Fall 2017

A Climactic Unimak Island Caldera-Forming Eruption, Aleutian Arc, Alaska: Magma storage and pre-eruption P-T-fO2-H2O conditions of the rhyodacite magma

Olivia E. (Olivia Eliška) Anderson
Western Washington University, anderson.oliviae@gmail.com

A Climactic Unimak Island Caldera-Forming Eruption, Aleutian Arc, Alaska: Magma storage and pre-eruption P-T-fO_2-H_2O conditions of the rhyodacite magma

By

Olivia Eliška Anderson

Accepted in Partial Completion
of the Requirements for the Degree
Master of Science

ADVISORY COMMITTEE

Chair, Dr. Pete Stelling

Dr. Susan DeBari

Dr. Sean Mulcahy

GRADUATE SCHOOL

Dr. Gautam Pillay, Dean

Master's Thesis

In presenting this thesis in partial fulfillment of the requirements for a master's degree at Western Washington University, I grant to Western Washington University the non-exclusive royalty-free right to archive, reproduce, distribute, and display the thesis in any and all forms, including electronic format, via any digital library mechanisms maintained by WWU.

I represent and warrant this is my original work, and does not infringe or violate any rights of others. I warrant that I have obtained written permissions from the owner of any third party copyrighted material included in these files.

I acknowledge that I retain ownership rights to the copyright of this work, including but not limited to the right to use all or part of this work in future works, such as articles or books.

Library users are granted permission for individual, research and non-commercial reproduction of this work for educational purposes only. Any further digital posting of this document requires specific permission from the author.

Any copying or publication of this thesis for commercial purposes, or for financial gain, is not allowed without my written permission

Olivia E. Anderson

1 December 2017

A Climactic Unimak Island Caldera-Forming Eruption, Aleutian Arc, Alaska: Magma storage and pre-eruption P-T-fO_2-H_2O conditions of the rhyodacite magma

A Thesis

Presented to

The Faculty of

Western Washington University

In partial Fulfillment

Of the Requirements for the Degree

Master of Science

By

Olivia Eliška Anderson

December 2017

Abstract

Understanding the mingling interactions between felsic and mafic end-member magmas is essential in understanding the physical processes occurring in bimodal eruptions. The Fisher caldera-forming eruption (CFE), which co-erupted rhyodacite (~69 wt.% SiO_2) and basaltic andesite (~53 wt.% SiO_2) ~9400 yBP, was studied to better understand the scenarios under which bimodal CFEs erupt.

This study presents new geochemical and isotopic data from glasses and minerals from Fisher and Shishaldin CFE deposits. Geochemical relationships between Shishaldin and Fisher CFEs indicates these deposits are from the same eruption, sourced from magmas underlying the Fisher Volcano. Results from differentiation models show that the rhyodacite did not form from closed-system fractional crystallization of the co-erupted basaltic andesite, similar to observations of antecrystic minerals and $\delta^{18}O$ data. Assimilation of hydrothermally-altered country rock is interpreted to cause the low $\delta^{18}O$ signature of both the basaltic andesite and rhyodacite.

In this study, I test three hypotheses for magma plumbing systems that have been shown to lead to compositionally bimodal CFEs: (1) a single, compositionally-zoned magma chamber, (2) a shallow silicic reservoir and a mid- or deep-crustal basaltic andesite reservoir, with rising mafic magma injecting into the shallow chamber; and (3) an independent and complex system of magma chambers within the upper crust. Geochemical modeling results and oxygen isotope data suggest that the Fisher magmatic system likely comprised a complex system of multiple independent, shallow magma chambers with the rhyodacite and basaltic andesite evolving separately but proximal to each other. The shallow rhyodacite had a pre-eruptive temperature of 877 – 908°C and the basaltic andesite had a pre-eruptive temperature of 1065 – 1147°C. Pre-eruptive water contents of ~4±1.5 wt.% H_2O for the rhyodacite and ~0 – 2.5 wt.% H_2O for the basaltic andesite suggest that the magmas were typical for Aleutian arc magmas.

Acknowledgements

My thesis could not have happened without funding from the Geological Society of America, Alaska Geological Society, Western Washington University (WWU) RSP grant, and the WWU Geology department. Funding from the above organizations was much appreciated.

I thank my advisor, Pete Stelling, for his guidance in this endeavor and for helping me progress my thesis. It was a wonderful experience, even with the ups and downs, to tackle the questions of complex magmatic systems.

I would like to extend many thanks to my thesis committee members, Sue DeBari and Sean Mulcahy. Sue, your editing powers helped me turn my thesis writing orders of magnitude better. Sue and Sean, I thank both of you for your time and devotion near the completion of this thesis to get it where it needed to be.

Thank you to all of the Western Washington University faculty and staff who supported this research, especially Ben Paulson who always had the time to help out with the logistics of lab work. Many thanks to Scientific Technical Services (SciTech), especially Charles Wandler, Erin Macri, and Dan Carnevale, for my use of the SEM, which was essential to my research.

Many thanks to Ilya Bindeman for his help in obtaining oxygen isotope data of my rocks and understanding how oxygen isotopes can be applied to volcanic systems. I would also like to thank Keith Putirka and Frank Spera who provided invaluable feedback on thermobarometry and MELTS modeling, respectively. I very much appreciate the thorough responses and the time they took in helping me.

My deepest thanks to my cohort and friends, including Paige Knapp, Kristina Gustovich, Luan Heywood, Rebecca Morris, and Stephanie Truitt. I could not have asked for a more supportive group. I would like to especially thank Rebecca Morris for her help near the completion of this thesis when life felt most difficult and for her thoughtful comments on my thesis.

Last, but not least, I would like to thank my parents for all of their support over the years. I very much wish my dad could be around now to see my thesis to its completion, but I am sure he knew that it would happen.

Table of Contents

Abstract iv

Acknowledgements v

List of Tables viii

List of Figures ix

1. Introduction 1

2. Background and Geologic Setting 6
- **2.1 Geologic Setting** 6
- **2.2 Fisher Caldera** 6
- **2.3 Unimak CFE deposits of uncertain origin** 9
- **2.4 Shishaldin** 10

3. Methods 11
- **3.1 Sample Selection and Petrography** 11
- **3.2 Mineral separation** 12
- **3.3 Stable oxygen isotope analyses** 12
- **3.4 Major and minor element analyses of minerals and glass** 13
  - 3.4.1 Geothermometry 13
  - 3.4.1a Two-oxide geothermometry 14
  - 3.4.1b Pyroxene thermobarometry 14
  - 3.4.1c Olivine-liquid thermometry 15
  - 3.4.1d Apatite saturation thermometry 15
  - 3.4.2 Plagioclase hygrometry 15
  - 3.4.3 Fractional crystallization modeling 16

4 Results 17
- **4.1 Petrography and Chemistry** 17
  - 4.1.1 Rhyodacite glass and phenocrysts 17
  - 4.1.2 Basaltic andesite glass and phenocrysts 26
  - 4.1.3 Summary of petrography and chemistry 34
  - 4.1.4 Evidence for magma mingling 35
- **4.2 Pre-eruptive Conditions: T-P-fO_2** 36
  - 4.2.1 Rhyodacite pre-eruptive conditions 36
  - 4.2.2 Basaltic andesite pre-eruptive conditions 43
- **4.3 Pre-eruptive water content** 45
- **4.4 Oxygen isotope chemistry** 48
- **4.5 Relationship between the rhyodacite and basaltic andesite** 54
- **4.6 MELTS modeling** 54
  - 4.6.1 Liquid line of descent from MELTS modeling 57
  - 4.6.2 Fractionating minerals 59
  - 4.6.3 Intensive conditions: temperature and H_2O content 61
  - 4.6.4 Summary of MELTS modeling 61

5 Discussion 63
- **5.1 Unimak CFE: Fisher CFE or Shishaldin CFE?** 63
- **5.2 Fisher CFE oxygen isotope geochemistry** 64
- **5.3 Fisher magmatic system** 66
  - 5.3.1 Hypothesis #1 66
  - 5.3.2 Hypothesis #2 66
  - 5.3.3 Hypothesis #3 67

5.4 Assimilation in the Fisher CFE 68
5.5 Fisher CFE Pre-Eruptive Conditions 69
5.6 The Mingling Timescales of the Fisher CFE 70
5.7 The Mechanics of the Fisher CFE 71
6 Conclusion 74
References 76
Appendices 80

List of Tables

Table 1. Representative rhyodacite glass chemistry……..……..…18

Table 2. Representative rhyodacite mineral chemistries……... 21-22

Table 3. Representative basaltic andesite glass chemistry……..… 27

Table 4. Representative basaltic andesite mineral chemistries……...……... 30

Table 5. Summary of minerals present in magmas…….……..… 34

Table 6. Two-oxide thermometry and oxygen barometry results…….…… 37

Table 7. Orthopyroxene-liquid thermobarometry results……...…….... 42

Table 8. Two-pyroxene thermobarometry results……...……. 43

Table 9. Clinopyroxene-liquid thermobarometry results……...…… 45

Table 10. Olivine-liquid thermometry results……...… 45

Table 11. Oxygen isotope compositions…….…. 50

Table 12. Simple subtraction crystal fractionation model results…….…. 55

Table 13. MELTS results……...…….…. 55

List of Figures

Figure 1. Magma model hypotheses for the Fisher system …… 2
Figure 2. Map of Unimak Island……... …… 3
Figure 3. Field expression of deposits……..……. 7
Figure 4. Schematic stratigraphic section…….…. 8
Figure 5. Glass chemistry……. 19
Figure 6. F-type rhyodacite minerals……..... 20
Figure 7. Cathodoluminescence textures of plagioclase in rhyodacite…….…...… 23
Figure 8. S-type rhyodacite minerals……..…….…...… 23
Figure 9. F-type basaltic andesite minerals and textures…….…….…...… 31
Figure 10. S-type basaltic andesite minerals and textures……... 32
Figure 11. Mineral chemistry……...……. 33
Figure 12. S-type banded pumice mingling textures……..…... 35
Figure 13. Two-oxide thermometry…….. 38
Figure 14. Thermometry results and comparison……...… 39
Figure 15. Barometry results and comparison……... 41
Figure 16. Plag-Liq Hygrometer results……. 47
Figure 17. Oxygen isotope equilibrium plots……. 51-52
Figure 18. Oxygen isotope results……. 53
Figure 19. Simple subtraction fractional crystallization model results…… 56
Figure 20. MELTS liquid model results…… 57
Figure 21. MELTS Temperature vs. P_2O_5…… 58
Figure 22. MELTS plagioclase and pyroxene results…… 60
Figure 23. MELTS Temperature vs. SiO_2……. 62
Figure 24. MELTS P-T-H_2O model results…….. 62
Figure 25. Fisher CFE Petrogenetic Model…….…. 68
Figure 26. Fisher CFE eruption & mingling scenario…….…….....…….…….. 73

1. Introduction

Caldera-forming eruptions (CFEs) often erupt multiple, compositionally-distinct magmas, including mafic and silicic endmembers, that mingle prior to eruption (e.g., Pallister et al., 1992; Pallister et al., 1996; Hildreth and Fierstein, 2012; Larsen, 2006). Eruptions that have been determined to have been triggered by magma mixing and mingling are common in the literature [e.g., Fisher (Stelling et al., 2005); Katmai (Hildreth and Fierstein, 2000); Ksudach in Kamchatka (Braitseva et al., 1996); Pinatubo (Pallister et al., 1992)]. Case studies of bimodal eruptions show that when a mafic magma is injected into a silicic magma chamber, that event can trigger an eruption due to increased temperature as a result of contact between the mafic and silicic magmas (e.g., Sparks and Sigurdsson, 1977). In this case, the resident silicic magma is thought to become overheated, undergo vigorous convection, and experience an increase in its volatile content donated from the mafic component. When two magmas of drastically different temperatures mingle, the transfer of heat occurs at a faster rate (~3-5 orders of magnitude) than the transfer of mass (i.e., chemical diffusion; Sparks and Marshall, 1986), causing mingling rather than mixing of magmas as evidenced by banded pumice. Another mechanism for the formation of banded pumice is a single stratified magma chamber (Hildreth and Fierstein, 2012). In this case the banded pumice forms at the interface between the silicic and mafic components. In a single, compositionally zoned magma chamber, the silicic liquid is the product of fractional crystallization of a resident mafic magma. The low density of the silicic liquid causes it to rise and accumulate at the top of the magma chamber. An injection into the base of the magma chamber could cause a temperature increase and/or pressure change in the chamber, inciting an eruption of both mafic and felsic magmas. Determining the pre-eruptive conditions, such as temperature and pressure, can provide evidence of where the magmas reside from pressure estimates and how they interacted with each other (e.g., thermal zonation).

Hildreth (1987) suggests that any time eruptive deposits show mingling of various compositions, each of the following processes should initially be considered, and these are the hypotheses that will be tested in this study at a single volcanic center (Fig. 1): (1) a single zoned or layered chamber, (2) addition of a new batch of relatively primitive magma from depth, and (3) mingling of magmas from two or more discrete shallow chambers of a complex reservoir. An ideal location to test these models is where a single volcanic

system has had a compositionally bimodal CFE and more than one interpretation of its magmatic plumbing model by different authors. Fisher Volcano, on Unimak Island, Alaska (Fig. 2), has had two magmatic plumbing models proposed for its magma system prior to the Fisher CFE: (1) a single, compositionally-zoned magma chamber (Miller and Smith, 1977; Bindeman et al., 2001) and (2) independent and complex system of magma chambers within the upper crust (Stelling, 2003; Stelling et al., 2005). Bindeman et al. (2001) also considered Hildreth's second model of a relatively primitive magma from the deep crust, but this model did not fit with the Fisher CFE. The current study seeks to test all of these hypotheses and determine the pre-eruptive volcanic plumbing system on Unimak Island.

Oxygen isotope data can help constrain the components and history of magmatic interactions with its environment and further constrain the architecture of the plumbing system beneath the volcano. An uncommon characteristic of the Fisher CFE is the low $\delta^{18}O$ content of its erupted products, which suggests some degree of assimilation occurred prior to the cataclysmic event (Bindeman et al., 2001). This isotope signature plays an important role in constraining the magmatic plumbing system of Fisher Volcano in that it can provide pre-eruptive temperature estimates and information about the petrologic relationships between

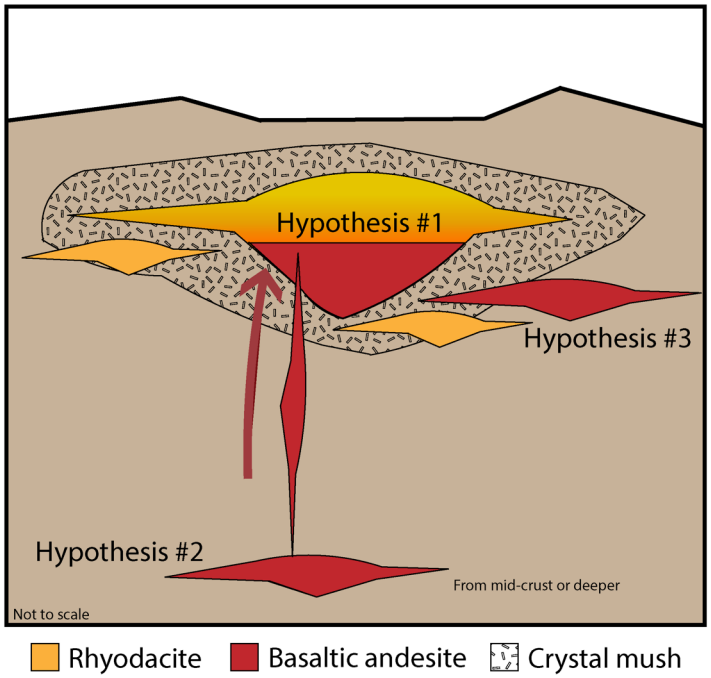

Figure 1. Possible models of the magmatic system beneath Fisher caldera, based on ideas from Hildreth (1987): a single zoned or layered chamber (Hypothesis #1), addition of a new batch of mafic or primitive magma from depth into an existing shallow crustal reservoir (Hypothesis #2), and mixing of magmas from two or more discrete chambers of a reservoir complex (Hypothesis #3).

the two magmas (Bindeman, 2008). Processes that affect $\delta^{18}O$ content in magmas include interaction with meteoric water and assimilation of rocks with significantly different $\delta^{18}O$ (Bindeman, 2008). The origin of mixed magmas, whether in a single magma chamber or in separate reservoirs, can be determined by stable oxygen isotope signatures in crystals. Stable oxygen isotope analysis can illuminate different crystal sources, assimilant sources, and the involvement of water with magmas (Bindeman, 2008). Each different source of contamination has a unique $\delta^{18}O$ signature, and different magmatic phases incorporate oxygen isotopes at different rates at different temperatures. In this study, I have collected oxygen isotope chemistry of plagioclase, orthopyroxene, clinopyroxene, and Fe-Ti oxides from the rhyodacite and plagioclase and orthopyroxene from the basaltic andesite. An independent pre-eruptive temperature estimate may be gained from equilibrium pairs of these minerals. Whether or not the crystals are in equilibrium, assimilation and constraints on the magmatic plumbing system can be determined from oxygen isotope values of minerals.

The deposits from at least one large bimodal explosive eruption from Fisher Volcano, an 11x18 km caldera in the center of Unimak Island, and possibly another CFE from Shishaldin, have been documented

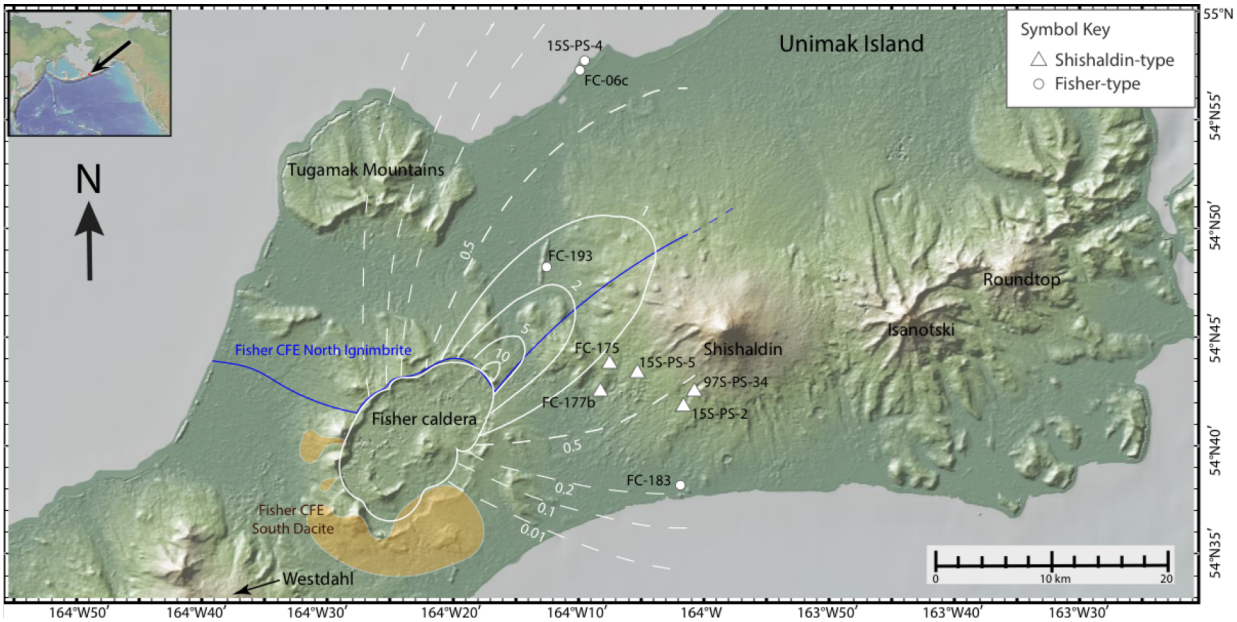

Figure 2. Map of Unimak Island showing the sample locations of this study. Isopachs taken from Stelling et al. (2005) and represent the thicknesses in meters of the Fisher CFE North Dacite across Unimak Island based on field observations. The extent of the Fisher CFE North Ignimbrite is represented by the blue line and the Fisher CFE South Dacite is represented by orange areas. Basemap from GeoMapApp, using Global Multi-Resolution Topography (GMRT) Synthesis of Ryan et al. (2009).

across the central portion of the island and extending as far east as Cold Bay, AK, 140 km away on the Alaskan Peninsula (Funk, 1974; Miller and Smith, 1977, Bindeman et al., 2001; Carson et al., 2002; Stelling, 2003; Stelling et al, 2005; Gardner et al., 2007). This multi-compositional CFE has two primary compositional endmembers: rhyodacite pumice and basaltic andesite scoria. This study has integrated evidence from all of the prior studies along with new data to provide a better understanding of the pre-Fisher CFE magmatic system and the complexity of bimodal CFEs overall.

To distinguish between the hypotheses (#1-3 in Fig. 1) for the pre-eruptive architecture of Fisher Volcano, I have constrained the magmatic plumbing system of the Fisher CFE in a way that would explain simultaneous eruption of a basaltic andesite and rhyodacite. Understanding pre-eruptive conditions (pressure, temperature, oxygen fugacity, and water content) of both magmas helped resolve the magma plumbing system of the CFE and provided some constraints on how the magmas interacted when they mingled. Other estimates of mingling timescales involved the resorption textures of plagioclase and Fe-Ti oxides and their associated time to develop those textures. I used petrography to characterize textures and crystal compositions of each magma type and oxygen isotopes to determine whether the basaltic andesite and rhyodacite have the same distinct oxygen isotope chemistry. I also utilized major element chemistry of minerals and glass to (1) apply mineral-liquid thermobarometry and hygrometry to estimate pre-eruptive conditions and (2) to model whether the basaltic andesite and rhyodacite are related by fractional crystallization. The thermobarometry and hygrometry are also vital to the thermodynamic modeling of fractional crystallization. A strong fractional crystallization relationship between the co-erupted magmas would suggest the presence of a single large stratified magma chamber as suggested in hypothesis 1 (Miller and Smith, 1977; and Bindeman et al., 2001), (Fig. 1). Barometry is also useful in determining the magmatic plumbing system because hypotheses 1 and 3 would suggest both magmas are at low pre-eruptive pressures whereas in hypothesis 2 the mafic magma would have a higher pre-eruptive pressure than the rhyodacite.

Oxygen isotope values are also useful with determining the type of magmatic plumbing system that lies under Fisher Volcano prior to its CFE. Low oxygen isotope values for both the rhyodacite and the basaltic andesite would support magmatic plumbing models of shallow crystallization, either as a large

stratified reservoir as suggested by Bindeman et al. (2001) or multiple, independent, shallow reservoirs as suggested by Stelling (2003), Stelling et al., (2005) and Gardner et al., (2007), which are Hildreth's hypotheses 1 and 3, respectively. If both the rhyodacite and basaltic andesite have low $\delta^{18}O$ values, then both had to have been residing within the upper crust in order to assimilate low $\delta^{18}O$ rocks. If the $\delta^{18}O$ values are different, then the basaltic andesite may have been from the mid- to deep crust and then possibly triggered the eruption.

It is possible that multiple bimodal CFE deposits are present on Unimak, and not all of them are clearly related to Fisher Volcano. A subset of deposits on the lower west flanks of Shishaldin Volcano appear to thicken toward Shishaldin (Stelling, 2003) and have different depositional characteristics although the individual components of the deposits have similar whole rock chemistry. The known Fisher CFE deposits are called F-type and the deposits of unknown origin are called S-type in this study. This project is the first to focus on the S-type deposits, first described in Stelling (2003), and presents new geochemical data on matrix glasses and minerals from S-type and F-type deposits. These new data are compared to the known chemistry of the Fisher CFE versus Shishaldin lavas (Bindeman et al., 2001) to determine their sources. Fortunately, Bindeman et al., (2001) determined that the Fisher CFE deposits have a characteristically low $\delta^{18}O$ signature as compared to Shishaldin lavas, which have a normal $\delta^{18}O$ signature (~5.5‰), and these data provide important evidence to determine whether there are one or more CFE deposits exposed in central Unimak Island.

The conditions of magma storage determined from the current study would serve as a test of Stelling's model for Shishaldin of a magma system of shallow and lower crustal reservoirs where assimilation occurs if the S-type deposits were erupted from Shishaldin. If the fractional crystallization MELTS modeling does not work and oxygen isotope chemistry is different between the rhyodacite and basaltic andesite, then Stelling's model is correct. If fractional crystallization does work from the basaltic andesite to the co-erupted rhyodacite and oxygen isotope chemistry is the same between the two magmas, then Stelling's model must be incorrect. The above conclusions would still be valid for the Fisher system if the S-type deposits were erupted from Fisher Volcano.

There are several conclusions in this study. The results of this study indicate that the S-type deposits are from the Fisher CFE and not from Shishaldin as mineralogy, chemistry, and stable isotopes are identical within error and are distinct from Shishaldin chemistry. The rhyodacite and co-erupted basaltic andesite cannot be related to each other by fractional crystallization but are from independent magma reservoirs from Fisher Volcano. The low oxygen isotope signature of both the rhyodacite and the basaltic andesite further suggest that these magmas existed in separate, shallow crustal reservoirs prior to eruption. Thus, the Fisher CFE is another instance of multiple small magma chambers interacting at a system initially interpreted as a single stratified chamber. It seems that a large, stratified reservoir as a feeder for CFEs is a much less likely interpretation than previously thought (Dreher et al., 2005).

2. Background and Geologic Setting

2.1 Geologic Setting

Unimak Island lies very near the transition from continental crust to oceanic crust and may be on continental crust. The crust east of Unimak Pass (just east of Unimak Island) is continental whereas the crust west of Unimak Pass is oceanic (Shillington et al., 2004). The volcanoes on Unimak Island are a part of the Aleutian Arc, which is formed by the subduction of the Pacific Plate under the North American Plate. Unimak Island is located in the center of the 1,800-km-long volcanic arc (Fig. 2). The top of the subducting slab is ~92 km beneath Shishaldin, ~94 km beneath Fisher, and 85 km beneath Westdahl (Syracuse and Abers, 2006).

2.2 Fisher Caldera

The pre-Fisher CFE magmatic system has been interpreted as either having been comprised of multiple magma chambers (Stelling et al., 2005) or a single stratified reservoir (Miller and Smith, 1977; Bindeman et al., 2001). Fisher Caldera (1112 m elevation) is one of the largest calderas in the Aleutian Arc (Miller and Smith, 1977; Miller et al., 1998). Silicic eruptions at Fisher have increased in frequency since the late Pleistocene, changing from an average of ~26 ky between silicic eruptions to 4.5 ky. The Fisher system prior to the CFE of ~9400 yBP was composed of at least 8 stratocones (Stelling et al., 2005). Miller and Smith (1977) noted the voluminous ash flow deposits of the Fisher CFE. Stelling et al. (2005) and Gardner et al. (2007) further mapped the Fisher CFE deposits, filling in areas not previously mapped. They found the Fisher CFE erupted

three compositionally distinct magmas: a low-Si dacite in low volume (<1 km^3) ash fall and flow deposit to the south (Fisher CFE South Dacite; not analyzed in this study), a high-Si rhyodacite in ash fall to the north (Fisher CFE North Dacite) capped by a mixed basaltic andesite-dacite in a voluminous ignimbrite (Fisher CFE North Ignimbrite) to the north (Fig. 2). Stelling (2003) and Stelling et al. (2005) estimated the eruptive volume of the Fisher CFE to be between 20 and 100 km^3, the minimum value based on mapped deposits and the maximum using the caldera dimensions and a vertical drop based on the internal relief of one of the cones.

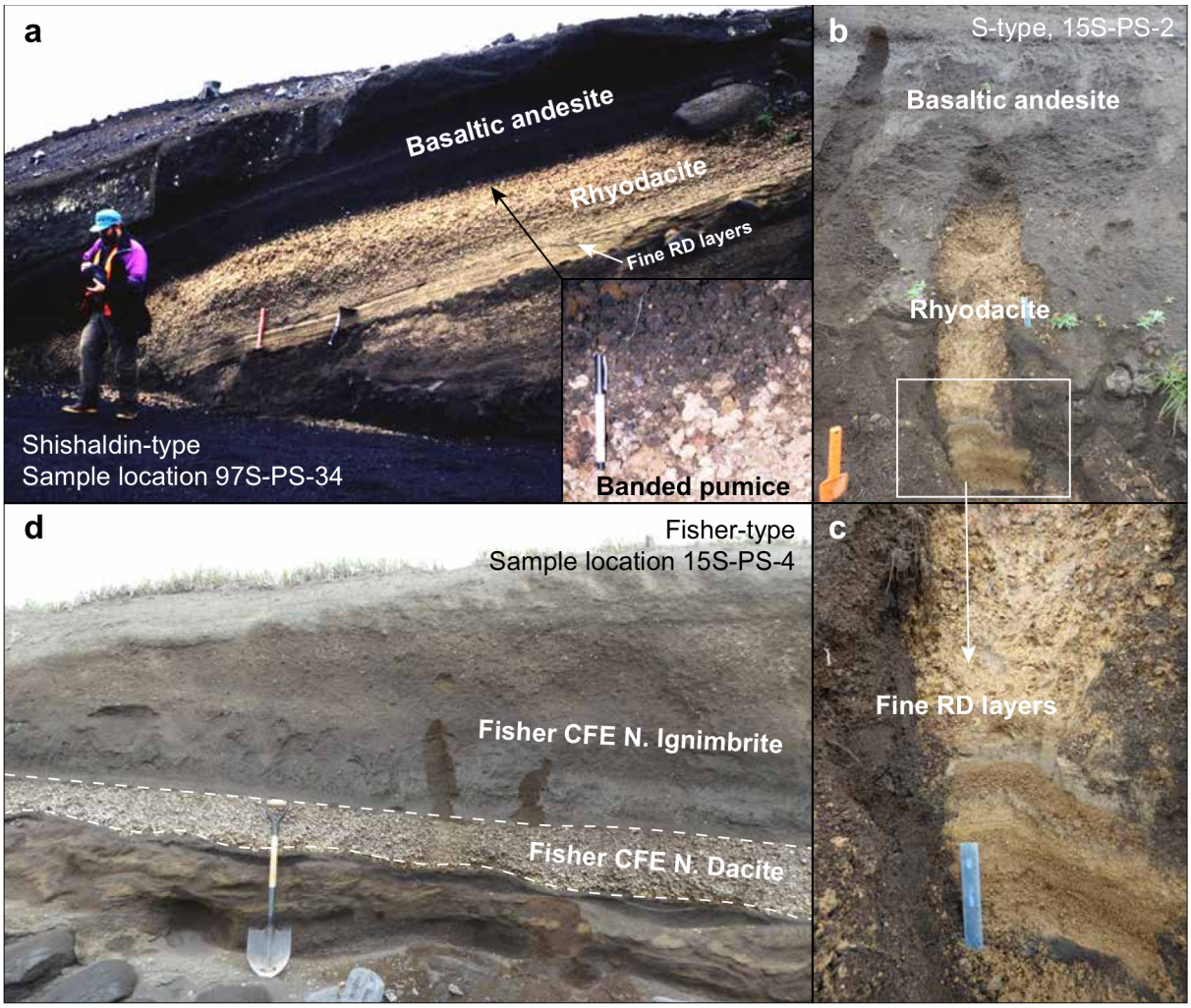

Figure 3. (a) The first S-type outcrop documented. Inset shows the banded pumice zone that borders between the rhyodacite pumice layer and the basaltic andesite scoria layer. **(b)** Another S-type outcrop where samples were collected in August 2015 showing the same pattern of pumiceous rhyodacite overlain by scoriaceous basaltic andesite. Part **(c)** is a close up of the fine rhyodacite (RD) layers that underlie the coarser-grained rhyodacite. **(d)** Outcrop of the F-type deposit, which only contains the pumiceous rhyodacite overlain by a thick pyroclastic flow deposit containing both basaltic andesite and rhyodacite compositions. The F-type lacks the fine, rhyodacite layers with lapilli-sized ash fall deposits and a discrete scoria layer. Photos courtesy of Pete Stelling.

North and northeast of Fisher volcano, the Fisher CFE North Dacite deposit (in this study called Fisher-type; Fig. 3, 4) occurs as a rhyodacite pumice fall on top of soil, capped by poorly to moderately welded ignimbrite containing clasts of basaltic andesite scoria, rhyodacite pumice, and banded pumice that preserve evidence of mingling of these two magmas. The rhyodacite pumice in the ignimbrite is compositionally identical to the underlying pumice fall deposit. The pumice fall deposit preserves a color

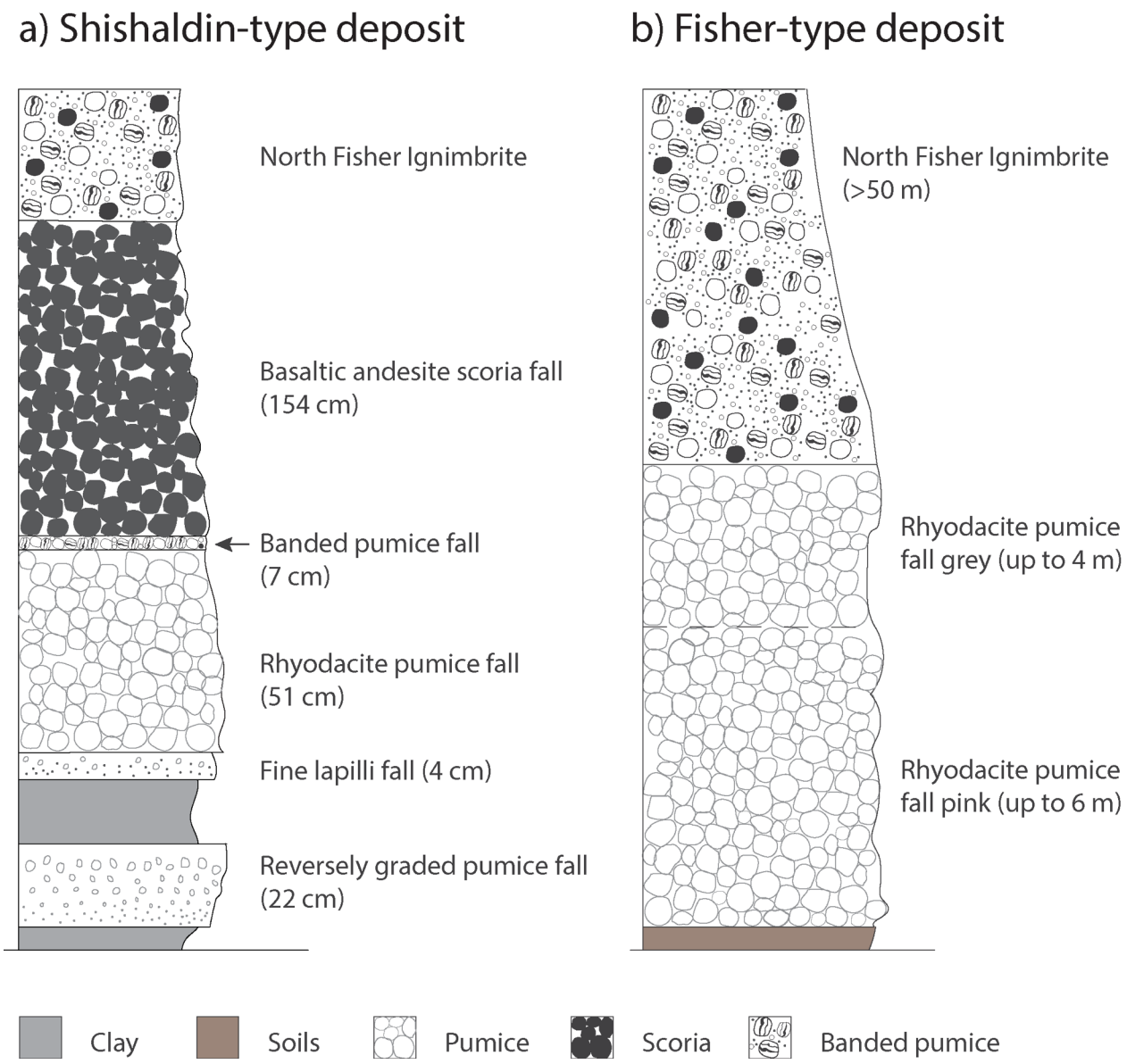

Figure 4. Schematic stratigraphic section of the **(a)** Shishaldin-type and **(b)** Fisher-type CFE deposits. Sections are not to scale, but approximate thicknesses are given. The S-type section is based on sample location 15S-PS-2 measured by Pete Stelling in 2015 whereas the F-type section is based on estimates of Stelling (2003).

change from yellow/pink to grey in the upper 25% of the deposit that is a result of differential oxidation with no compositional difference (Stelling, 2003; Stelling et al., 2005).

Bindeman et al. (2001) showed that the Fisher CFE deposits can be distinguished by anomalously low $\delta^{18}O$ with $\delta^{18}O$ plagioclase of +4.79 ± 0.24‰. A proxy for the $\delta^{18}O$ of dacite to basaltic andesite magmas are the $\delta^{18}O$ of andesine and labradorite plagioclases from its host magma. Normal $\delta^{18}O$ magmatic values are >+5.5‰ and anything <+5.5‰ is considered low $\delta^{18}O$ for magmas (Bindeman, 2008). Light meteoric waters from glaciers have oxygen isotope values <-25‰ and hydrothermal systems with $\delta^{18}O$-depletion can have oxygen isotope values as low as -5‰. Meteoric water in the Aleutian Islands is -10 ± 2‰ (Perfit and Lawrence, 1979). At the last glacial maximum (LGM; ~23,000 yBP for southwestern Alaska), the Alaskan Peninsula and Unimak Island were covered by a 300 – 500 m-thick ice cap (Mann and Peteet, 1994). Bindeman et al. (2001) suggest Fisher CFE magmas' low isotopic signature was caused by assimilation of ~5–10% hydrothermally-altered rocks that had interacted with glacial meltwater.

2.3 Unimak CFE deposits of uncertain origin

Not all CFE deposits on Unimak are clearly related to Fisher Volcano, however. A subset of deposits on the lower west flanks of Shishaldin Volcano appear to thicken toward Shishaldin (Stelling, 2003). Shishaldin's current stratocone is built on top of an ancient caldera (somma), which is 4 km in diameter. If those deposits were from Shishaldin, it must have been a very large eruption to generate the thick deposits observed along its flanks of ~0.5 m of pumice overlain by ~1.5 m of scoria. This supposed eruption could have been large enough to cause a caldera collapse, which is represented by the somma. These Shishaldin-type (S-type) CFE deposits have a basal sequence of up to nine finely laminated interlayered lapilli-rich pumice and clay-rich layers, overlain by coarse yellow-pink pumice, a thin banded pumice layer, and a thick black scoria layer. This sequence of fall deposits is sometimes capped by poorly- to moderately-welded ignimbrite containing pumice and scoria. Within this study, S-type deposits represent the deposits with basal lapilli layers and a discrete scoria layer on top while Fisher-type (F-type) deposits represent deposits that do not have a separate scoria layer with the rhyodacite pumice (Fig. 3, 4). The rhyodacite in both F-type and S-type deposits are ~69 wt.% SiO_2 whereas the basaltic andesite for both sets is ~53 wt.% SiO_2. Bindeman et al. (2001) suggest that the

anomalously low $\delta^{18}O$ signature of the Fisher CFE was a good identifier of the Fisher CFE. Thus, oxygen isotope values can be used to determine if the F-type and S-type deposits represent two separate eruptions because Shishaldin lavas have a normal $\delta^{18}O$ signature of 5.6 to 6.2‰ (Bindeman et al., 2001).

2.4 Shishaldin

Shishaldin (2857 m) has been active since the mid-Pleistocene (Stelling, 2003), and is the second-most active volcano in the Aleutians. The most recent explosive eruption of Shishaldin was a sub-Plinian basaltic eruption in 1999 (Stelling et al., 2002). Other similar Holocene deposits are found on the flanks of Shishaldin, suggesting this type of explosive basaltic eruption is not unusual for this volcano (Stelling et al., 2002). The current stratovolcano of Shishaldin is constructed on top of ancestral Shishaldin, or somma, which may be the remnants of an older caldera that erupted the S-type deposits (Fournelle, 1988; Stelling, 2003). Remnants of the somma are exposed on the west and northeast sides at 1500 – 1800 m elevation but Shishaldin is covered by snow and ice in the upper 1000 m of Shishaldin. The somma was partially destroyed ~10 ka with sector collapse, causing a large debris avalanche (Beget et al., 1998). Since the somma collapse, the edifice has been filled by continued volcanism, which formed the upper ~1000 m of Shishaldin.

The magmatic plumbing system at Shishaldin remains enigmatic, but several studies have suggested complexity. Early petrologic studies of Shishaldin volcanics by Fournelle (1988) identified three main basalt types: high-Al, high-Mg, and FeTi. Fournelle (1988) and Fournelle and Marsh (1991) suggested that the high-Al basalt is the parental magma for the Shishaldin system, and that fractionation of plagioclase from this parental magma produced the FeTi basalts, andesites, dacites, and rhyodacites observed at Shishaldin. High-Mg are suggested to be hybrids of low-Mg arc magma that assimilated country rock from the Jurassic Border Ranges ultramafic complex.

Beget et al. (2002) and Stelling (2003) further mapped the eruptive deposits of Shishaldin and Fisher caldera. Stelling suggested that Shishaldin magmas were derived from variable combinations of inputs from the mantle wedge, slab, subducted sediments and crustal assimilation. Stelling proposed a two-staged magmatic system where crustal assimilation occurs near the base of the crust and at shallow crustal levels. Stelling found that the S-type rhyodacite may be of the shallow assimilation type, whereas the S-type basaltic

andesite belongs to the deeper assimilation-magma series. The approach that Stelling took used geochemical trends to investigate these large-scale processes for the entire Shishaldin magmatic suite. In contrast, this study focuses on a single eruption in which comingling occurs between a basaltic andesite and a rhyodacite.

Other researchers have since proposed a two-stage magmatic complex at Shishaldin that agrees with the Stelling model. Based on long-period (LP) seismic events, Cusano et al. (2015) suggested a mostly degassed magma within a shallow magma plumbing system and a deeper, less-degassed magma reservoir. The activation path between these two magma systems is what caused variations in the LP events. Additionally, in a study of the seismicity and deformation associated with the 1999 basaltic sub-Plinian eruption of Shishaldin, Moran et al. (2006) hypothesized that new magma ascended from >10 km depth rapidly (at least 80 m/day) to a shallow magma reservoir. This study will add to this model by resolving whether Shishaldin had a CFE in its volcanic history. If the S-type deposits have a different chemistry than the F-type deposits, then it tells us that the Shishaldin plumbing system is capable of a bimodal CFE, and it will allow for the investigation of two magmatic systems. If the S-type and F-type chemistries are identical it suggests a single eruption, likely from Fisher, with a complex depositional pattern.

3. Methods

3.1 Sample Selection and Petrography

Samples of both F- and S-type deposits were collected in 1997, 2000 and 2015 by Dr. Pete Stelling (Fig. 2). The S-type deposits were collected from locations that expose a thick pumice layer overlain by a dark scoria layer, the distinctive field characteristic of S-type deposits (sample locations 97S-PS-34, 15S-PS-2, 15S-PS-5, FC-175, FC-177B; Fig. 2). The F-type deposits were collected from locations that lacked a discrete scoria layer, (sample locations FC-06c, FC-183, FC-193, and 15S-PS-4). Textures and approximate chemistry of minerals and glass were determined using a petrographic microscope and a Tescan Vega scanning electron microscope (SEM) equipped with a backscattered electron (BSE) detector, cathodoluminescence (CL) detector, and an energy dispersive spectrometer (EDS). CL was intended to be a way to distinguish between the F-type and S-type plagioclases, but the CL zones were too complex to decipher any diagnostic characteristics.

3.2 Mineral separation

Pumice and scoria samples were crushed from seven samples using a corundum mortar and pestle to pick crystals for oxygen isotope analyses. These oxygen isotope analyses were intended to be used for pre-eruptive temperature estimates and were used to determine the magmatic plumbing model. Plagioclase, pyroxene, and Fe-Ti oxide crystals were picked from the crushed samples. Initial crystal separation was made by density using water to separate out larger pieces of pumice to simplify picking after crushing. Up to 2 mg of crystals were collected for each oxygen isotope analysis. In some cases, this mass was achieved with a single crystal, and in others multiple crystals were grouped based on similarity of size, shape and color. Silicate mineral samples ranged from ~4-70 crystals, and Fe-Ti oxides required >20 crystals to meet the target mass for analysis. Pyroxenes with Fe-Ti oxide inclusions or rim growth, although common, were avoided. Plagioclase crystals were generally larger than pyroxenes or Fe-Ti oxides in the rhyodacite, so these crystals could more readily be analyzed as single crystal.

3.3 Stable oxygen isotope analyses

Bindeman et al., (2001) suggested that anomalously low $\delta^{18}O$ signatures could be used as a defining characteristic of the Fisher deposits as compared to most eruptions, which have normal $\delta^{18}O$ signatures. To determine if there are differences between the F-type and S-type samples and constrain assimilation processes, oxygen isotope analyses were conducted on single crystal and bulk crystal separates of plagioclase, orthopyroxene, clinopyroxene, and Fe-Ti oxides from both F-type and S-type samples. Oxygen isotope analyses were conducted at the CO_2-laser fluorination/mass-spectrometer lab at the Stable Isotope Lab at the University of Oregon. Plagioclase separates were pretreated with BrF_5 whereas pyroxenes and Fe-Ti oxides were pretreated overnight to remove alteration or adhered glass. The samples were heated with a 25 W CO_2 laser in the presence of BrF_5 gas to free the oxygen. Oxygen was converted to CO_2 gas and the CO_2 gas was analyzed on an MAT 253 10kV gas source isotope ratio mass spectrometer (IRMS). A Gore Mountain garnet ($\delta^{18}O$ = 6.52‰) was used as a working standard. Typical 1σ analytical error is 0.08 – 0.12‰, and a 2σ level of certainty of ±0.2‰ is used to distinguish analytical error versus natural variations.

3.4 Major and minor element analyses of minerals and glass

Twenty-two polished thin sections of samples from different field locations were analyzed using electron probe microanalysis (EPMA) for this study in order to determine the major and minor element chemistry of minerals and glass. For the type locality of the Shishaldin-type samples, two thin sections of each deposit were made. Glass and mineral major element chemistry was analyzed by a Cameca SX-100 electron probe microanalyzer (EPMA) at the University of California, Santa Barbara (UCSB). Mineral analyses at UCSB were analyzed using a 15 kV accelerating voltage, 10 nA beam current, and 1 μm beam diameter. Minerals analyzed were plagioclase, clinopyroxene, orthopyroxene, ulvöspinel, ilmenite, and olivine. The glass chemistry at UCSB was analyzed with a 15 kV accelerating voltage, 5 nA beam current, and 5 μm beam diameter. Time dependent intensity (TDI) corrections were made for Na, K, Si, Ti, and Fe. Sodium decay required the most correction and had TDI corrections between -9 and 223%. Pumice and scoria samples were sent to the Alaska Volcano Observatory (AVO), and AVO obtained glass chemistry prior to this study with a JEOL 8900 EPMA at the USGS Menlo Park, CA, using the same analytical conditions as at UCSB. Data collected at UCSB overlap with those collected at Menlo Park within error in that the data points cluster over each other as in Fig. 5 (Appendix A1-A5). The average and standard deviation of the 2σ errors of individual EPMA glass analyses at UCSB are: 0.54±0.02 wt.% SiO_2, 0.25±0.005 wt.% Al_2O_3, 0.13±0.026 wt.% TiO_2, 0.23±0.04 wt.% FeO (total), 0.04±0.002 wt.% MnO, 0.028±0.009 wt.% MgO, 0.078±0.02 wt.% CaO, 0.12±0.02 wt.% Na_2O, 0.086±0.008 wt.% K_2O, 0.031±0.003 wt.% Cl, and 0.053±0.004 wt.% P_2O_5. Error from AVO is likely similar to the errors from UCSB, but AVO did not report errors for their glass analyses.

3.4.1 Geothermometry

Geothermometers and geobarometers were used to estimate the pre-eruptive temperature and pressure of the rhyodacite and the basaltic andesite. These geothermobarometers are primarily based on equilibrium between mineral and melt or two minerals or in one case on a single mineral. The geothermobarometers and geothermometers used in this study are olivine-liquid, clinopyroxene-liquid, clinopyroxene, orthopyroxene-liquid, two-pyroxene, two-oxide, and apatite saturation. Apatite saturation thermometry and clinopyroxene thermobarometry rely only on one analysis (glass chemistry and clinopyroxene chemistry, respectively). Some

of these calibrations have larger errors than others, such as two-pyroxene thermobarometry. Two-oxide geothermometry is the most precise estimate available for pre-eruptive temperature for most silicic volcanic systems. Errors of calibrations that are from Putirka (2008) are given in the following sections (3.4.1b – c) using standard error of estimate (SEE), which is equivalent to 1σ uncertainty.

3.4.1a Two-oxide geothermometry

Two-oxide geothermometry relies on equilibrium between ilmenite and ulvöspinel and gives one of the most reliable temperature estimates for volcanic systems (Blundy and Cashman, 2008) as well as providing estimates of magmatic oxygen fugacity. Temperature and oxygen fugacity estimates were made following the approach of Andersen and Lindsley (1985) using Stormer's (1983) calculation of ulvöspinel and ilmenite components and calculated the ILMAT Excel spreadsheet (Lepage, 2003). The method of Ghiorso and Evans (2008) was also used as a comparison. The average absolute deviation (aad), which is the average of each sample's absolute deviation (how much a sample deviates from the average), of the Andersen and Lindsley (1985) thermometer is ±33°C and of the Ghiorso and Evans (2008) thermometer is ±44°C (Blundy and Cashman, 2008). For both methods, the aad for fO_2 estimations is 0.25 – 0.34 log units (Blundy and Cashman, 2008).

3.4.1b Pyroxene thermobarometry

The pyroxene geothermometers used in this study are orthopyroxene-liquid, clinopyroxene-liquid, and two-pyroxene (Eqns. 28a, 33, 36, respectively, in Putirka, 2008). The SEE for the orthopyroxene-liquid, clinopyroxene-liquid, and two-pyroxene thermometers are ±39°C, ±45°C, and ±56°C, respectively (Putirka, 2008). Equilibrium for orthopyroxene was determined using Fe-Mg exchange. For clinopyroxene, equilibrium was determined by comparing the observed clinopyroxene components (e.g., DiHd, EnFs, etc.) to calculated clinopyroxene components based on the glass chemistry as suggested by Putirka (2008; personal comm.). This method of testing for clinopyroxene equilibrium is more rigorous than relying on the Fe-Mg exchange alone.

The pyroxene geobarometers used in this study are orthopyroxene-liquid, clinopyroxene-liquid, two based on clinopyroxene chemistry, and two-pyroxene (Eqns. 29a, 30, 32a, 32b, 39, respectively, in Putirka, 2008). A new clinopyroxene-liquid calibration is also considered from Neave and Putirka (2017). The standard error of estimate (SEE), which is equivalent to 1σ uncertainty, for these barometers are ±2.6 kbar, ±3.6 kbar, ±3.1 kbar, ±2.6 kbar, and ±3.2 kbar, respectively. The Neave and Putirka (2017) calibration has an SEE of ±1.5 kbar.

3.4.1c Olivine-liquid thermometry

Olivine-liquid thermobarometry relies on equilibrium between olivine crystals and its associated glass or whole rock chemistry. The olivine and glass or whole rock pair are considered to be in equilibrium when K_D (Fe-Mg) = 0.30 ± 0.03 for basaltic systems (Roeder and Emslie, 1970). The thermobarometer of Beattie (1993) is preferred for anhydrous samples, and Putirka (2008; Eqn. 22) model has greater precision for hydrous glasses. The temperature estimate has an SEE of ±29°C for Eqn. 22 (Putirka, 2008) and ±44°C for Beattie (1993).

3.4.1d Apatite saturation thermometry

Apatite crystallization depends on SiO_2 and P_2O_5 contents of the glass and the temperature of the magma (Harrison and Watson, 1984). Because P_2O_5 varies little in apatite, the chemistry of the host glass can be used to determine the temperature at which apatite was saturated in the host magma, presuming that apatite was a crystallizing phase. Apatite saturation was calculated for the rhyodacite glass using the method of Harrison and Watson (1984) for metaluminous glass analyses and Bea et al. (1992) for peraluminous analyses. Apatite crystallization continues to 60°C – 100°C cooler than the saturation temperature as the magma cools. Therefore, the apatite saturation temperature represents a maximum estimate for the pre-eruptive temperature of the magma.

3.4.2 Plagioclase hygrometry

In order to determine the pre-eruptive water content of the magmas, a plagioclase hygrometer was applied using plagioclase and glass major element chemistry. The plagioclase-liquid hygrometer is based on the

exchange reaction of anorthite and albite components between plagioclase and its equilibrium liquid. Plagioclase chemistry is sensitive to temperature, dissolved water concentrations, and, to a lesser extent, pressure. The hygrometer calculation by Waters and Lange (2015) has been calibrated for liquid compositions ranging from basalts through rhyolites (45 – 80 wt.% SiO_2) and plagioclase compositions between An_{17-95}. The calculation has a standard error estimate of 0.35 wt.% H_2O. In most cases, glass analyses adjacent to plagioclase analyses were used. In cases where adjacent analyses were not possible, a representative glass composition of the sample was used. For the rhyodacite, two-oxide thermometry temperature estimates are used as an input whereas for the basaltic andesite temperature estimates and H_2O estimates for a range of temperatures are plotted together to constrain the water content of the basaltic andesite magma.

3.4.3 Fractional crystallization modeling

Fractional crystallization can be modeled to determine if the rhyodacite could be the fractional crystallization product of the co-erupted basaltic andesite. One of the primary ways this is accomplished in this study is by using MELTS, a thermodynamic modeling tool based on mineral-melt equilibria that describes the sequence of minerals that occur on the liquid line of descent during the crystallization of a given parental melt composition (Ghiorso, 1994; Ghiorso and Sack, 1995; Gualda et al., 2012; Ghiorso and Gualda, 2015). Modeling was done using MELTS v.1.2.0. Phases that were allowed to fractionate were olivine, orthopyroxene, clinopyroxene, feldspar, spinel, rhombohedral oxide, ortho-oxide, apatite, fluid, and melt. All MELTS runs started at the liquidus temperature, which ranges from 1070°C to 1156°C as determined by the program, and were allowed to run to 830°C at a 5°C increment. MELTS models were run at isobaric conditions at various pressures (0.5 kbar, 1 kbar, 2 kbar, 4 kbar, and 8 kbar) while fractionating solids. MELTS runs were also set to run along a specified oxygen buffer of QFM, QFM+1, QFM-1, QFM+2, and QFM-2.

Fractional crystallization was also tested using two other methods that both assume mass-balance: least squares mass-balance calculations and simple subtraction fractional crystallization. In least squares modeling, one performs a calculation of one magma fractionating into another and uses least squares to determine how closely the calculation fits with the observed compositions. The least squares residuals tell one

how well the data fits. Simple subtraction fractional crystallization modeling was done by starting with a representative basaltic andesite glass and fractionating from it various mineral assemblages based on the observed mineralogy and composition in 4 to 6 stages (Table 12). Simple subtraction is different from least squares calculations in that simple subtraction calculates the residual liquid whereas in least squares you must provide the composition. The hypothetical fractionating assemblage in each stage was based on petrographic observations of the basaltic andesite and estimations of mineral proportions. Mineral compositions are mineral chemistry from EPMA data.

4 Results

4.1 Petrography and Chemistry

4.1.1 Rhyodacite glass and phenocrysts

Rhyodacite Glass

Both the S-type and F-type rhyodacite pumice are very sparsely phyric with highly vesicular and microlite-free glass. Both the S-type and F-type rhyodacite are indistinguishable by major element glass chemistry. The S-type rhyodacite glass is 67 – 72 wt.% SiO_2, 0.5 – 1.2 wt.% MgO (0.5 – 0.7 wt.% MgO when not including the lapilli rhyodacite layers), 2 – 3 wt.% CaO, and 4 – 5 wt.% FeOt (Table 1, Fig. 5). The rhyodacite glass and the basal lapilli-rich rhyodacite layers have effectively identical glass chemistries, with a slightly wider range of MgO content in the basal lapilli-rich layers. The F-type rhyodacite glass is 65 – 71 wt.% SiO_2, 0.4 – 0.9 wt.% MgO, 2 – 3 wt.% CaO, and 4 – 6 wt.% FeOt (Table 1, Fig. 5, Appendix A1). Because the S-type and F-type rhyodacite glass and minerals appear texturally and compositionally similar, they will be described together and referred to as rhyodacite. Any differences between the different deposit types will be mentioned when applicable.

Table 1. Representative analyses of major element chemistry of glass in rhyodacite samples.
Abbreviations: S-type = Shishaldin-type, F-type = Fisher-type, RD = rhyodacite, n.a. = not analyzed
*Glass analyses done by Alaska Volcano Observatory (AVO) at USGS Menlo Park, CA.
⁺Glass analysis is not TDI-corrected the same as other glass analyses obtained at UCSB.
^Whole rock chemistry from Stelling (2003).

Sample	**97S-PS-34a**	**FC-175d**	**15S-PS-5e**	**FC-177b**	**15S-PS2i**
Analysis ID	34a_154*	175D_233*	15S-PS-5E_g4	177B_g9	PS-2l_g1
Description	S-type pumice RD	S-type pumice RD	S-type pumice RD	S-type lapilli-sized RD	S-type lapilli-sized RD
SiO_2	68.18	67.43	67.16	67.59	68.79
Al_2O_3	15.38	15.00	15.04	15.32	15.42
TiO_2	0.55	0.50	0.48	0.55	0.50
FeOt	4.29	4.08	4.32	4.08	4.24
MnO	0.25	0.21	0.19	0.19	0.22
MgO	0.68	0.61	0.63	0.61	0.57
CaO	2.37	2.30	2.35	2.10	2.23
Na_2O	5.25	5.71	6.18	6.73	5.24
K_2O	2.31	2.51	2.58	2.39	2.42
Cl	0.19	0.17	0.17	0.18	0.18
P_2O_5	0.24	0.21	0.18	0.18	0.19
Total	99.68	98.72	99.27	99.92	100.01
Mg #	22	21	21	21	19

Sample	**FC-06c**	**FC-183**	**FC-193**	**FC-155B**	**FC-155E**
Analysis ID	06c_91*	FC183_g4	FC-193_3⁺	FC-155B-2^	FC-155E-3^
Description	F-type pumice RD	F-type pumice RD	F-type pumice RD	F-type pumice RD	F-type pumice RD
SiO_2	68.93	67.07	67.64	67.13	65.97
Al_2O_3	15.12	15.50	15.66	15.29	15.18
TiO_2	0.45	0.71	0.75	0.64	0.69
FeOt	4.12	4.85	5.27	4.64	4.80
MnO	0.24	0.19	0.24	0.20	0.20
MgO	0.52	0.75	0.81	0.74	0.84
CaO	2.35	2.66	3.08	2.56	2.68
Na_2O	5.47	5.44	3.80	5.69	5.53
K_2O	2.41	2.34	2.11	2.32	2.31
Cl	0.20	0.12	0.13	n.a.	n.a.
P_2O_5	0.08	0.27	0.24	0.17	0.17
Total	99.89	99.89	99.73	99.37	98.36
Mg #	18	22	22	22	24

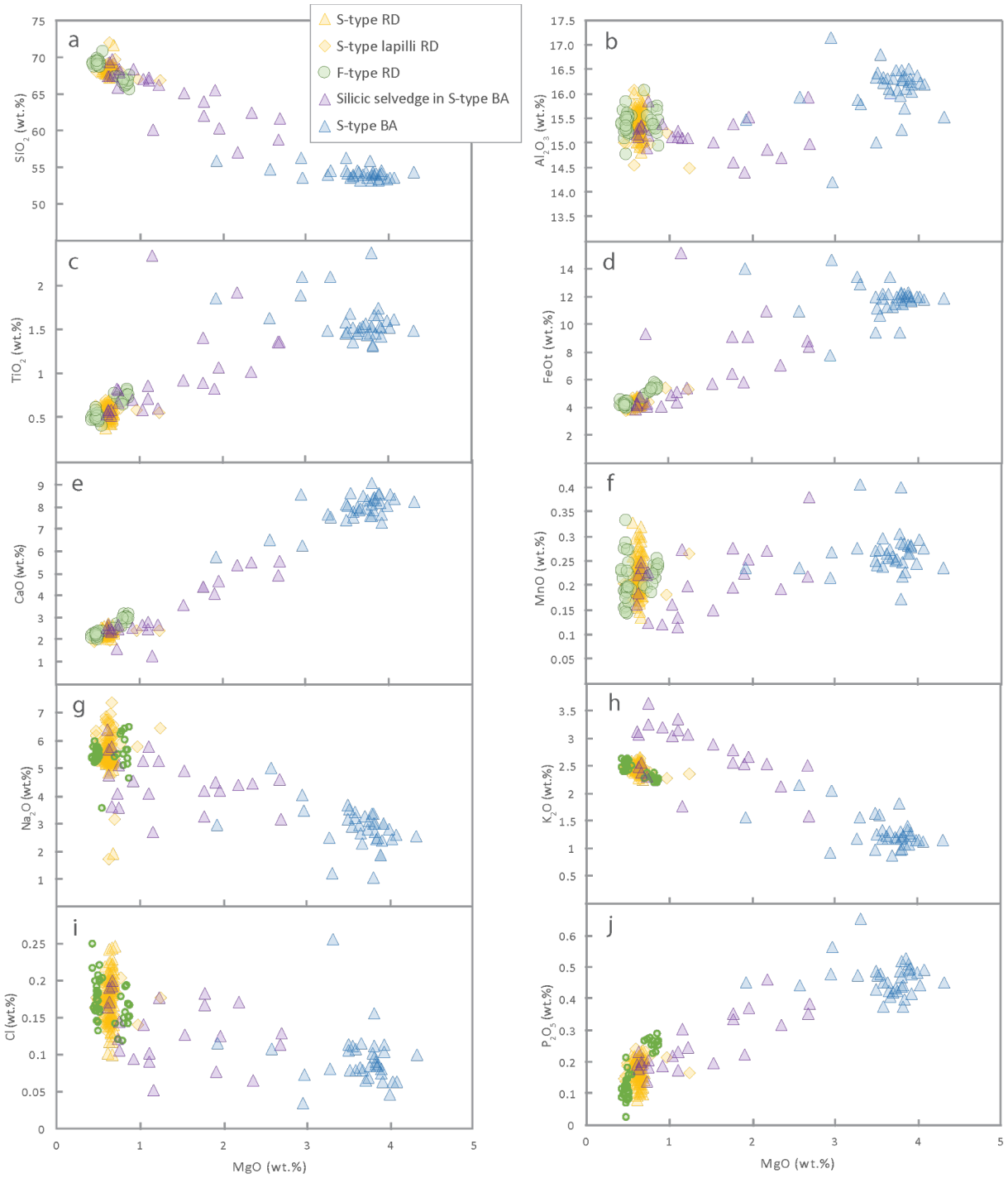

Figure 5. Glass chemistry of S-type and F-type samples in this study. Note the term "silicic selvedge" above. The silicic selvedge, which are minor portions of silicic glass within the basaltic andesite samples, is discussed in section 4.1.2.

Rhyodacite Plagioclase

Plagioclase (An_{54-26}) crystals have little compositional difference between core and rim in any given phenocryst or antecryst, which is a crystal that did not originally form in the host magma (Table 2; Appendix A3). Plagioclase crystals (Fig. 6a-c, 7, 8a-c) are the most abundant mineral in the rhyodacite. Plagioclase phenocrysts are euhedral and elongate or equant, and show simple or polysynthetic twinning. Melt and pyroxene inclusions occur within plagioclase phenocrysts. Some crystals show oscillatory zoning, although this is not consistent across all crystals and may suggest antecrystic origins. In some cases, zoning is only noticeable with cathodoluminescence. Euhedral plagioclase crystals contain a resorbed, CL-bright core followed by oscillations in CL-brightness ending with a rim that is darker than the core (Fig. 7).

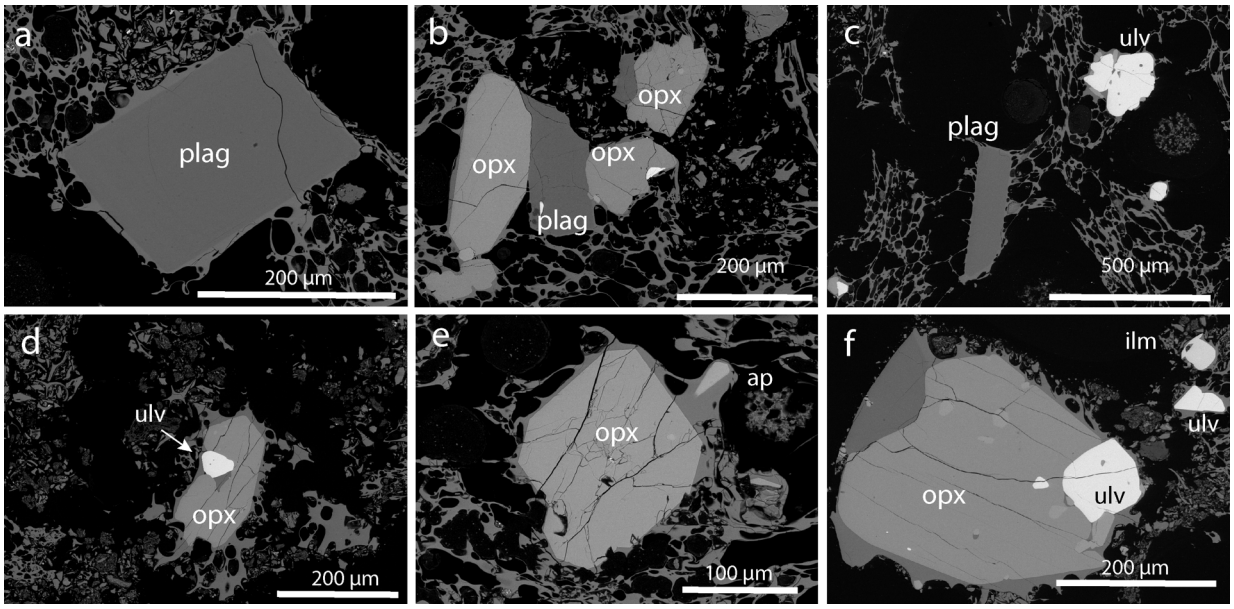

Figure 6. ***Fisher-type rhyodacite minerals*** Back-scatter electron (BSE) images of the S-type rhyodacite. Mineral abbreviations: olv = olivine, ilm = ilmenite, ulv = ulvöspinel, plag = plagioclase, cpx = clinopyroxene, opx = orthopyroxene, ap = apatite. **(a)** Euhedral plagioclase. [FC-183] **(b)** Aggregates of orthopyroxene and plagioclase. [FC-183] **(c)** Euhedral plagioclase with slightly resorbed ulvöspinel. [FC-193] **(d)** Orthopyroxene with ulvöspinel inclusion. [FC-193] **(e)** Euhedral orthopyroxene with small apatite. [FC-183] **(f)** Ilmenite-ulvöspinel pair near typical large orthopyroxene with ulvöspinel attached. [FC-193]

Table 2. Representative major element chemistry of rhyodacite minerals.
Mg# = $Mg^{2+}/(Mg^{2+} + Fe^{2+})*100$; Wo = $Ca/(Ca+Mg+Fe^{2+})*100$; En = $Mg/(Ca+Mg+Fe^{2+})*100$; Fs = $Fe^{2+}/(Ca+Mg+Fe^{2+})*100$
Abbreviations: S-type = Shishaldin-type, F-type = Fisher-type, RD = rhyodacite, BA = basaltic andesite, inter. = intermediate, ulv = ulvöspinel, opx = orthopyroxene, ap = apatite, plag = plagioclase, BSE = backscattered electron
*A crystal found within the basaltic andesite, but is from a silicic magma.

	Plagioclase				
Deposit type		S-type RD		F-type RD	
Analysis ID	175_plag5	175_plag6	175_plag7	183_plag16	183_plag17
Location	rim	int	core	rim	core
SiO_2	58.39	58.20	58.86	56.84	56.58
TiO_2	b.d.	0.03	0.03	0.07	0.06
Al_2O_3	26.88	26.45	26.43	26.88	27.09
FeOt	0.33	0.31	0.33	0.45	0.38
MnO	b.d.	b.d.	b.d.	0.04	b.d.
MgO	0.03	0.04	0.04	0.05	0.05
CaO	7.91	7.78	7.47	8.41	8.75
Na_2O	6.87	6.93	6.89	6.72	6.55
K_2O	0.27	0.28	0.28	0.22	0.22
Cr_2O_3	b.d.	b.d.	b.d.	b.d.	b.d.
Total	100.66	100.02	100.34	99.69	99.69
Ab	60.18	60.75	61.50	58.37	56.84
Or	1.54	1.61	1.67	1.27	1.24
An	38.28	37.65	36.83	40.35	41.93

	Olivine		
Deposit type	S-type RD	S-type RD	S-type RD
Sample	2I_px10	2I_px11	2I_px12
Location	rim	inter.	core
SiO_2	33.47	36.28	37.04
TiO_2	b.d	b.d	b.d
Al_2O_3	b.d	b.d	b.d
FeOt	42.72	28.72	27.98
MnO	1.74	0.95	0.79
MgO	19.97	33.09	33.35
CaO	0.23	0.17	0.17
Na_2O	b.d	b.d	b.d
K_2O	b.d	b.d	b.d
Cr_2O_3	b.d	b.d	b.d
Total	98.13	99.20	99.33
Mg #	45.5	67.3	68.0
Fo	44.5	66.5	67.4

	Orthopyroxene			
Deposit type	S-type RD	S-type RD	F-type RD	F-type RD
Analysis ID	34A_px3r	34A_px4c	183_px3r	183_px4c
Location	rim	core	rim	core
SiO_2	50.79	50.62	50.63	50.30
TiO_2	0.24	0.28	0.29	0.24
Al_2O_3	0.42	0.41	0.64	0.60
FeOt	26.78	27.57	25.30	26.95
MnO	1.78	1.73	1.37	1.50
MgO	17.00	16.89	18.68	17.30
CaO	1.76	1.77	1.82	1.86
Na_2O	0.02	0.02	0.03	0.02
K_2O	b.d	b.d	0.02	b.d
Cr_2O_3	b.d	b.d	b.d	b.d
Total	98.79	99.27	98.77	98.78
Mg #	53.4	53.1	58.5	54.7
Wo	3.8	3.8	3.9	4.0
En	51.3	51.1	56.2	52.5
Fs	44.9	45.1	39.8	43.4

	Clinopyroxene			
Deposit type	S-type RD	S-type RD	F-type RD	F-type RD
Analysis ID	5E_px1r	5E_px2c	06c_UN189c	06c_UN189r
Location	rim	core	core	rim
SiO_2	52.88	50.90	50.94	51.53
TiO_2	0.50	0.32	0.98	0.87
Al_2O_3	3.69	1.10	0.78	0.77
FeOt	12.71	15.38	18.69	16.64
MnO	0.85	1.17	1.50	1.29
MgO	10.62	12.36	12.36	11.81
CaO	16.34	17.50	15.19	17.55
Na_2O	0.91	0.30	0.23	0.24
K_2O	0.33	b.d	n.a.	n.a.
Cr_2O_3	b.d	b.d	b.d.	b.d.
Total	98.83	99.04	100.66	100.69
Mg #	59.8	61.0	55.4	56.1
Wo	39.8	38.3	32.9	37.5
En	36.0	37.6	37.2	35.1
Fs	24.2	24.1	29.9	27.4

Table 2. ***CONTINUED*** Representative analyses of Fe-Ti oxide pairs in rhyodacite. Temperature and fO_2 estimates provided here will be discussed in section 4.2.1.
n.a. = not analyzed, b.d. = below detection
^Ulv-Ilm pair that plots exactly on equilibrium line
*Ulv-Ilm coexisting pair

Deposit type	**Shishaldin-type**		**Fisher-type**	
Oxide Pair	34A_2 rim^	34A_11 core	193_4 rim*	193_7 core
Location	rim	core	rim	core
Ilmenite	UN37_148	UN37_97	193_ox3	193_ox4
%Ilm	91.70	93.50	92.06	93.01
FeOt	45.45	44.88	44.51	44.90
TiO_2	49.50	50.16	48.23	49.55
Al_2O_3	0.23	0.23	0.22	0.18
MgO	2.91	2.64	2.62	2.67
MnO	1.39	1.39	1.09	1.10
Cr_2O_3	0.03	b.d.	b.d.	0.03
V_2O_3	n.a.	n.a.	b.d.	0.38
SiO_2	0.05	0.03	0.03	b.d.
Total	99.56	99.33	96.71	98.81
Ulvöspinel	UN36_263	UN32_00	193_ox7	193_ox2
%Ulv	53.91	55.57	57.80	58.13
FeOt	75.02	73.64	70.13	70.53
TiO_2	18.91	19.27	19.01	19.39
Al_2O_3	2.07	1.94	2.08	2.05
MgO	1.81	1.80	1.74	1.82
MnO	1.17	1.12	0.92	0.94
Cr_2O_3	b.d.	b.d.	b.d.	b.d.
V_2O_3	n.a.	n.a.	0.04	0.10
SiO_2	0.07	0.10	0.13	b.d.
Total	99.04	97.87	94.07	94.83
Temperature	888	841	908	878
fO_2	-12.9	-14.2	-12.7	-13.4

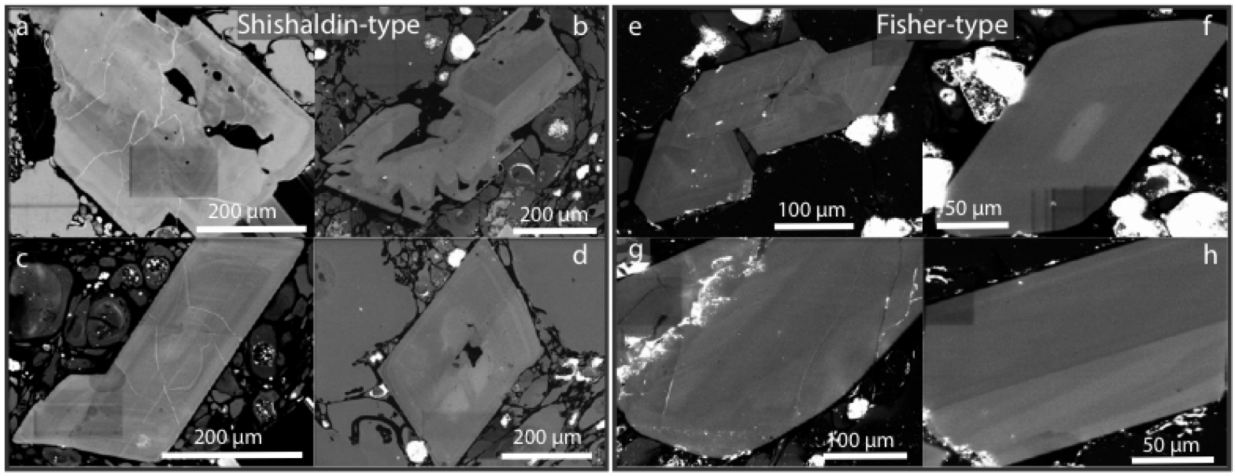

Figure 7. ***Cathodoluminescence textures of plagioclase in rhyodacite.*** A main pattern of a CL-bright, rounded core followed by CL-dark zones and ending with CL-bright rims. Some crystals show more complexity with resorbed zones (a, b). **(a-d)** S-type plagioclase CL textures **(e-h)** F-type plagioclase CL textures.

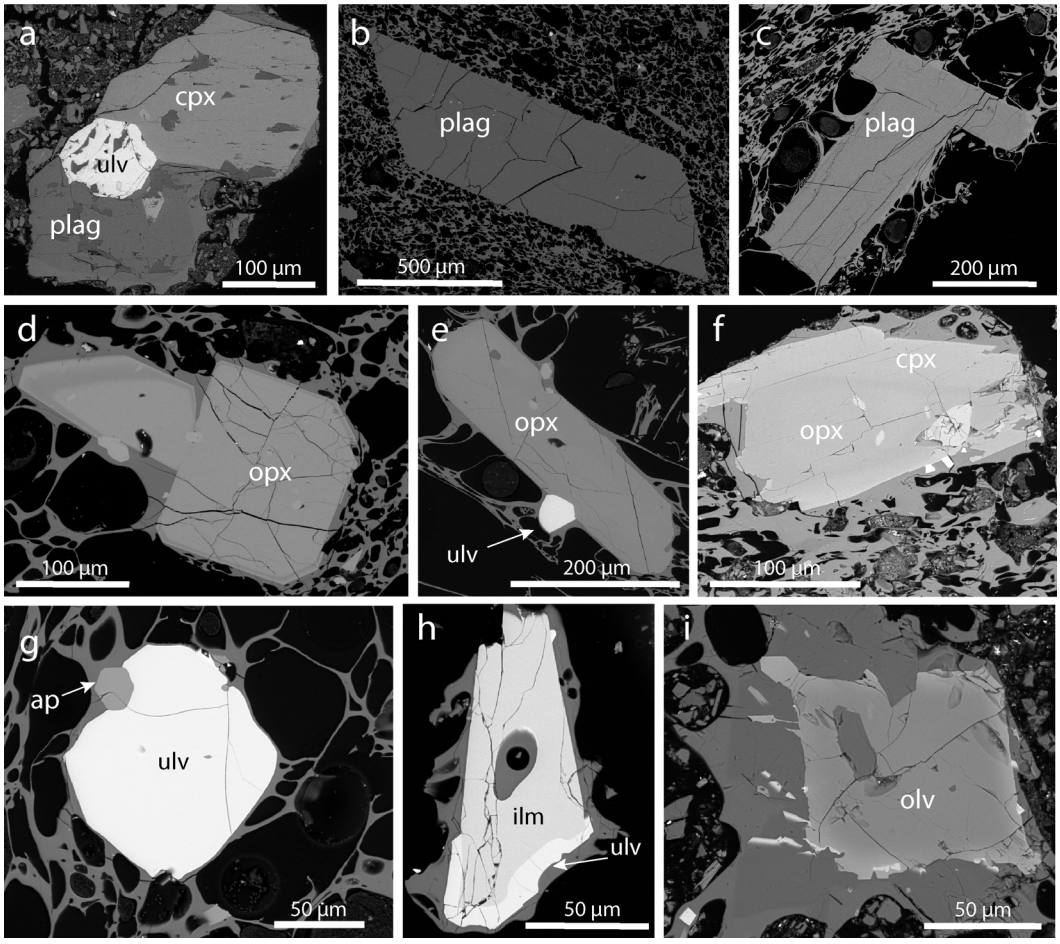

Figure 8. ***Shishaldin-type rhyodacite minerals*** Back-scatter electron (BSE) images of the S-type rhyodacite. Mineral abbreviations: olv = olivine, ilm = ilmenite, ulv = ulvöspinel, plag = plagioclase, cpx = clinopyroxene, opx = orthopyroxene, ap = apatite. **(a)** Typical aggregate of ulvöspinel-plagioclase-pyroxene (in this case clinopyroxene) **(b)** Euhedral plagioclase [FC-175]. **(c)** Euhedral plagioclase crystals [97S-PS-34a] **(d)** Euhedral orthopyroxene with the single BSE-darker zone near the rim [97S-PS-34a] **(e)** Orthopyroxene with ulvöspinel [97S-PS-34a] **(f)** Orthopyroxene in a clinopyroxene jacket with an apatite inclusion [lapilli layer 15S-PS-2i] **(g)** Ulvöspinel with apatite [97S-PS-34a] **(h)** Ulvöspinel-ilmenite pair [97S-PS-34a] **(i)** Resorbed olivine with compositional zoning and encased in slightly darker-BSE glass [lapilli layer 15S-PS-2i].

Rhyodacite Pyroxenes

The orthopyroxenes in the rhyodacite have compositions of $Wo_{6\text{-}0.25}$ $En_{70\text{-}45}Fs_{53\text{-}30}$ and compositions vary little within individual crystals (Table 2; Appendix A4). The orthopyroxenes have K_D(Fe-Mg) = 0.234±0.021 when the accepted K_D(Fe-Mg) for a rhyodacite glass composition is 0.242±0.06 (Putirka, 2008), thus orthopyroxenes are in chemical equilibrium using the Fe-Mg exchange. The orthopyroxenes are euhedral to subhedral (Fig. 6d-f, 8d-e), which suggests textural equilibrium with the rhyodacite glass, and are pale to medium brown.

The clinopyroxenes in the rhyodacite have compositions of $Wo_{41\text{-}30}$ $En_{44\text{-}34}$ $Fs_{35\text{-}21}$ (Table 2; Appendix A5). Clinopyroxenes are not in chemical equilibrium based on calculations of clinopyroxenes' observed components (DiHd=0.56-0.75, EnFs=0.20-0.36, and Jd=0.01-0.07) compared to the components of a clinopyroxene that would be in equilibrium with the rhyodacite glass (DiHd=0.33-0.54, EnFs=0.07-0.17, Jd=0.01-0.02; Putirka et al., 1996; Putirka, 1999). Clinopyroxenes are subhedral crystals that are pale to dark forest green. Clinopyroxene occurs as prismatic or elongate crystals and sometimes display simple twins. S-type clinopyroxenes are either part of aggregates of plagioclase and ulvöspinel or as isolated crystals that are partially resorbed. Clinopyroxenes are less common in F-type deposits and did not appear in the thin sections of F-type samples in this study.

Crystal aggregates composed of clinopyroxene or orthopyroxene, plagioclase, and ulvöspinel are found within the rhyodacite (Fig. 8a). Aggregates containing clinopyroxene have ulvöspinel inclusions partially within the clinopyroxene without disequilibrium textures, suggesting the ulvöspinel crystallized before clinopyroxene. Aggregates containing orthopyroxene, however have ulvöspinel crystallizing after the orthopyroxene or do not contain ulvöspinel. Clinopyroxenes within these aggregates do not have obvious signs of disequilibrium, unlike isolated phenocrysts of clinopyroxene. All crystals that are part of aggregates are generally subhedral and sometimes fragmented, but compositionally identical to their isolated phenocryst counterparts.

Rarely, crystals of orthopyroxene with a clinopyroxene rim (two examples) and clinopyroxene with an orthopyroxene rim (one example) occur within the S-type lapilli-rich rhyodacite (Fig. 8f). In one of these cases, the orthopyroxene is not in chemical equilibrium with the rhyodacite glass, but in the other two they

are in equilibrium. The orthopyroxene jacketed by clinopyroxene is fragmented and the orthopyroxene has a few small Fe-Ti oxides at the rim. In this case, the orthopyroxene is not in equilibrium with the rhyodacite glass. None of these zoned clinopyroxenes, whether rim or core, are in chemical equilibrium with the rhyodacite glass. This crystal (Fig. 8f) is therefore interpreted to be an antecryst, perhaps from assimilation of wall rock material.

A small population (n = 9) of small (~50 μm) euhedral to subhedral orthopyroxenes within the S-type rhyodacite contain a zone that is BSE-darker than the core and rim of other rhyodacite orthopyroxene, corresponding to a Mg# increase of ~2. This BSE-darker zone is 2.1 μm wide and is located 2.1 μm from the rim in a euhedral crystal cut perpendicular to a crystallographic axis (Fig. 8d). The zone is occasionally slightly resorbed. This zoning pattern is only found in the S-type rhyodacite, both the coarse pumice and the lapilli-rich layers. This small population is unlikely to be xenocrystic and shows heterogeneity within the rhyodacite magma rather than an important distinction between S-type and F-type deposits.

Rhyodacite Fe-Ti oxides

Ulvöspinel (X_{ulv} = 0.49-0.63; Table 2; Appendix A6; Fig. 6c, d, f; 8a, g, h) is the dominant Fe-Ti oxide species present in the rhyodacite, although rare ilmenite does occur (Table 2; Fig. 6f; 8h). Both species are in chemical equilibrium with each other based on the Bacon and Hirschmann (1988) test (section 4.2.1 and Fig. 13), but ulvöspinels that are not in equilibrium with the ilmenite do occur. Ulvöspinel crystals in partial contact with a vesicle show ilmenite exsolution lamellae that become more pronounced with proximity to the vesicle and are absent greater than 11 μm away from the vesicle. This texture may have developed after eruption and is likely a reaction with the vesicle gases. Fe-Ti oxides associated with clinopyroxene do not exhibit disequilibrium textures. Ulvöspinel in both F-type and S-type samples are sometimes attached to orthopyroxene or part of aggregates of plag+pyx+ulv (Fig. 6d, f; Fig. 8a). Ilmenite in the S-type rhyodacite pumice was found in contact with ulvöspinel (Fig. 8h) and in the F-type pumice a separate ilmenite crystal nearby an ulvöspinel crystal was found (Fig. 6f).

Rhyodacite Olivine

A single subhedral crystal of olivine (Fo_{67} core to Fo_{45} rim; Table 2; Appendix A7) was found within the S-type rhyodacite with apparent compositional zoning (Fig. 8i). The olivine is surrounded by glass that is BSE-

darker, suggesting it is more Fe-poor (no chemical analysis available), than the majority of rhyodacite glass. In this way, the glass surrounding the olivine is zoned by the more Fe-poor glass closer to the crystal and typical rhyodacite glass further from the crystal. This olivine crystal also has small, anhedral Fe-Ti oxides at the rim of the olivine and within the BSE-darker glass. The core of the olivine crystal is similar to the composition of olivines found in the basaltic andesite. The rim of the olivine crystal is not in equilibrium with the silicic glass with respect to Mg# (K_D Fe-Mg = 0.344), but is only slightly outside of the accepted K_D (Fe-Mg) range of 0.30 ± 0.03 (Roeder and Emslie, 1970).

Olivines were also found in mineral separates of F-type rhyodacite samples, but not in thin section. Therefore, no EPMA data exist for these minerals. Bindeman et al. (2001) reported olivine within the F-type rhyodacite of Fo_{33}. Several fragmented crystals of pale yellow-green olivine were separated from the F-type sample FC-183, but the combined mass was insufficient for oxygen isotope analyses.

Apatite

Minor apatite microphenocrysts are present in the rhyodacite as small, euhedral, stubby crystals. Apatites also occur as inclusions within plagioclase, orthopyroxene, clinopyroxene, and ulvöspinel. As inclusions, apatite generally appears acicular with fractures that run the full length of the crystal, indicating rapid growth. Inclusions of apatite can occur when the melt around the margins of growing crystals become temporarily oversaturated in P_2O_5 (Harrison and Watson, 1984).

4.1.2 Basaltic andesite glass and phenocrysts

Basaltic Andesite Glass

Chemically, the basaltic andesite glass has 52 – 54 wt.% SiO_2, ~3.5 – 4 wt.% MgO and an average Mg# of ~36 (ranging between 20 and 42; Table 3; Appendix A2). The basaltic andesite glass has networks of coarse microlites, but small basaltic andesite glass pockets are found between microlites. The only larger, microlite-free zones in the basaltic andesite samples are the thin silicic selvedges of rhyodacite glass that surround many crystals.

Microlites within all basaltic andesite glasses are composed of predominantly Fe-Ti oxides and plagioclase with minor pyroxenes. Microlites in basaltic andesite from F-type deposits show more variability

in textures than those in S-type deposits. Some areas have fans of coarse plagioclase laths whereas other areas have finer-grained microlites. The S-type basaltic andesite contains a dense network of microlites with small blebs of silicic selvedge interspersed. F-type basaltic andesite also contains microlite-free areas surrounding rhyodacite-derived crystals but not all rhyodacite crystals are surrounded by silicic selvedge. In the F-type basaltic andesite, the rhyodacite-derived crystals have very coarse microlites surrounding them that are dominated by coarser-grained plagioclase microlites instead of silicic selvedge (Fig. 9a). Direct comparisons between the F-type and S-type basaltic andesites are challenging because the F-type basaltic andesite is much more intermingled with the rhyodacite than the S-type basaltic andesite.

The S-type basaltic andesite has silicic selvedges, which sometimes contain crystals but are other times individual blebs of rhyodacite glass. The glass within silicic selvedges is more felsic than the basaltic andesite glass, ranging from ~59 to 69 wt.% SiO_2. At its most silicic, the selvedge is compositionally identical to the rhyodacite glass. The glass analyses of the silicic selvedges form a mixing line between the basaltic andesite glass and the rhyodacite glass (Fig. 5). Generally, the thinner the selvedge, the less silicic the glass is within the selvedge. The minerals within the selvedges are sometimes in equilibrium with the selvedge glass and not in equilibrium with the basaltic andesite glass. Fe-Ti oxide crystals surrounded by silicic selvedge show ilmenite exsolution, indicating disequilibrium between the selvedge and the ulvöspinels. Orthopyroxenes that are surrounded by a selvedge, however, do not show disequilibrium textures yet the

Table 3. Representative major element chemistry of glass in basaltic andesite samples.
Abbreviations: S-type = Shishaldin-type, RD = rhyodacite, BA = basaltic andesite

Sample	**97S-PS-34b**	**15S-PS-5b**	**15S-PS-2c**	**97S-PS-34b**	**97S-PS-34b**	**15S-PS-2c**
Analysis ID	34b_g10	15S-PS-5B_mfgl6	15S-PS-2C_g5	34b_g5	34b_g1	15S-PS-2C_g1
Description	Scoria glass	Scoria glass	Scoria glass	Silicic glass in scoria	Silicic glass in scoria	Silicic glass in scoria
SiO_2	52.71	52.91	54.75	66.92	61.56	68.71
Al_2O_3	15.31	16.65	15.66	15.12	15.30	15.00
TiO_2	2.04	1.66	1.42	0.59	0.89	0.58
FeOt	12.44	10.54	9.21	4.87	9.08	4.20
MnO	0.39	0.27	0.30	0.16	0.27	0.22
MgO	3.20	3.51	3.71	1.04	1.75	0.62
CaO	7.33	8.53	7.48	2.64	4.35	2.38
Na_2O	1.17	2.86	3.28	5.24	3.22	4.69
K_2O	1.51	1.59	1.77	3.03	2.53	2.45
Cl	0.25	0.11	0.10	0.14	0.16	0.19
P_2O_5	0.63	0.48	0.48	0.22	0.35	0.23
Total	96.99	99.10	98.14	99.96	99.47	99.28
Mg #	31	37	42	28	26	21

single orthopyroxene analyzed is not in chemical equilibrium with the selvedge glass. This orthopyroxene is in chemical equilibrium with a representative rhyodacite glass. The crystals enveloped in silicic selvedges are interpreted to have resulted from mingling with the CFE rhyodacite. The volume of this silicic material within the basaltic andesite component is likely small given that it does not affect the whole rock chemistry relative to the basaltic andesite glass chemistry.

Basaltic Andesite Plagioclase

S-type plagioclase phenocrysts are less abundant and smaller (~100 μm) than the other basaltic andesite phenocrysts (clinopyroxene, olivine, and ulvöspinel). S-type plagioclase crystals have compositions An_{85-32} in the basaltic andesite scoria (Fig. 10b-c; 11b; Table 4; Appendix A3). However, only An_{60-32} plagioclase are in equilibrium with the mafic melt. Some of the plagioclases are surrounded by a selvedge of rhyodacite glass, which is likely the more albitic plagioclase compositions but the previous analyses done by Stelling (2003) included did not specify the context of each analysis.

The F-type basaltic andesite contains large (~500 μm) plagioclase crystals from the rhyodacite that have a sharp compositional change at the rim, marked by a BSE-darker zone (Fig. 9a-d), suggesting lower Fe content. These crystals have large resorption areas within the crystal and along its rim, suggestive of disequilibrium (Fig. 9b, d). These plagioclase crystals are not surrounded by silicic selvedge but the large resorption textures suggest they are not native to the basaltic andesite. The F-type basaltic andesite chemistry is not shown or analyzed in this study because this study focuses on deposits that are not in the ignimbrite.

Basaltic Andesite Pyroxenes

All orthopyroxenes in the basaltic andesite are euhedral to subhedral and are surrounded by a selvedge of microlite-free rhyodacite glass (Fig. 10d). The orthopyroxenes (Wo_4 En_{51-52} Fs_{44-46}; Table 4; Appendix A4), are in chemical equilibrium with the rhyodacite and are not in equilibrium with the rhyodacite selvedge surrounding the crystals or the basaltic andesite glass. The major element chemistry of orthopyroxenes in the basaltic andesite match the composition of orthopyroxenes in the rhyodacite. There is little variation in core to rim compositions of orthopyroxenes.

Clinopyroxenes (Table 4; Appendix A5) are stubby or equant and occur with and without rhyodacite selvedges. Major element chemistry of clinopyroxenes (Fig. 11a) surrounded by a selvedge of silicic glass

matches the compositions of those in the co-erupted rhyodacite. Clinopyroxenes without a selvedge (Wo_{40-46} En_{39-46} Fs_{11-15}, $Mg\#_{cpx}$ 73-81) are in chemical equilibrium with the basaltic andesite glass; those crystals with a selvedge (Wo_{35-41} En_{35-40} Fs_{21-24}, $Mg\#_{cpx}$ 59-65) are not in equilibrium with the basaltic andesite glass. The basaltic andesite glass would be in equilibrium with clinopyroxene components of DiHd=0.77, EnFs=0.19-0.20, Jd=0.01. Clinopyroxenes without selvedge have components of DiHd=0.77-0.78, EnFs=0.18, and Jd=0.02, whereas clinopyroxenes with selvedge have components of DiHd=0.59-0.75, EnFs=0.19-0.32, and Jd=0.01-0.03. Clinopyroxenes with $Mg\#_{cpx}$ >76 exhibit sector zoning (Fig. 10e). Core and rim compositions are nearly identical in clinopyroxenes.

Basaltic Andesite Fe-Ti oxides

Ulvöspinel (Table 4; Appendix A6) is common in both S-type and F-type basaltic andesite as both phenocrysts and non-native crystals. Ilmenite is not observed. Isolated ulvöspinel crystals occur both with and without silicic selvedges. Ulvöspinels in the S-type basaltic andesite that have silicic selvedges either contain exsolution lamellae of ilmenite (Fig. 10f) or exhibit other disequilibrium textures, such as rounding or resorption (Fig. 10g). Ulvöspinel crystals without silicic selvedges do not show ilmenite exsolution, are euhedral, and are sometimes attached to olivines as a co-crystallizing phase (Fig. 10h, i) within the S-type basaltic andesite. Ulvöspinels from F-type basaltic andesite are euhedral (Fig. 9e). Some F-type ulvöspinels are rounded or resorbed (Fig. 9j) but do not exhibit ilmenite exsolution. Sometimes the ulvöspinels in the F-type deposits are not surrounded by selvedge, but are too rounded to be from the basaltic andesite and contain apatite, which does not crystallize in the basaltic andesite.

The ulvöspinels that are phenocrysts of the basaltic andesite have compositions of X_{ulv} = 0.26-0.27. The ulvöspinels with disequilibrium textures are compositionally similar to rhyodacite ulvöspinels, which is X_{ulv} = 0.49-0.63, based on rough EDS estimates. Ulvöspinels from the F-type basaltic andesite are euhedral and their fraction ulvöspinel (~0.25 X_{ulv}) is lower than those from the rhyodacite (~0.70 X_{ulv}).

Basaltic Andesite Olivine

Olivine is present in both the S-type and F-type basaltic andesite and is typically pale yellow-green and euhedral to subhedral (Fig. 9k; 10h-j; 11c). One olivine in the F-type basaltic andesite, however, contains ulvöspinel inclusions but is also euhedral. Some olivines have ulvöspinels attached. Olivines are never

surrounded by silicic selvedge. Basaltic andesite olivines have compositions of Fo_{73-71} (Table 4; Appendix A7). The majority of olivine crystals are in chemical equilibrium with the basaltic andesite glass, based on criteria established by Roeder and Emslie (1970).

Basaltic Andesite Apatite

Although apatite is observed in basaltic andesite samples, apatite crystals only occur within rhyodacite glass selvedges. Apatite is also observed as inclusions within plagioclase and clinopyroxene crystals, but only in host crystals that are surrounded by rhyodacite glass selvedges. No apatite inclusions are found within crystals in chemical equilibrium with basaltic andesite glass.

Table 4. Representative major element chemistry of basaltic andesite minerals.
Mg# = $Mg^{2+}/(Mg^{2+} + Fe^{2+})*100$; Wo = $Ca/(Ca+Mg+Fe^{2+})*100$; En = $Mg/(Ca+Mg+Fe^{2+})*100$; Fs = $Fe^{2+}/(Ca+Mg+Fe^{2+})*100$
Abbreviations: S-type = Shishaldin-type, F-type = Fisher-type, RD = rhyodacite, BA = basaltic andesite, inter. = intermediate, ulv = ulvöspinel, opx = orthopyroxene, ap = apatite, plag = plagioclase, BSE = backscattered electron
*A crystal found within the basaltic andesite, but is from a silicic magma.

	Plagioclase		
Deposit type	S-type BA	S-type BA	S-type BA
Sample	2C_plag1	2C_plag2	2C_plag3
Location	rim	int	core
Description	euhedral, small, equant, microlites up to xtl rim		
SiO_2	52.43	51.21	52.08
TiO_2	0.05	0.06	0.07
Al_2O_3	29.53	29.14	29.60
FeOt	1.08	0.68	0.63
MnO	b.d.	0.03	b.d.
MgO	0.20	0.12	0.10
CaO	12.22	11.84	12.15
Na_2O	4.56	4.80	4.40
K_2O	0.12	0.11	0.11
Cr_2O_3	b.d.	b.d.	b.d.
Total	100.18	97.98	99.15
Ab	40.04	42.08	39.30
Or	0.67	0.62	0.67
An	59.30	57.29	60.03

	Orthopyroxene*		
Deposit type	S-type BA	S-type BA	S-type BA
Sample	34b_px9r*	34b_px10i*	34b_px11c*
Location	rim	inter.	core
SiO_2	50.47	50.25	50.41
TiO_2	0.23	0.19	0.18
Al_2O_3	0.52	0.48	0.40
FeOt	27.04	27.13	27.89
MnO	1.60	1.67	1.72
MgO	17.06	16.84	16.65
CaO	1.87	1.81	1.75
Na_2O	0.03	0.04	0.02
K_2O	0.01	b.d.	b.d.
Cr_2O_3	b.d.	b.d.	b.d.
Total	98.83	98.40	99.02
Mg #	53.9	53.5	52.6
Wo	4.1	4.0	3.8
En	51.7	51.4	50.6
Fs	44.2	44.6	45.6

	Ulvöspinel	
Deposit Type	S-type BA	S-type BA
Sample	5B_ox3	5B_ox4
Location	rim	core
Description	euhedral, attached to olv1-2, ~100 µm long	
SiO_2	0.03	0.09
TiO_2	8.46	8.80
Al_2O_3	5.41	5.39
FeOt	74.94	74.39
MnO	0.31	0.31
MgO	3.93	3.96
CaO	0.01	b.d.
Na_2O	b.d.	b.d.
K_2O	b.d.	b.d.
Cr_2O_3	0.19	0.14
V_2O_3	0.81	0.89
NiO	b.d.	b.d.
Total	94.09	93.97
Ulv fraction	0.26	0.27

	Clinopyroxene			
Deposit type	S-type BA	S-type BA	S-type BA	S-type BA
Sample	34b_px5r	34b_px6c	34b_px7r	34b_px8c
Location	rim	core	rim	core
Description	sector-zoned, BSE-dark zone		sector-zoned, BSE-lighter zone	
SiO_2	50.04	51.41	46.49	48.57
TiO_2	0.83	0.63	1.64	1.32
Al_2O_3	3.03	2.09	6.38	4.62
FeOt	10.50	8.47	10.83	9.56
MnO	0.29	0.24	0.28	0.24
MgO	15.19	15.63	12.83	14.00
CaO	18.47	20.36	19.58	20.39
Na_2O	0.21	0.25	0.32	0.35
K_2O	b.d.	0.02	0.02	b.d.
Cr_2O_3	b.d.	b.d.	b.d.	b.d.
Total	98.56	99.09	98.37	99.05
Mg #	75.9	80.7	75.9	79.8
Wo	39.9	43.0	45.4	45.5
En	45.6	46.0	41.4	43.5
Fs	14.5	11.0	13.2	11.0

	Clinopyroxene*		
	S-type BA	S-type BA	S-type BA
	2C_px1-rim*	2C_px2-core*	2C_px3-rim*
	rim	core	rim
	large, splintery, subhedral, fragmented, w/ long apatite inclusion		
	50.78	50.91	50.41
	0.45	0.32	0.40
	1.53	0.96	1.00
	13.76	14.84	14.49
	0.93	1.03	1.05
	12.31	11.88	12.63
	18.53	18.57	18.35
	0.32	0.29	0.29
	b.d	b.d	b.d
	b.d	b.d	b.d
	98.62	98.81	98.62
	62.8	60.5	64.9
	40.4	40.5	40.4
	37.4	36.0	38.7
	22.1	23.5	20.9

	Olivine	
Deposit type	S-type BA	S-type BA
Sample	34b_olv1	34b_olv2
Location	rim	core
SiO_2	37.25	37.36
TiO_2	b.d	b.d
Al_2O_3	0.02	b.d
FeOt	25.50	26.04
MnO	0.48	0.46
MgO	35.75	35.82
CaO	0.25	0.19
Na_2O	0.02	b.d
K_2O	b.d	b.d
Cr_2O_3	b.d	b.d
Total	99.28	99.86
Mg #	71.4	71.0
Fo	71.0	70.7

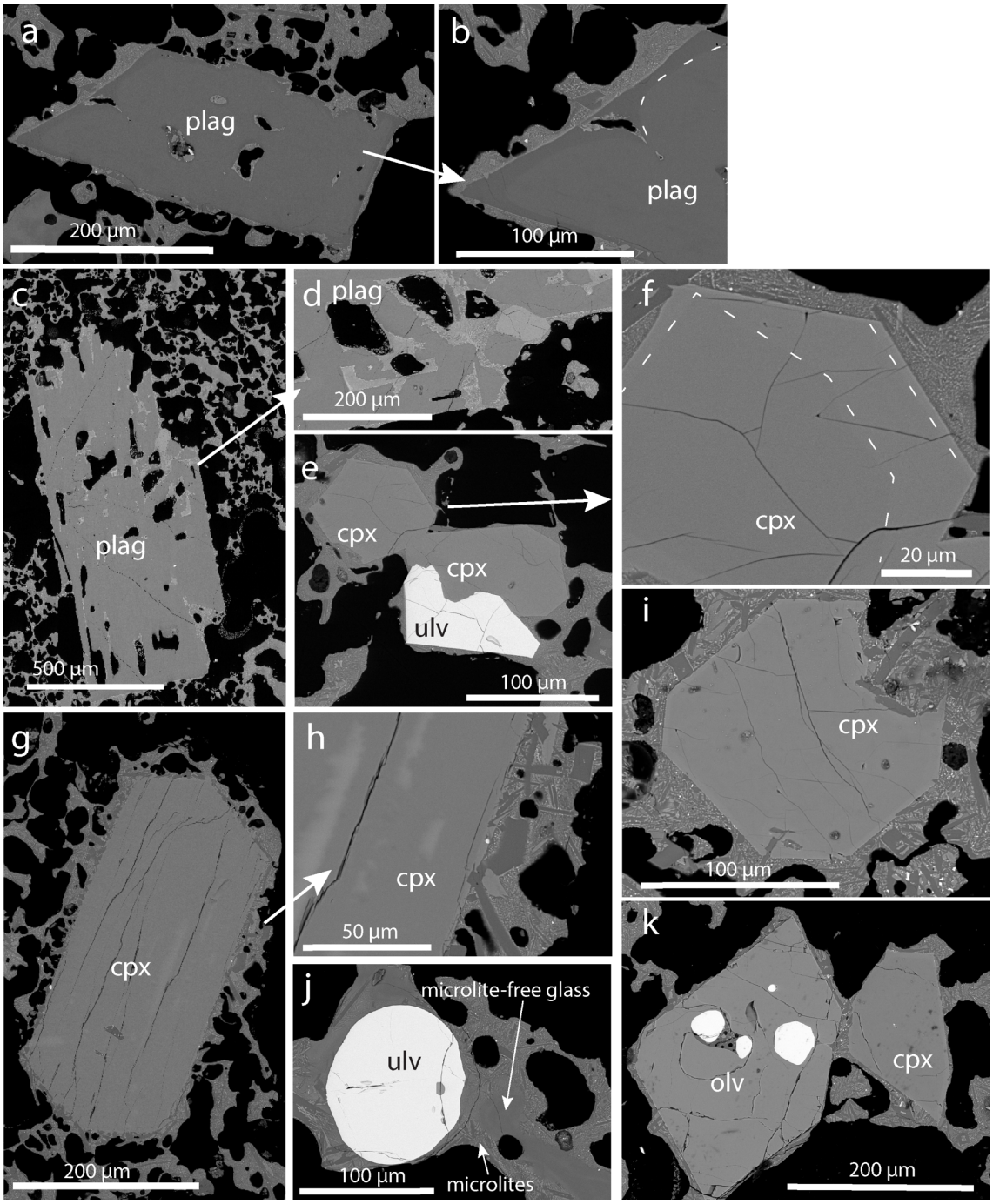

Figure 9. ***Fisher-type basaltic andesite minerals and textures*** Back-scatter electron (BSE) images of the F-type basaltic andesite (BA). Mineral abbreviations: olv = olivine, ilm = ilmenite, ulv = ulvöspinel, plag = plagioclase, cpx = clinopyroxene, opx = orthopyroxene, ap = apatite. **(a)** Resorbed plag with coarse sieve texture and a BSE-darker rim. **(b)** Close up of (a) with the compositionally-different and resorbed rim of plag. **(c)** Resorbed plag with coarse sieve texture. **(d)** Close up of resorbed plag in (c). Microlite-rich glass is within the crystal. **(e)** Euhedral cpx and ulv likely BA-derived. **(f)** Close up of cpx with subtle compositional zoning shown by the dashed white lines. **(g)** Cpx with rim slightly resorbed and coarser microlites around the rim. **(h)** Close up of cpx from (g) showing the coarser plag microlites at the rim. **(i)** Resorbed cpx with slightly BSE-lighter rim. **(j)** Rounded ulv with microlite=free glass and microlite-rich glass. **(k)** Subhedral olv with ulv inclusions and near a cpx.

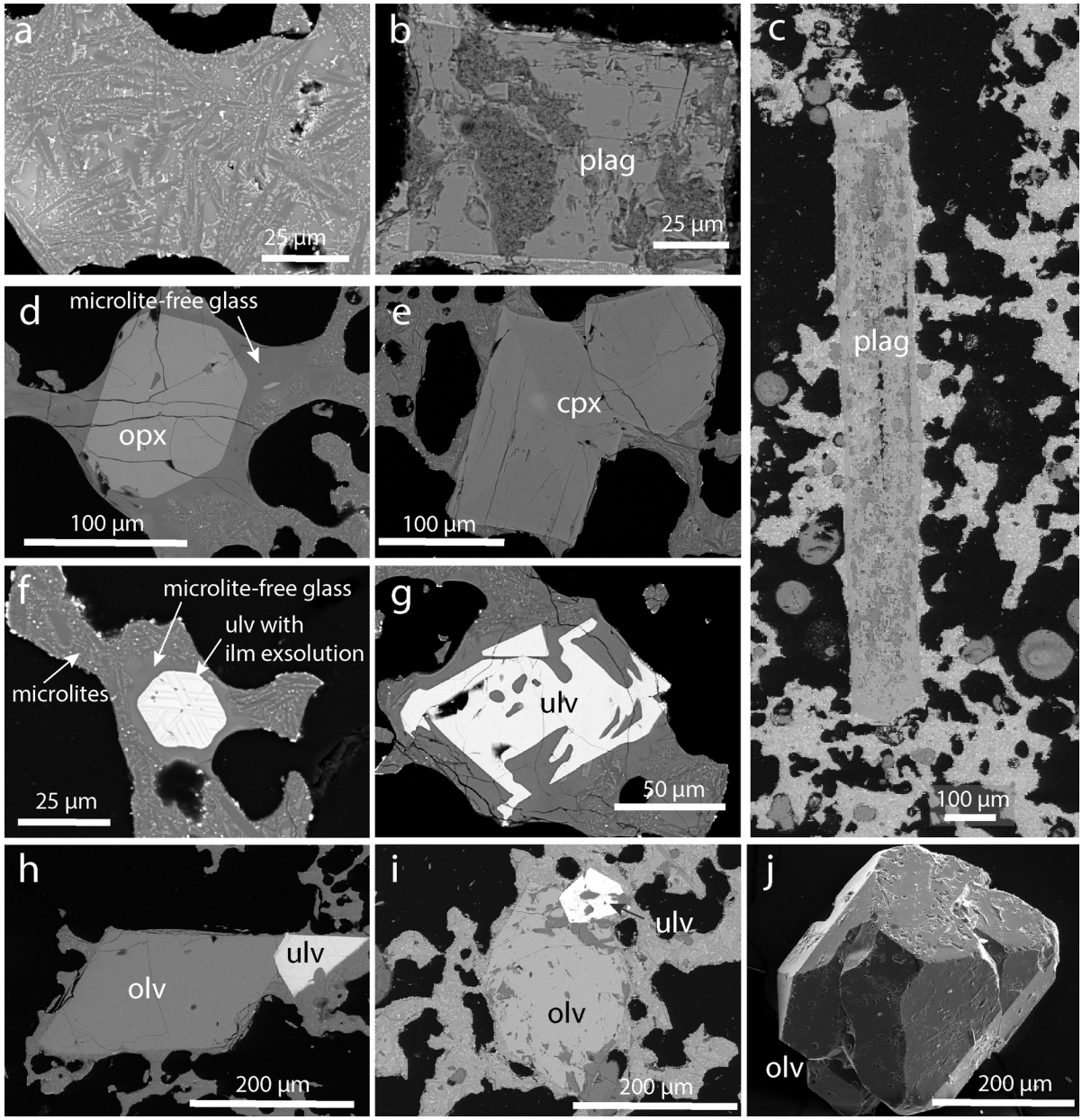

Figure 10. ***Shishaldin-type basaltic andesite minerals and textures*** Back-scatter electron (BSE) images of the S-type basaltic andesite. Mineral abbreviations: olv = olivine, ilm = ilmenite, ulv = ulvöspinel, plag = plagioclase, cpx = clinopyroxene, opx = orthopyroxene, ap = apatite. **(a)** Typical texture of the microlite-rich basaltic andesite glass within the discrete basaltic andesite scoria fall layer. [97S-PS-34b] **(b)** Euhedral, equant plagioclase. [15S-PS-2c] **(c)** The only instance of a long, thin plagioclase crystal with coarse sieve texture of microlite-free glass. [15S-PS-2b] **(d)** Orthopyroxene surrounded by silicic selvedge (microlite-free glass), which is surrounded by microlite-rich basaltic andesite glass. [97S-PS-34b] **(e)** Sector-zoned, euhedral clinopyroxene crystals in equilibrium with basaltic andesite glass. The crystal also shows penetration twinning and the sector continues to the other crystal. [97S-PS-34b] **(f)** Ulvöspinel with ilmenite exsolution encased in silicic selvedge. [97S-PS-34b] **(g)** Resorbed ulvöspinel surrounded by silicic selvedge. [97S-PS-34b] **(h)** Olivine in equilibrium with basaltic andesite glass and attached to an ulvöspinel. [97S-PS-34b] **(i)** Euhedral olivine with attached ulvöspinel. [15S-PS-2b] **(j)** SEM image of crystal separate of subhedral olivine. [15S-PS-2c]

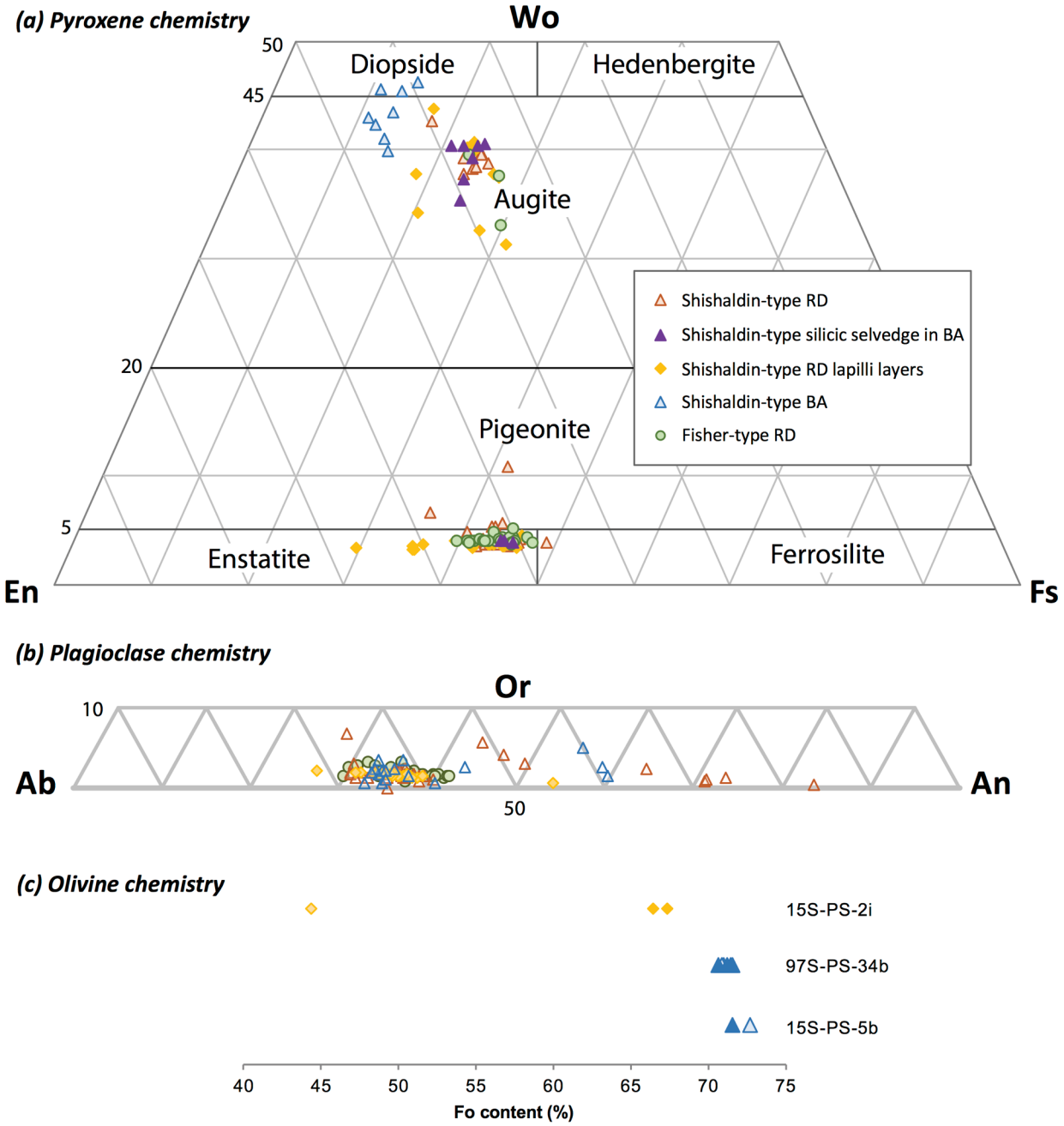

Figure 11. Chemistry of major mineral phases, symbolized by the host glass composition: (a) pyroxenes, (b) plagioclase, and (c) olivine. In (c), the filled symbols represent core compositions and the empty symbols represent rim compositions. Abbreviations: RD=rhyodacite, BA=basaltic andesite.

4.1.3 Summary of petrography and chemistry

The S-type and F-type rhyodacite samples are very similar with identical glass textures and chemistry as well as identical mineral compositions. The rhyodacite contains phenocrysts of plagioclase, orthopyroxene, ulvöspinel, ilmenite, and apatite (Table 5). The rhyodacite contains a few clinopyroxene and olivine crystals that are not in equilibrium with the rhyodacite glass. These crystals are interpreted to be antecrystic. The S-type rhyodacite shows greater heterogeneity in pyroxene textures, e.g., zoning textures, compared to the F-type rhyodacite, but this is interpreted to be showing heterogeneity within the rhyodacite magma rather than a distinguishing characteristic between S-type and F-type deposits.

The basaltic andesite contains phenocrysts of plagioclase, clinopyroxene, olivine, and ulvöspinel (Table 5). Phenocrystic plagioclase crystals are generally smaller than the plagioclase contained in silicic selvedges. Clinopyroxenes sometimes exhibit sector zoning. Phenocrystic olivines are usually associated with ulvöspinel crystals. The S-type basaltic andesite component contains small silicic selvedges with crystals at its center. The minerals that are generally enclosed in silicic selvedges in the basaltic andesite are plagioclase, orthopyroxene, clinopyroxene, and ulvöspinel and have compositions identical to their counterparts in the rhyodacite. The F-type basaltic andesite is only found within the ignimbrite and thus has very different, more complex textures, such as coarser microlites surrounding certain crystals and a compositionally different rim on large plagioclase crystals.

Table 5. Summary of Minerals Present in Co-erupted Magmas.
n.a. = not analyzed, * indicates microphenocryst, antecryst = crystal that is not a phenocryst but from recharge magmas or wall rock

Deposit type	Phenocrysts	Composition	Antecrysts	Composition
Rhyodacite	Plagioclase	An 54 - 26	Clinopyroxene	Wo 41-30 En 44-34 Fs 35-21
	Orthopyroxene	Wo 6-0.25 En 70-45 Fs 53-30	Olivine	Fo 67-45
	Ulvöspinel	Ulv 49-63		
	Ilmenite	Ilm 91.7 - 93.5		
	Apatite*	n.a.		
Basaltic Andesite	Plagioclase	An 60-59	Plagioclase	An 43-31
	Clinopyroxene	Wo 40-46 En 39-46 Fs 11-15	Orthopyroxene	Wo 4 En 51-52 Fs 44-46
	Olivine	Fo 73-71	Clinopyroxene	Wo 35-41 En 35-40 Fs 21-24
	Ulvöspinel	Ulv 26-27	Ulvöspinel	n.a.
			Apatite	n.a.

4.1.4 Evidence for magma mingling

There are multiple lines of evidence for mingling between the rhyodacite and basaltic andesite, which are two dissimilar and potentially immiscible melts just prior to eruption. The S-type deposits characteristically have a ~10 cm thick zone of banded pumice between the rhyodacite and basaltic andesite pumice deposits. Although the F-type deposits lack this zone, banded pumice are present in the overlying ignimbrite. Within the S-type banded pumice, the rhyodacite glass is microlite-free, with fewer, smaller vesicles than the basaltic andesite glass (Fig. 12a). Crenulated margins show that the two melts were still liquid when they interacted (Fig. 12b). The basaltic andesite glass within the banded pumice is not as microlite-rich as in the discrete scoria fall deposit, but contains clumps of microlites and otherwise microlite-free basaltic andesite glass in the

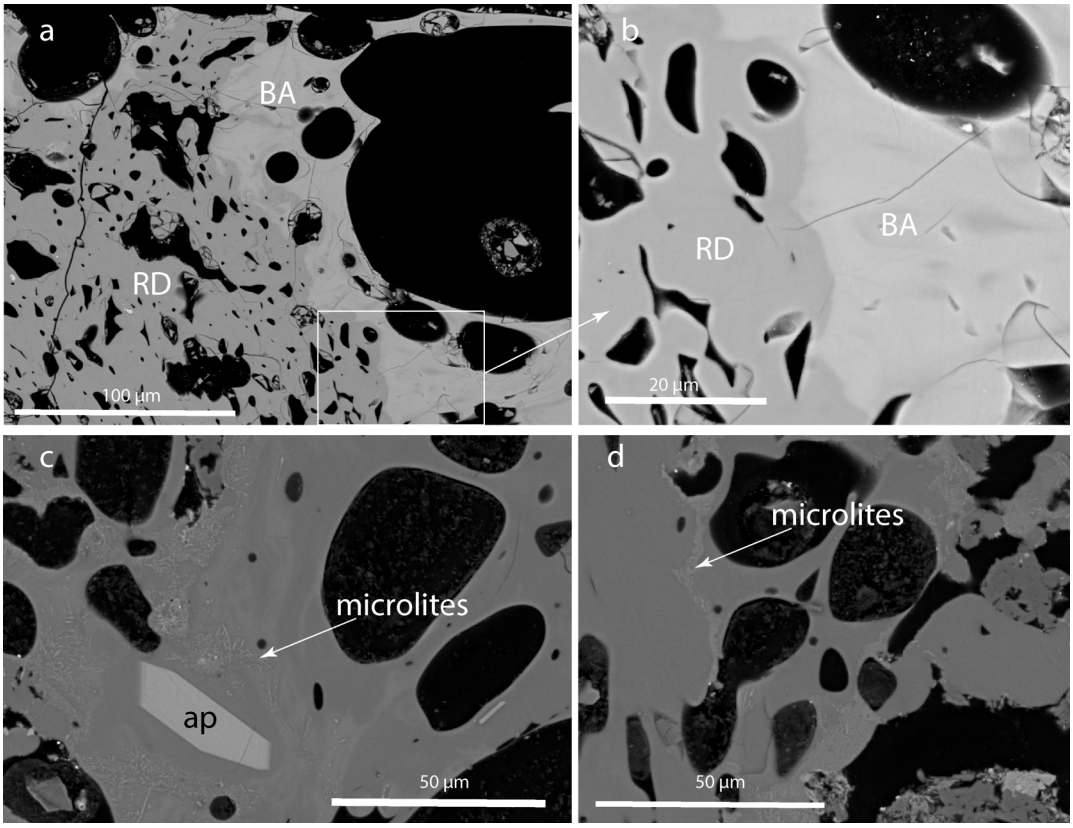

Figure 12. ***S-type banded pumice mingling textures.*** **(a-b)** BSE image of mingling zone with rhyodacite (BSE-darker, labeled RD) on the left and basaltic andesite on the right (BSE-brighter, labeled BA). Vesicle differences are noticeable with the basaltic andesite comprised of larger coalesced vesicles as they have the remains of glass walls and the rhyodacite made up of higher concentrations but smaller vesicles. Area in white box is shown in (b). **(b)** Sharp, crenulate margins along some boundaries. **(c)** BSE images of the banded pumice show that the basaltic andesite glass is not as microlite-rich as the basaltic andesite glass in the basaltic andesite samples. Microlites do occur in isolated clumps or in small zones. ap = apatite **(d)** Crenulate margins between basaltic andesite glass and rhyodacite glass. Microlites are less densely spaced and finer-grained than the microlites in the basaltic andesite samples.

banded pumice (Fig. 12c). Fine-grained microlites also form along the crenulate margins of basaltic andesite glass between the darker-BSE rhyodacite glass (Fig. 12d). Another line of evidence for mingling are the sub-mm blebs, or silicic selvedges, of rhyodacite that are present in the basaltic andesite part of the S-type eruption.

The F-type banded pumice is a lot more chaotic and more crystal-rich (still low volume percent of crystals), very different from the S-type banded pumice, but this may be a result of overturn in the magma chamber prior to the eruption of the ignimbrite. The F-type deposit basaltic andesite is only in the ignimbrite, so identifying the rhyodacite-derived components is a little more difficult. Generally, rhyodacite crystals mingled with the F-type ignimbrite are rounded, resorbed, or have compositional changes at the rims.

4.2 Pre-eruptive Conditions: T-P-fO_2

4.2.1 Rhyodacite pre-eruptive conditions

Pre-eruptive temperature and oxygen fugacity using two-oxide thermobarometry

The most precise, last equilibrated thermometer available for the rhyodacite is the two-oxide thermometer. Of the 22 thin sections of samples from 10 field sites, two contain both ilmenite and ulvöspinel. One thin section from 97S-PS-34a (S-type rhyodacite) contains a single crystal of ilmenite (Table 2) that is in equilibrium (based on methods described by Bacon and Hirschmann (1988); Fig. 13a) with four isolated ulvöspinel crystals and one ulvöspinel crystal in contact with the ilmenite (Fig. 9a). An F-type rhyodacite sample (FC-193) contains a single crystal of ilmenite that is ~20 μm away from an ulvöspinel crystal that is in equilibrium with the ilmenite (Fig. 7a; Table 2). Results from the Andersen and Lindsley geothermometer (Fig. 13b; Table 2) applied to rim compositions in both ilmenite and ulvöspinel yield 877 - 908ºC (± 33°C; n = 7; Table 6). However, the Andersen and Lindsley (1985) thermometer underestimates temperatures >860°C (Blundy and Cashman, 2008), so the rhyodacite temperature may have been hotter than the estimates calculated using this method. The Ghiorso and Evans (2008) method produces similar temperature estimates of 887 - 911°C (±44°C; n =5) for the S-type and 907 - 908°C (±44°C; n = 2) for the F-type (Table 6). The single, coexisting two-oxide pair found in FC-193 gave a temperature estimate of 908°C whereas the S-type two-oxide pair yielded 888°C for the pair that plots on the equilibrium line in the Bacon and Hirschmann

(1988) test. These are the temperatures that will be used for plagioclase hygrometry because one is a coexisting pair and the other plots best in the equilibrium test.

Oxygen fugacity estimates for S-type rhyodacite range between -13.1 and -12.5 log units [-13.1 to -12.6 log units using Andersen and Lindsley (1985) and -12.9 to -12.5 log units using Ghiorso and Evans (2008); Table 6]. The F-type rhyodacite rim pairs have a range of oxygen fugacities of -12.7 to -12.6 log units [-12.7 log units using Andersen and Lindsley (1985) and -12.6 log units using Ghiorso and Evans (2008)]. Because the two methods provide similar results, only the Andersen and Lindsley results will be mentioned from this point. The single, coexisting two-oxide pair found in FC-193 gave an oxygen fugacity of -12.7 whereas the S-type two-oxide pair yielded an fO_2 of -12.9 log units.

The cores of the two-oxide pairs yield a lower temperature estimate than the rims. However, whether the actual core of the oxides was analyzed is uncertain because the exact orientation of the crystal within the thin section is unknown. Although all core pairs passed the Bacon and Hirschmann (1988) test, the core pre-eruptive temperature estimates are treated with caution.

Table 6. Two-oxide thermometry and oxygen barometry results. Temperatures and fO_2 calculated according to Andersen and Lindsley (1985) using the Stormer (1983) solution model and Ghiorso and Evans (2008).
^Ulv-Ilm pair that plots exactly on equilibrium line
*Ulv-Ilm coexisting pair

Shishaldin-type			Andersen and Lindsley (1985)		Ghiorso and Evans (2008)	
Pair	**Mol % Usp**	**Mol % Ilm**	**T (°C)**	**log10 fO_2**	**T (°C)**	**log10 fO_2**
Pair 34A_2*^ rim	53.91%	91.70%	888	-12.9	898	-12.7
Pair 34A_4 rim	55.99%	91.70%	904	-12.6	910	-12.5
Pair 34A_5 rim	52.46%	91.70%	877	-13.1	887	-12.9
Pair 34A_6 rim	55.82%	91.70%	903	-12.7	911	-12.5
Pair 34A_7 rim	55.30%	91.70%	898	-12.7	906	-12.5
	average		894	-12.8	902	-12.6
	st dev		11	0.2	10	0.2
Pair 34A_10 core	58.17%	93.50%	860	-13.9	861	-13.9
Pair 34A_11 core	55.57%	93.50%	841	-14.2	845	-14.2
Pair 34A_12 core	54.57%	93.50%	834	-14.3	838	-14.3
Pair 34A_13 core	56.01%	93.50%	844	-14.2	842	-14.2
	average		845	-14.1	847	-14.2
	st dev		11	0.2	10	0.2
Fisher-type			Andersen and Lindsley (1985)		Ghiorso and Evans (2008)	
Pair	**Mol % Usp**	**Mol % Ilm**	**T (°C)**	**log10 fO_2**	**T (°C)**	**log10 fO_2**
Pair193_1 rim	57.43%	92.06%	905	-12.7	907	-12.6
Pair193_4* rim	57.80%	92.06%	908	-12.7	908	-12.6
	average		907	-12.7	908	-12.6
	st dev		2	0.0	1	0.0
Pair193_7 core	58.13%	93.01%	878	-13.4	878	-13.4
Pair193_8* core	59.31%	93.01%	888	-13.2	886	-13.2
Pair193_10* core	58.63%	93.01%	883	-13.3	881	-13.3
	average		883	-13.3	882	-13.3
	st dev		5	0.1	4	0.1

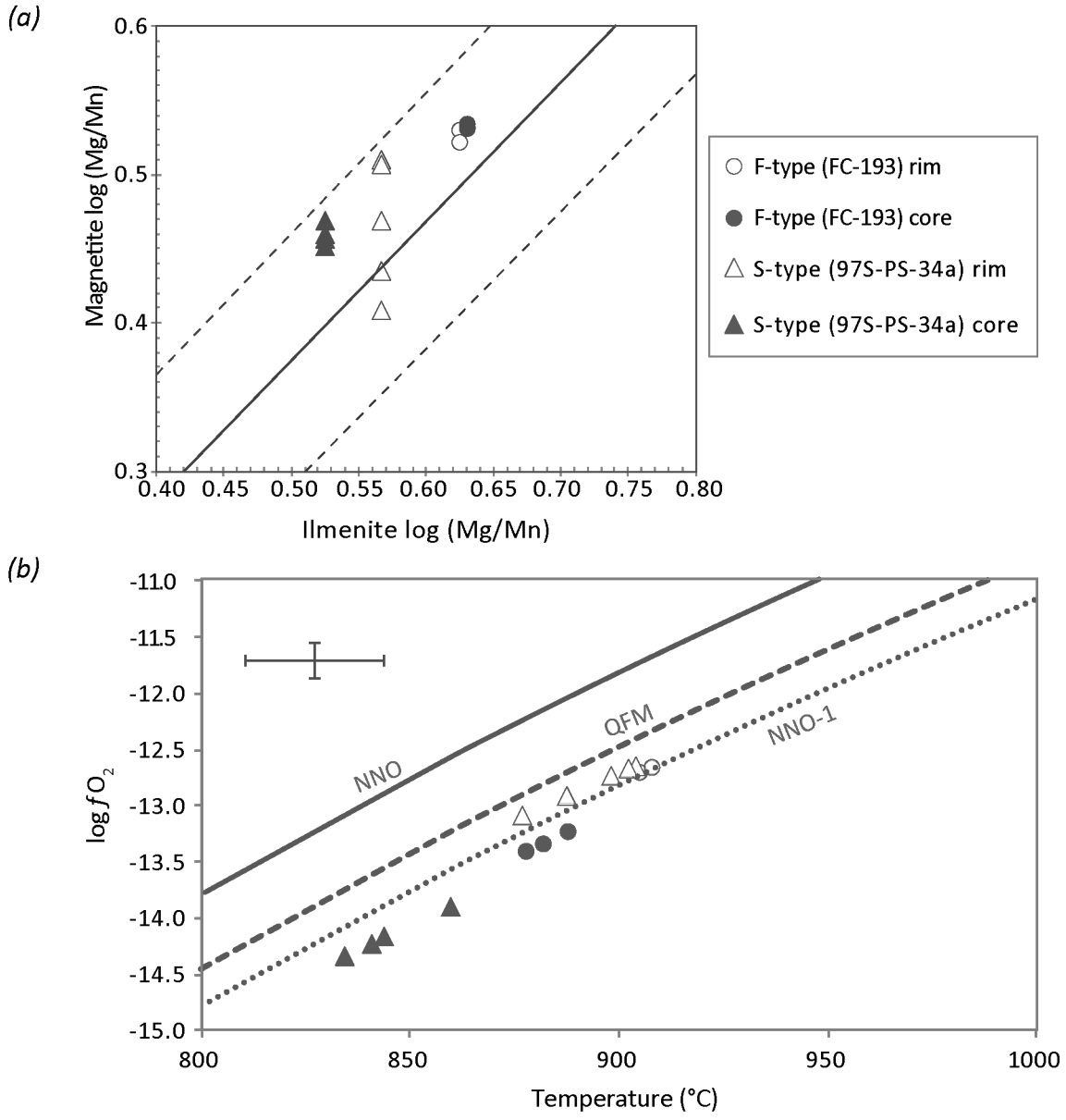

Figure 13. ***Two-oxide thermometry and oxygen barometry.*** **(a)** Bacon and Hirschmann (1988) test for two-oxide pairs. Ideal equilibrium is shown by the solid line and the dashed lines indicate the full accepted equilibrium range. **(b)** Two-oxide thermometry and oxygen barometry results using Andersen and Lindsley (1985). Oxygen buffers are plotted for 200 MPa (~2 kbar). Error bars correspond to the average absolute deviation (aad) of ±33°C and the max aad of ±0.34 log units for the oxygen barometer.

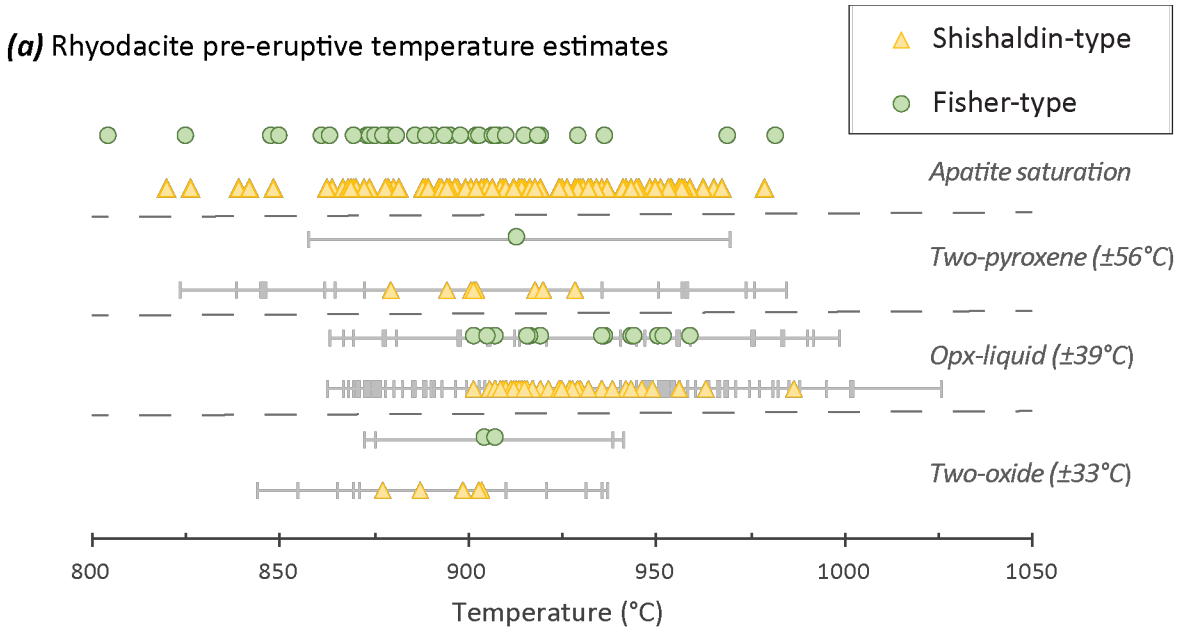

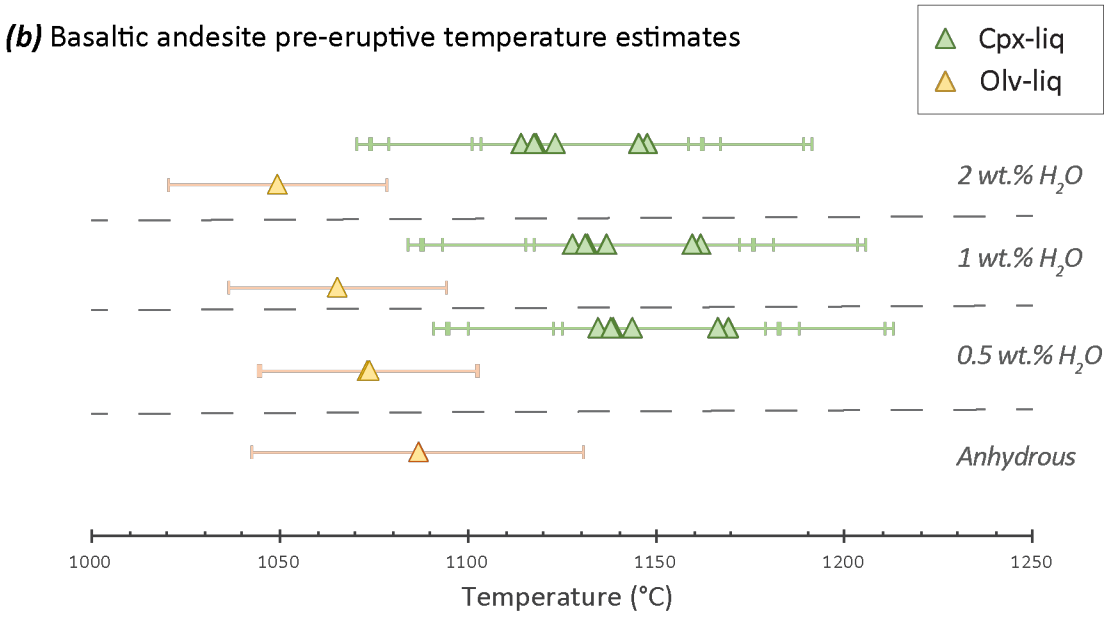

Figure 14. Thermometry results and comparison for the **(a)** rhyodacite and **(b)** basaltic andesite. For the basaltic andesite, H_2O content has a slight impact on the pre-eruptive temperature, but the effect is within error of the thermometer. Abbreviations: opx = orthopyroxene, cpx = clinopyroxene, olv = olivine.

Pre-eruptive temperature and pressure using pyroxene geothermobarometry

Orthopyroxene-liquid (Table 7) and two-pyroxene (Table 8) thermometers were used to estimate the pre-eruptive temperature of the rhyodacite. The orthopyroxene-liquid thermometer requires an estimation of H_2O content in the liquid. A water content of 4 wt.% H_2O was used based on the results of plagioclase hygrometer calculations and two-oxide thermometry was used as a temperature input for the hygrometer to resolve the circular problem (section 4.3).

The orthopyroxene-liquid thermometry calculations yield nearly identical temperature estimate ranges for S-type (901 – 987°C; ±39°C) and for F-type rhyodacites (902 – 960°C; ±39°C). The two-pyroxene thermometer yields a slightly lower temperature range of 879 – 928°C (±56°C) for the S-type rhyodacite and 914°C for the F-type rhyodacite but shows generally good agreement between the thermometers (Fig. 14a).

Pressure estimates based on orthopyroxene-liquid and two-pyroxene equilibrium yield a wide range of values for magma storage depth (Fig. 15). Based on orthopyroxene-liquid barometry, the S-type pairs yield 2.4 – 10.7 kbar (±2.6 kbar) and F-type pairs are 2.0 – 6.0 kbar, which overlap with each other. Two-pyroxene barometry yields -0.63 – 8.2 kbar for the S-type and 10.3 kbar (±3.2 kbar) for F-type.

The pressure ranges estimated for the two deposit types is all over the crust, even including a negative pressure. The negative pressure could imply the magma was within the edifice of a volcano prior to eruption. However, if one includes the 1σ error bar on that pressure estimate, then it does have a positive pressure of ~2.6 kbar. Hence this negative pressure estimate could represent a magma within the shallow crust prior to eruption. In Putirka's (2008) model calibration for the orthopyroxene-liquid barometer, negative pressure estimates arise for melts that have low pre-eruptive pressures (≤5 kbar). Assuming an average crustal density of 2.6 g/cm^3, the orthopyroxene-liquid barometer results provide a range of 0 – 42 km depth, suggesting that the rhyodacite was stored somewhere in the crust. The huge range in pressures is not useful for this study since it is already known an evolved magma must originate in the crust.

Temperature of rhyodacite when apatite saturates

The apatite saturation temperature estimates for the rhyodacite have a wider range than the other geothermometers in this study. S-type samples yield a range of apatite saturation temperatures from 820°C to

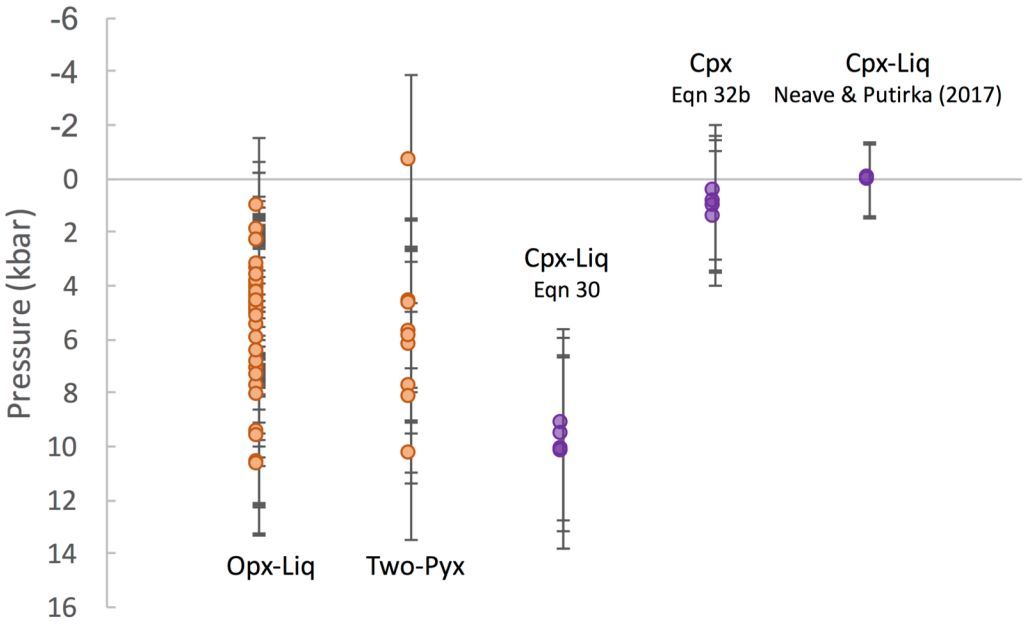

Figure 15. Pressure estimates from mineral-liquid thermobarometry for the rhyodacite (in orange) and for the basaltic andesite (in purple).

979°C with an average and standard deviation of 913 ± 33°C (n = 96). The F-type samples have an apatite saturation temperature that ranges from 805°C to 982°C with an average of 892 ± 34°C (n = 38). Both F-type and S-type apatite saturation temperature results overlap due to similar glass chemistries. Although the apatite saturation temperature estimates have a wide spread, these results have significant overlap with and are comparable to the two-oxide and pyroxene-based geothermometer results, so the apatite saturation thermometer is consistent with the other temperature estimates (Fig 14a). The wide range in temperature estimates is a result of the heterogeneity of the glass chemistry.

Rhyodacite pre-eruptive temperature and pressure summary

The pre-eruptive temperature of the rhyodacite is 877 – 908°C (±33°C), based on the most precise technique applied (two-oxide thermometer). Because Fe-Ti oxides equilibrate rapidly, this temperature estimate is more likely to provide estimates that represent temperatures immediately prior to eruption. Other mineral-liquid thermometers overlap with this range, but extend to higher temperatures. These higher temperatures may be the result of earlier stages of crystallization as pyroxenes and plagioclase are slower to equilibrate with the surrounding melt than Fe-Ti oxides. The error bars on the rhyodacite temperature estimates are still separate enough from the basaltic andesite temperature estimates to distinguish between the pre-eruptive temperatures

of the two magmas. Apatite saturation thermometer calculations overlap other calculated pre-eruptive temperatures, but the broad range of temperature estimates (979-820°C; error unknown) make these estimates less useful and are not considered further in this study. The range of apatite saturation temperature estimates is likely due to the heterogeneity of the glass compositions themselves since the calculation is solely dependent on glass chemistry and would likely correlate with the glass compositions. The geobarometers that were usable in this study have very large SEEs that span most of the crust and will not be considered further. Also, the two-pyroxene thermobarometer is likely not a good calculation to use for the rhyodacite because clinopyroxene is not in equilibrium with the rhyodacite even though it passes the equilibrium test for this thermobarometer with orthopyroxene pairs.

Table 7. Temperatures and pressures calculated using the orthopyroxene-liquid thermobarometer of Putirka (2008).
The standard error of estimate (SEE) for the thermometer is ±39°C and ±2.6 kbar for the barometer.
Mg# = $Mg^{2+}/(Mg^{2+} + Fe^{2+})*100$

Deposit type	Sample	Opx Analysis ID	Glass Analysis ID	opx Mg#	Wo	En	Fs	Temp °C	Pressure (GPa)	Pressure (kbar)
Shishaldin-type	15S-PS-2I	2I_px4 rim	2I_g8	53.9	4.1	51.7	44.2	956	1.0	9.5
		2I_px20 rim	2I_g18	53.5	3.5	51.7	44.8	944	0.7	7.4
		2I_px22 rim	2I_g19	57.5	4.0	55.1	40.8	963	1.1	10.7
	15S-PS-5E	5E_px3 rim	5E_g4	56.0	4.0	53.8	42.2	930	0.5	4.8
		5E_px5 rim	5E_g4	57.7	4.9	54.9	40.2	939	0.7	6.9
		5E_px7 rim	5E_g5	55.0	3.9	52.9	43.2	924	0.3	3.4
	97S-PS-34A	34A_px3 rim	AVO 34A-151	53.4	3.8	51.3	44.9	913	0.2	2.4
		34A_px5 rim	AVO 34A-151	55.8	4.2	53.5	42.3	921	0.2	2.4
		34a_UN62 rim	AVO 34A-151	55.2	3.7	53.2	43.1	915	0.3	3.0
		34a_UN64 rim	AVO 34A-151	55.6	3.9	53.4	42.7	963	0.8	8.3
		34a_UN66 rim	AVO 34A-151	55.9	3.8	53.7	42.4	916	0.4	3.6
		34a_UN68 rim	AVO 34A-151	53.5	10.9	47.7	41.4	987	0.9	9.4
		34a_UN71 rim	AVO 34A-151	55.7	3.7	53.6	42.6	914	0.4	3.9
		34a_UN72 rim	AVO 34A-151	56.7	3.5	54.7	41.8	936	0.5	5.2
	FC-175	175_px8 rim	AVO 175d_220	53.9	5.7	50.9	43.5	929	0.5	4.8
		175_px10 rim	AVO 175d_220	52.6	3.7	50.7	45.6	914	0.4	4.1
	FC-177B	177B_px2 rim	177B_g2	52.3	3.3	50.5	46.1	912	0.4	4.5
		177B_px3 rim	177B_g2	53.8	3.6	51.9	44.5	915	0.4	4.4
		177B_px7 rim	177B_g2	56.9	3.9	54.7	41.4	932	0.4	3.9
		177B_px9 rim	177B_g4	55.2	3.8	53.1	43.1	917	0.4	4.5
		177B_px13 rim	177B_g7	53.2	3.8	51.2	45.1	915	0.5	4.6
		177B_px14 inter.	177B_g7	53.3	3.8	51.3	44.9	908	0.5	4.6
Fisher-type	FC-06c	06c_UN183 rim	AVO 06c_91	54.6	4.6	52.1	43.3	920	0.4	4.0
		06c_UN184 rim	AVO 06c_91	52.7	3.6	50.8	45.6	917	0.4	4.2
		06c_UN185 rim	AVO 06c_91	52.5	4.2	50.4	45.5	908	0.2	2.0
		06c_UN187 rim	AVO 06c_91	52.6	3.8	50.6	45.6	906	0.2	2.4
		06c_UN188 rim	AVO 06c_91	52.5	3.7	50.5	45.8	916	0.5	4.7
	FC-183	183_px1 rim	183_g1	57.0	3.9	54.8	41.3	944	0.4	4.0
		183_px3 rim	183_g2	58.5	3.9	56.2	39.8	951	0.5	5.0
		183_px5 rim	183_g3	56.9	3.8	54.8	41.4	953	0.6	6.0

Table 8. Temperatures and pressures calculated using the two-pyroxene thermobarometer of Putirka (2008.
Observed K_D(Fe-Mg) for two-pyroxene pairs should be 1.09 ± 0.14.
The standard error of estimate (SEE) for the thermometer is ±56°C and ±3.2 kbar for the barometer.
Mg# = Mg^{2+} /(Mg^{2+} + Fe^{2+})*100

Deposit type	Sample	Pyroxene	Analysis ID	Mg#	Location	Wo	En	Fs	K_D(Fe-Mg)	Temp °C	Pressure (kbar)
Shishaldin-type	15S-PS-2I	Augite	2I_px8	62	intermediate	40.7	36.2	23.1	1.04	894	-0.63
		Orthopyroxene	2I_px2	63	intermediate	3.5	59.5	37.0			
		Augite	2I_px15	52	core	29.7	35.7	34.6	1.07	918	7.82
		Orthopyroxene	2I_px5	54	intermediate	3.6	50.6	45.8			
		Augite	2I_px7	57	rim	31.3	38.0	30.7	0.97	920	6.3
		Orthopyroxene	2I_px22	56	rim	3.8	52.7	43.4			
		Augite	2I_px13	56	rim	36.8	34.5	28.8	0.99	879	8.21
		Orthopyroxene	2I_px23	57	intermediate	3.4	55.1	41.4			
		Augite	2I_px14	56	intermediate	36.4	34.4	29.3	1.10	901	5.82
		Orthopyroxene	2I_px24	58	core	3.9	54.5	41.6			
		Augite	2I_px15	52	core	29.7	35.7	34.6	1.16	902	4.65
		Orthopyroxene	2I_px22	56	rim	3.8	52.7	43.4			
		Augite	2I_px18	58	rim	39.1	34.8	26.2	1.13	902	4.76
		Orthopyroxene	2I_px24	58	core	3.9	54.5	41.6			
Shishaldin-type	15S-PS-5E	Augite	5E_px2	59	core	36.8	36.2	27.1	1.17	928	5.93
		Orthopyroxene	5E_px6	60	core	6.3	55.1	38.6			
Fisher-type	FC-06c	Augite	06c_UN189	55	core	32.9	37.2	29.9	0.97	914	10.32
		Orthopyroxene	06c_UN183	54	core	3.8	52.2	43.9			
		Average								906	6
		Standard deviation								15	3

4.2.2 Basaltic andesite pre-eruptive conditions

Only the clinopyroxene-liquid (Table 9) and olivine-liquid (Table 10) methods could be used to estimate the temperature of the basaltic andesite (Fig. 14b) due to the lack of ilmenite and the chemical disequilibrium between orthopyroxene and the mafic magma (section 4.1.2, Table 5). Both olivine and clinopyroxene are phases within the basaltic andesite that are in chemical equilibrium with the basaltic andesite and do not show any disequilibrium textures. Because these thermometers require an estimate of water content and the hygrometer requires a temperature estimate (section 4.3), these calculations are less straightforward. However, variations in water content estimates do not have a significant effect on the calculated temperature. For the clinopyroxene-liquid thermometer, there is a 14°C difference between the calculated temperatures when 1 wt.% H_2O and 2 wt.% H_2O are used as inputs, well within the 45°C error of the model. For the olivine-liquid thermometer the difference between those same temperature calculations with 1 and 2 wt.% H_2O is 16°C, which is also within the 29°C error of the thermometer.

The clinopyroxene-liquid thermometer yields temperature ranges of 1135 – 1169°C (±45°C) using 0.5 wt.% H_2O, 1128 – 1162°C using 1 wt.% H_2O, and 1114 – 1147°C using 2 wt.% H_2O (Fig. 14b). Two olivine crystals were found to be in equilibrium with the basaltic andesite. The olivine-liquid thermometer

yields an estimate of 1089°C (0.5 wt.% H_2O), 1081°C (1 wt.% H_2O), and 1065°C (2 wt.% H_2O), which has an SEE of ±29°C, assuming a pressure of 5 kbar. The temperatures are ~16°C lower when calculated using a pressure of 2 kbar. The clinopyroxene-liquid and olivine-liquid temperature estimates have slight overlap (Fig. 14). However, the crystal populations are small (two crystals each of clinopyroxene and olivine).

The clinopyroxene-liquid and clinopyroxene geobarometers yield slightly conflicting results (Fig. 15), but a new calibration of the clinopyroxene-liquid barometer (Neave and Putirka, 2017) resolves this conflict. The clinopyroxene-liquid barometer (Putirka, 2008) yields 9.6 – 10.6 kbar (±3.6 kbar) with 1 wt.% H_2O and 10.3 – 11.4 kbar (±3.6 kbar) with 2 wt.% H_2O. Two barometers based on clinopyroxene composition alone (Putirka, 2008; Eqns. 32a and 32b) yield comparable results (Table 9) but differ from the clinopyroxene-liquid barometer. Equation 32a does not require an H_2O content estimate and yield -0.1 – 2.6 kbar (±3.1 kbar). Equation 32b, which requires an estimation of H_2O content and has no systematic error as in Equation 32a, yields 0.5 – 1.5 kbar (0.5 wt.% H_2O), 0.7 – 1.7 kbar (1 wt.% H_2O), and 1.2 – 2.2 kbar (2 wt.% H_2O), all with ±2.5 kbar error. The Neave and Putirka (2017) clinopyroxene-liquid barometer yields results of 0.09-0.15 kbar (0 wt.% H_2O), 0.04 – 0.10 (0.5 wt.% H_2O), 0 – 0.06 (1 wt.% H_2O), and -0.08 – -0.03 kbar (2 wt.% H_2O), all with ±1.4 kbar error. If the older calibration of clinopyroxene-liquid barometer is used, the pressure results for the basaltic andesite are not resolved enough to be meaningful. However, the new calibration of Neave and Putirka (2017) restricts the basaltic andesite pre-eruptive pressure to the shallow crust, consistent with the clinopyroxene barometer.

Basaltic andesite pre-eruptive temperature and pressure summary

The pre-eruptive temperature of the basaltic andesite is 1065 – 1169°C (+45°C and -29°C error) based on both olivine-liquid and clinopyroxene-liquid thermometers. Clinopyroxene-liquid thermometer may be showing higher temperatures than the olivines because either clinopyroxene or olivine may be antecrystic. Another possibility is that the barometer used in conjunction with this thermometer was not appropriate for this system.

The pressure estimates for the basaltic andesite are constrainable to the shallower crust using the mineral-liquid and mineral barometers. The clinopyroxene-liquid barometer of Putirka (2008) estimated deep crustal pressures (9.6-14.2 kbar) whereas the two clinopyroxene barometers and new clinopyroxene-liquid

barometer estimated shallow crustal pressures (-0.1-3.7 kbar and -0.08 to 0.15 kbar, respectively). These shallower estimates are similar to the estimated depth of the present magma reservoir beneath Fisher Caldera (Gong et al., 2015). The negative pressure results are not necessarily wrong especially since the other pressure estimates are very low pressures. The 1 atm experiments in these calibrations yield 1 atm as an average pressure, but with an error of ±1-3 kbar. Since 1 atm is equivalent to 0.001 kbar, or 0 kbar in rounding, it is natural that the models will fall to one or the other side of 0 kbar. Thus, these small negative values in pressure estimates are not inconsistent because the positive pressure estimates are very low as well.

Table 9. Temperatures and pressures calculated using the clinopyroxene-liquid thermobarometer of Putirka (2008), clinopyroxene barometer of Putirka (2008), and clinopyroxene-liquid barometer of Neave and Putirka (2017). The standard error of estimate (SEE) for the thermometer is ±45°C and ±3.6 kbar for the Eqn 30 barometer. The two other pressure estimates are based on a geobarometer that only takes into account clinopyroxene composition (Eqns 32a & 32b). Eqn 32a (±3.1 kbar) does not need an H_2O estimate whereas Eqn 32b (±2.5 kbar) does need an estimation of H_2O content. The Neave and Putirka (2017) barometer has an SEE of ±1.4 kbar. Analyses in bold are the clinopyroxene-liquid pairs that are closest to equilibrium.
Under "Location", "dark" and "bright" refer to the BSE-brightness of the sector analyzed.
Mg# = $Mg^{2+}/(Mg^{2+} + Fe^{2+})*100$

Deposit type	Sample	Input H_2O (wt.%)	Cpx Analysis ID	Glass Analysis ID	Location	cpx Mg#	Wo	En	Fs	Temp °C	Eqn 30 Pressure (kbar)	Eqn 32a Pressure (kbar)	Eqn 32b Pressure (kbar)	Neave and Putirka (2017) Pressure (kbar)
Shishaldin-type	97S-PS-34B	0.5	34b_px3	34b_g12	dark rim	76.9	41.1	45.3	13.6	1135	9.2	1.2	0.9	-
		0.5	**34b_px4**	**34b_g12**	**dark core**	**79.1**	**42.4**	**45.6**	**12.1**	**1139**	**10.3**	**0.6**	**1.1**	**0.10**
		0.5	34b_px5	34b_g12	dark rim	75.9	39.9	45.6	14.5	1144	9.6	2.6	1.5	-
		0.5	**34b_px6**	**34b_g12**	**dark core**	**80.7**	**43.0**	**46.0**	**11.0**	**1138**	**10.2**	**-0.1**	**0.5**	**0.04**
		0.5	34b_px7	34b_g12	bright rim	75.9	45.4	41.4	13.2	1169	12.8	5.9	3.0	-
		0.5	34b_px8	34b_g12	bright core	79.8	45.5	43.5	11.0	1167	13.1	4.0	2.9	-
		1	34b_px3	34b_g12	dark rim	76.9	41.1	45.3	13.6	1128	9.6	1.2	1.1	-
		1	**34b_px4**	**34b_g12**	**dark core**	**79.1**	**42.4**	**45.6**	**12.1**	**1132**	**10.6**	**0.6**	**1.3**	**0.06**
		1	34b_px5	34b_g12	dark rim	75.9	39.9	45.6	14.5	1137	10.0	2.6	1.7	-
		1	**34b_px6**	**34b_g12**	**dark core**	**80.7**	**43.0**	**46.0**	**11.0**	**1131**	**10.6**	**-0.1**	**0.7**	**0.00**
		1	34b_px7	34b_g12	bright rim	75.9	45.4	41.4	13.2	1162	13.2	5.9	3.2	-
		1	34b_px8	34b_g12	bright core	79.8	45.5	43.5	11.0	1159	13.5	4.0	3.1	-
		2	34b_px3	34b_g12	dark rim	76.9	41.1	45.3	13.6	1114	10.3	1.2	1.6	-
		2	**34b_px4**	**34b_g12**	**dark core**	**79.1**	**42.4**	**45.6**	**12.1**	**1118**	**11.4**	**0.6**	**1.7**	**-0.03**
		2	34b_px5	34b_g12	dark rim	75.9	39.9	45.6	14.5	1123	10.7	2.6	2.2	-
		2	**34b_px6**	**34b_g12**	**dark core**	**80.7**	**43.0**	**46.0**	**11.0**	**1118**	**11.3**	**-0.1**	**1.2**	**-0.08**
		2	34b_px7	34b_g12	bright rim	75.9	45.4	41.4	13.2	1147	13.9	5.9	3.7	-
		2	34b_px8	34b_g12	bright core	79.8	45.5	43.5	11.0	1145	14.2	4.0	3.6	-

Table 10. Temperatures calculated using the olivine-liquid thermometer of Putirka (2008) using Eqn 22 and Beattie (1993). All olivines are included, but only two analyses meet the equilibrium requirement. The accepted Kd(Fe-Mg) is 0.30 ± 0.03 for equilibrium. The pressure for the calculations was set to 0.5 GPa and 0.2 GPa. However, the temperature changes little with the range of pressures suitable for the basaltic andesite. For Equation 22, 1 wt% H_2O was used.
The standard error of estimate (SEE) for the thermometer using Eqn 22 is ±29°C and ±44°C for Beattie (1993).
Mg# = molar MgO/(MgO+FeO)*100

								Temp °C (Eqn 22)		Temp °C (Beattie, 1993)	
Deposit type	Sample	Olv Analysis ID	Glass Analysis ID	Kd (Fe-Mg)	olv Mg#	glass Mg#	Fo	P = 0.5 GPa	P = 0.2 GPa	P = 0.5 GPa	P = 0.2 GPa
Shishaldin-type	97S-PS-34b	34b_olv1	5B_g6	0.26	71.4	37	71.0	1081	1065	1102	1087
		34b_olv2	5B_g6	0.27	71.0	37	70.7	1081	1065	1102	1087
		34b_olv3	5B_g6	0.27	71.3	37	70.9	1082	1065	1102	1087
		34b_olv4	5B_g6	0.26	71.7	37	71.3	1080	1064	1102	1087
		34b_olv5	5B_g6	0.26	72.0	37	71.7	1079	1063	1102	1087
		34b_olv6	5B_g6	0.26	71.9	37	71.6	1079	1063	1102	1087
	15S-PS-5b	5B_olv1	5B_g6	0.24	73.1	37	72.8	1072	1056	1102	1087
		5B_olv2	5B_g6	0.26	72.0	37	71.7	1079	1063	1102	1087

4.3 Pre-eruptive water content

The pre-eruptive water content estimate is necessary to model fractional crystallization. The water content of the rhyodacite was determined by plagioclase-liquid equilibrium using the methods of Waters and Lange

(2015). The plagioclase hygrometer calculation is dependent on temperature, which ideally is independently determined. In Fig. 16, each grey curve represents a single plagioclase-liquid pair. Thermometry results (section 4.2) are plotted over these curves to show the most likely water content ranges for the magmas. The two-oxide thermometer pairs with the closest estimate for equilibrium [based on the Bacon and Hirschmann (1988) test] for each deposit type were used for the hygrometer calculations. S-type deposits (888°C), returned pre-eruptive water contents between 3.8 and 4.8 wt.% H_2O (±0.35), with an average of 4.2 wt.% H_2O and a standard deviation of 0.2 (n = 77). F-type deposits (908°C) returned pre-eruptive water contents between 3.7 – 4.1 wt.% H_2O, with an average of 3.8 wt.% H_2O and a standard deviation of 0.1 (n = 34). These results overlap the S-type analyses, which is expected due to the similarity in compositions between the two deposits. Accounting for the errors of the two-oxide thermometer and the plagioclase hygrometer (Fig. 16a), the full possible range for the pre-eruptive water content of the rhyodacite is ~2.5 to 6 wt.% H_2O.

In thermometry and hygrometry calculations for the basaltic andesite, there is a circular dependence between water content and temperature. To address this issue, pre-eruptive temperature was estimated using a range of possible water contents. The thermometry results were overlain on the H_2O-temperature curves to estimate the most likely H_2O content for the basaltic andesite (Fig. 16b-c). Areas of overlap between thermometry and H_2O curves represent the possible range of water contents for the basaltic andesite magma. The clinopyroxene-liquid (Fig. 16b) and olivine-liquid (Fig. 16c) thermometry results yield <~1.5 wt.% H_2O and ~0.5 – ~2.5 wt.% H_2O, respectively (±0.35 wt.% H_2O). This is consistent with water content measurements obtained from melt inclusions in other mafic Shishaldin magmas, which are ≤2.43 wt.% H_2O (Plank et al., 2013; Zimmer, 2008; Zimmer et al., 2010).

Pre-eruptive water content summary

The pre-eruptive water content of the rhyodacite is ~4 wt.% H_2O (±1.5 wt.% H_2O) and of the basaltic andesite is 0.5 – 2 wt.% H_2O. There is no significant difference between the S-type and F-type deposits for any composition. Although these results have a broad range, it can be said that the basaltic andesite is drier than the rhyodacite. These water content estimates provide a basis for the water content in the MELTS models. The water content of the basaltic andesite gives a starting water content for the MELTS models and the water content of the rhyodacite is the target for the MELTS modeling.

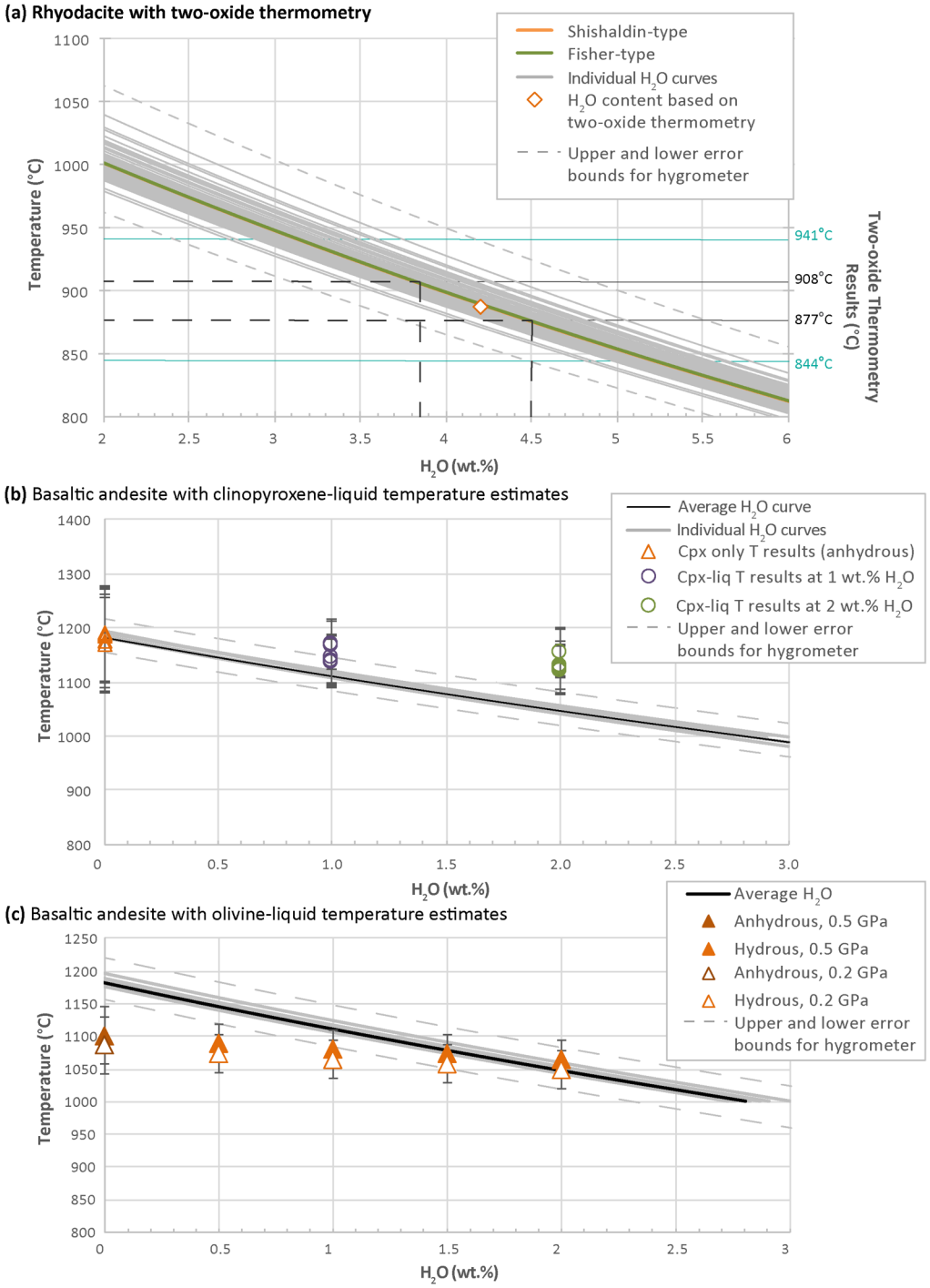

Figure 16. Plagioclase-liquid hygrometer results with error bars (dashed grey lines) for the **(a)** rhyodacite (n = 111) and **(b-c)** basaltic andesite (n = 7). **(a)** Bold temperature lines represent minimum and maximum pre-eruptive temperature from two-oxide thermometry and lighter shade lines are the associated average absolute deviation of the thermometer. Note the average S-type curve plots directly under the F-type curve, and is not visible. **(b-c)**. Grey curves are individual plagioclase-liquid pair calculations of H_2O.

4.4 Oxygen isotope chemistry

Oxygen isotope values for the co-erupted magmas will help establish the type of magmatic plumbing system, and for the S-type deposits determine if they are from Fisher or Shishaldin. Shishaldin has a normal $\delta^{18}O$ signature whereas the Fisher CFE has a low $\delta^{18}O$ signature. An original objective was to also gain oxygen isotope thermometry from mineral pairs in both magmas because it would be an independent estimate of temperature, which does not rely on pressure or water content. Most mineral pairs are out of equilibrium in this study by being outside of the temperature fractionation lines in Fig. 17, thus temperature estimates were not possible. However, oxygen isotopic disequilibrium provides important information about the assimilation processes of magmas. The oxygen isotope results of this study are consistent with the Fisher CFE results of Bindeman et al. (2001; Fig. 18), who analyzed deposits similar to the F-type in this study from Unimak Island and what may have been S-type deposits from Cold Bay, which is on the Alaskan Peninsula ~115 km east of Fisher Caldera, due to the presence of a discrete scoria layer. The Cold Bay deposit analyzed by Bindeman et al. (2001) is far from the source, so this study analyzed S-type deposits from Unimak Island. Bindeman et al. (2001) indicated that the low $\delta^{18}O$ signature of the Fisher CFE deposits is a unique characteristic and can be used to identify the deposit. Thus, $\delta^{18}O$ values can be used to determine if the S-type deposit also has the same signature. If they do, then it is less likely that the S-type and F-type deposits are from separate eruptions or separate volcanic centers. Oxygen isotope values for plagioclase, orthopyroxene, clinopyroxene, and Fe-Ti oxides in seven samples from five field sites were measured (Table 11) in order to show if there are any differences between the F-type and S-type deposits. Two locations are of the S-type deposits and three locations are from the F-type deposits. Typical magmatic $\delta^{18}O$ compositions from the mantle are 5.5‰ or greater (Eiler et al., 2000; Bindeman et al., 2001), and all analyzed S- and F-type samples are isotopically lighter (i.e., have $\delta^{18}O$ signatures <5.5‰) than typical magmas.

Oxygen isotope analyses of both S-type and F-type deposits show wide range of values with greater variability in rhyodacite analyses (Table 11; Fig. 17, 18a). The widest variability is in rhyodacite bulk and single crystal plagioclase $\delta^{18}O$ values (S-type: +4.54 to +4.98‰, F-type: +4.40 to +4.63‰; ±0.08-0.12‰). Analyses of single plagioclase crystals show heterogeneity in the oxygen isotope values (Table 11) +4.62‰, +4.98‰,

+4.90‰, and +4.54‰ for the S-type rhyodacite. In the rhyodacite, clinopyroxene (S-type: +3.42 to +4.39‰, F-type: +3.98‰ & +4.39‰, Fig. 17b, 18d) is generally isotopically heavier than expected if it was in equilibrium with plagioclase. A single clinopyroxene analysis is in equilibrium with plagioclase of ~4.4-4.6‰, but it is an outlier from the other three bulk-crystal analyses. The outlier crystal was physically larger and more equant than clinopyroxene bulk crystals, perhaps representing two populations, one of which may be antecrystic. Fe-Ti oxides typically contain lower oxygen isotope values than plagioclase or pyroxenes according to fractionation curves. Ulvöspinel (S-type: 2.13 to 2.91‰, F-type: 2.96‰ & 3.35‰; Fig. 17c-e, 18b) is in most cases isotopically heavier than predicted for equilibrium with clinopyroxene, orthopyroxene, or plagioclase.

Basaltic andesite plagioclase $\delta^{18}O$ values are isotopically heavier than expected if these crystals were in equilibrium with the analyzed orthopyroxene (S-type: +4.14 to +4.67‰, F-type: +4.14‰ to +4.59‰; Fig. 17a, 18c). Orthopyroxene crystals from basaltic andesite samples were analyzed for oxygen isotope compositions due to their abundance and size relative to olivine and clinopyroxene. However, later investigation revealed that all orthopyroxenes observed in the basaltic andesite were encased in a selvedge of rhyodacite glass, suggesting these crystals do not reflect basaltic andesite compositions because the orthopyroxenes are not phenocrysts of the basltic andesite. Thus, the basaltic andesite orthopyroxenes values (+3.41 to +3.69‰), are interpreted to represent the orthopyroxene oxygen isotope values of a rhyodacite. These minerals are isotopically lighter than those in the rhyodacite (+4.14 to +4.67‰; Fig. 17c) with 2σ error (see discussion on possible reasons in section 5.2).

The plagioclase crystals from the S-type basaltic andesite (+4.58 to +4.86‰) span the same range of $\delta^{18}O$ values as the plagioclase crystals from the S-type rhyodacite and as the basaltic andesite analyzed by Bindeman et al. (2001), within 2σ error. Two populations of plagioclase exist within the basaltic andesite: (1) large plagioclase surrounded by silicic selvedge and (2) smaller, thinner phenocrystic plagioclase. Larger crystals are more common and were preferentially chosen to obtain the necessary mass for laser fluorination. Thus, the xenocrystic, rhyodacite-derived plagioclase crystals were unintentionally preferred for isotopic analyses due to their relative greater abundance and size. As a result, the $\delta^{18}O$ signature of the basaltic

andesite crystals are not well characterized. Fortunately, Bindeman et al. (2001) did analyze an olivine crystal, which is a known phenocryst of the basaltic andesite, and this crystal has a low $\delta^{18}O$ signature of 3.98‰.

Table 11. Oxygen isotope composition of phenocrysts in Shishaldin-type and Fisher-type deposits.
RD = rhyodacite; BA = basaltic andesite
*Single crystal analysis, otherwise analyses represent a group of crystals (bulk analysis).
^Glass chemistry of similar deposit due to lack of glass chemistry for 15S-PS-4a.

			$\delta^{18}O$, (‰)			
Sample	**Deposit Type**	**SiO_2 (wt%) glass**	**Plag**	**Opx**	**Cpx**	**Ulv**
97S-PS-34a	Shishaldin-type RD	68.27	4.62*	4.29	3.42*	2.81
			5.36		4.27	2.50
			4.45			
			4.73			
FC-175d	Shishaldin-type RD	68.44	4.98*	4.14	4.39	2.91
			4.78			
15S-PS-2d	Shishaldin-type RD	68.94	4.90*	4.67	4.32	2.60
			4.54*			2.13
			4.55			
FC-183	Fisher-type RD	66.19	4.40	4.39*	3.98	3.35
			4.45	4.59		
15S-PS-4a	Fisher-type RD	68.99^	4.42	4.14	4.39	2.96
			4.63			
97S-PS-34b	Shishaldin-type BA	53.94	4.64	3.41*		
			4.86	3.61		
			4.64			
15S-PS-2c	Shishaldin-type BA	56.7	4.66	3.69		
			4.71			
			4.58			

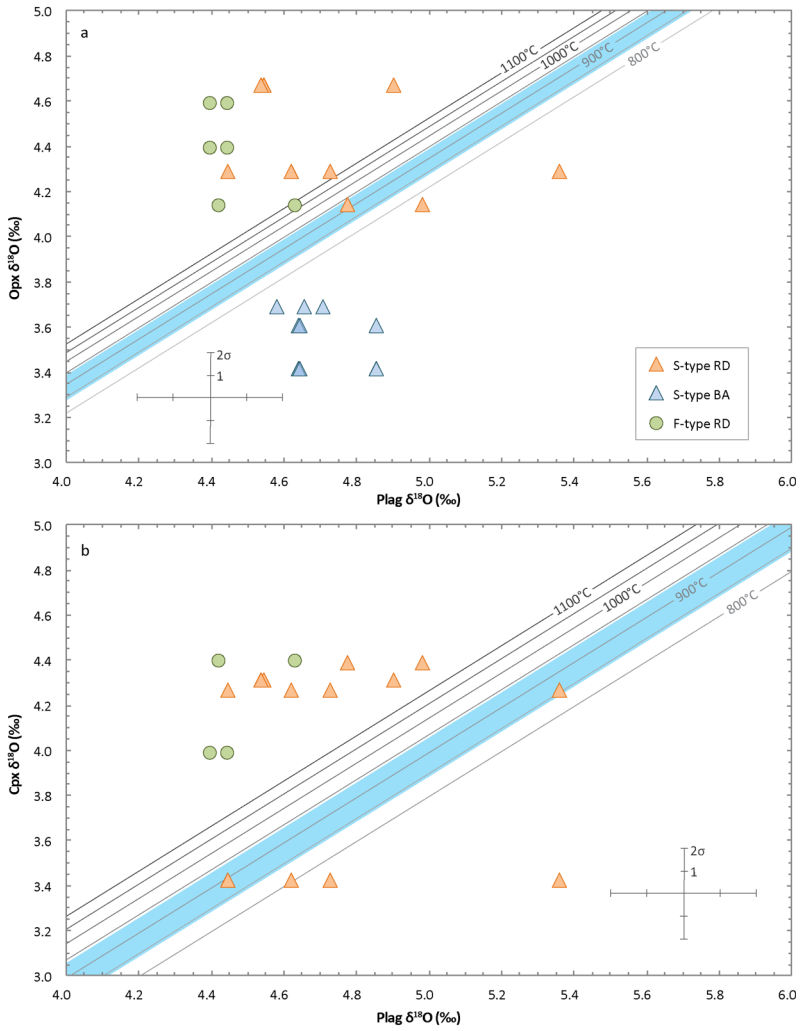

Figure 17. $\delta^{18}O$ (Plagioclase) vs. $\delta^{18}O$ (Opx, Cpx). Error bars of 2σ = ~0.2‰. The temperature fractionation lines represent equilibrium between the respective minerals. Outside of those lines, the minerals are out of equilibrium. Blue shaded region represents the pre-eruptive temperature range from two-oxide thermometry calculations of 844-941°C. **(a)** $\delta^{18}O$ (Plagioclase) vs. $\delta^{18}O$ (Opx), Temperature lines are based on An_{40}-Opx fractionation from Chiba et al. (1989). **(b)** $\delta^{18}O$ (Plagioclase) vs. $\delta^{18}O$ (Cpx). Temperatures are based on An_{40}-Cpx fractionation from Chiba et al. (1989). Abbreviations: RD = rhyodacite, BA = basaltic andesite, T = temperature.

Next Page: $\delta^{18}O$ (Plag, Cpx, Opx) vs. $\delta^{18}O$ (Mt). Error bars of 2σ = ~0.2‰. **(c)** $\delta^{18}O$ (Plag) vs. $\delta^{18}O$ (Mt). Temperatures are based on An_{40}-Mt fractionation from Chiba et al. (1989). **(d)** $\delta^{18}O$ (Cpx) vs. $\delta^{18}O$ (Mt). Temperatures are based on Cpx-Mt fractionation from Chiba et al. (1989). **(e)** $\delta^{18}O$ (Opx) vs. $\delta^{18}O$ (Mt). Temperatures are based on Opx-Mt fractionation from Chiba et al. (1989). Abbreviations: RD = rhyodacite, BA = basaltic andesite, T = temperature.

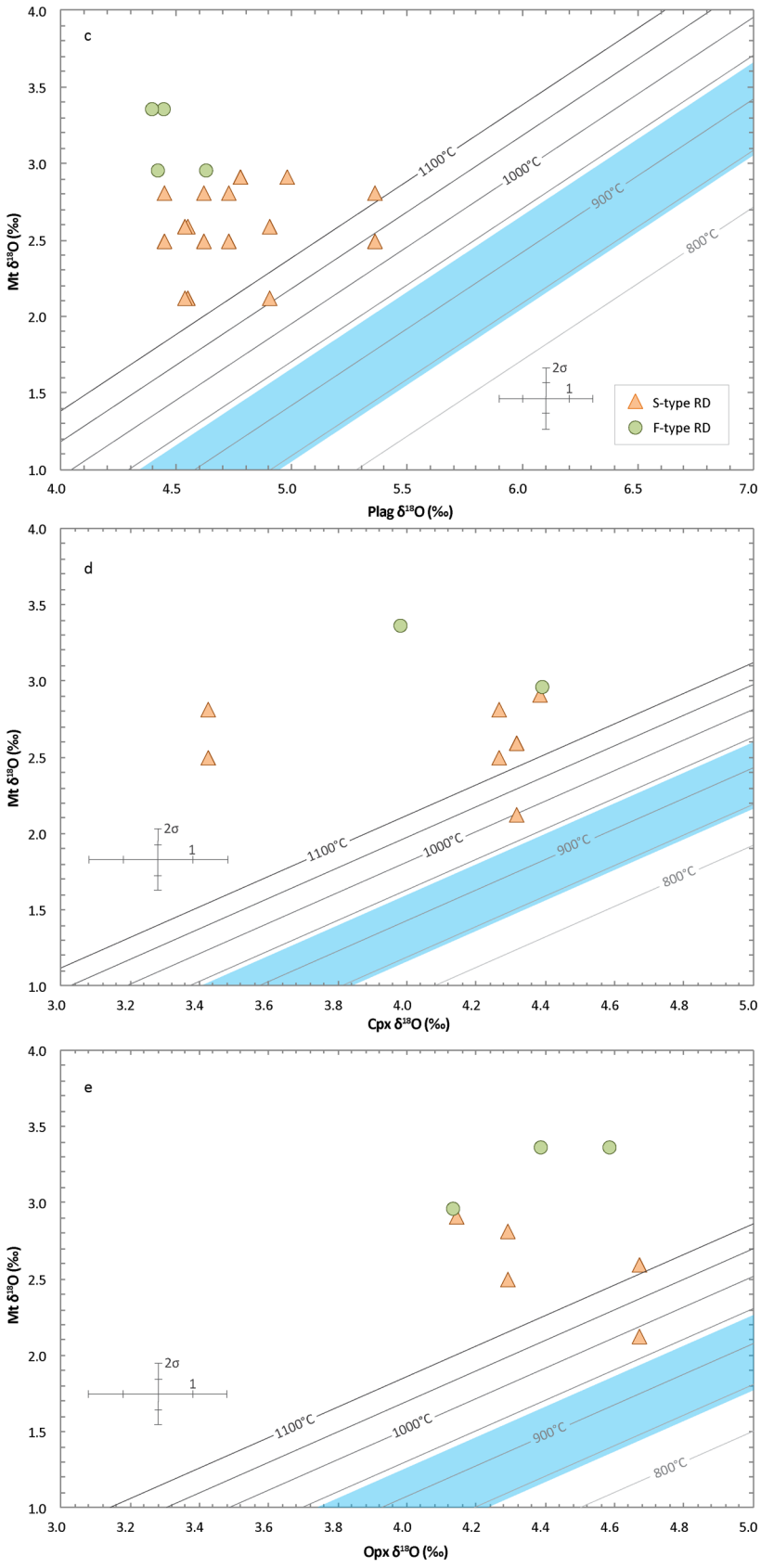

Figure 17 (*continued*).

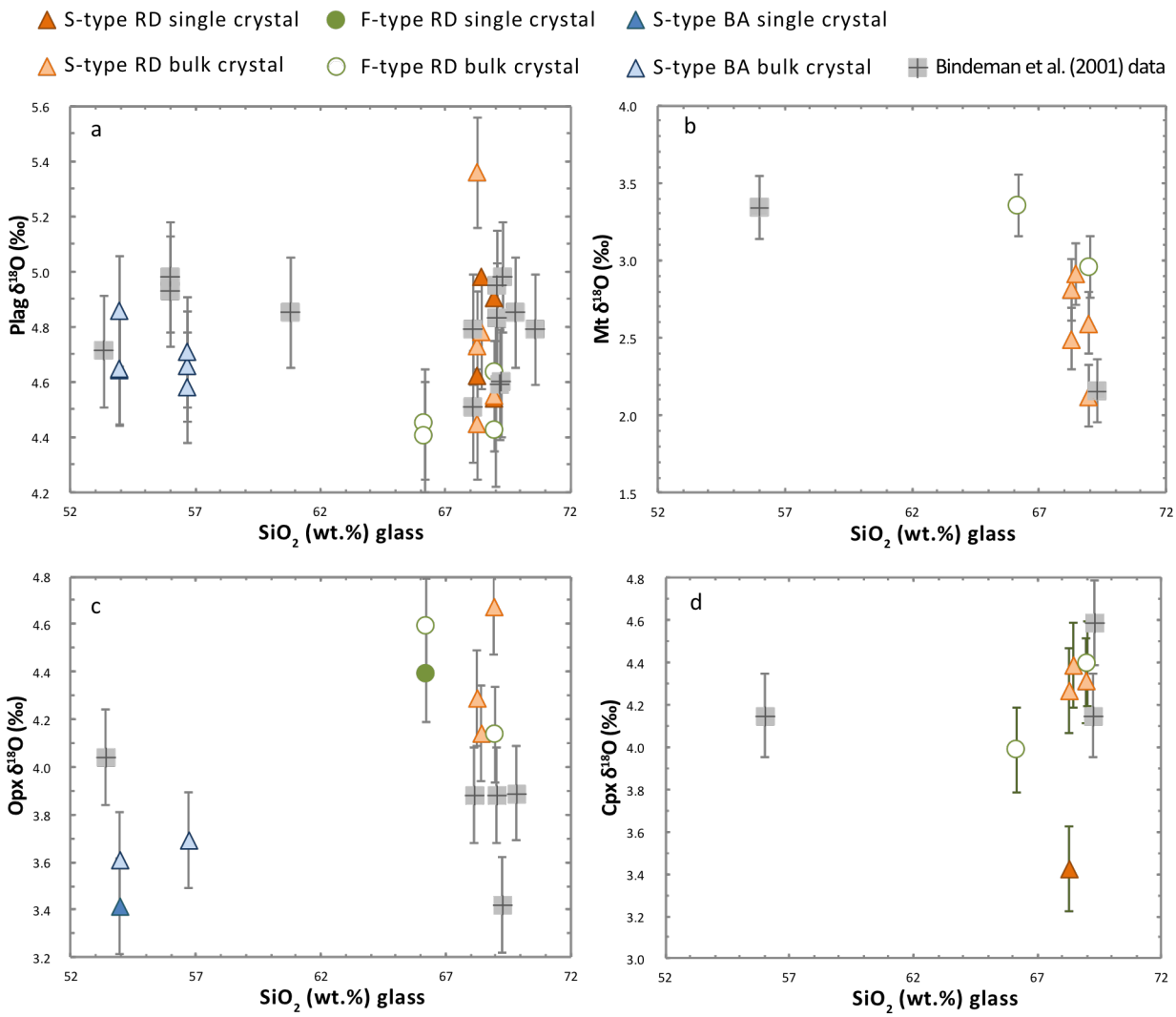

Figure 18. ***Oxygen isotope results.*** Darker-toned data points are single crystal analyses while the light-toned points represent an analysis of multiple crystals. In both (a) and (c) the orthopyroxene and plagioclase crystals represented by the mafic glass chemistry are not crystals that are from the basaltic andesite, but from a silicic melt, which may be the co-erupted rhyodacite. Error bars represent 2 sigma errors of ~0.2‰.

4.5 Relationship between the rhyodacite and basaltic andesite

Establishing whether fractional crystallization of the basaltic andesite is the dominant process that led to the formation of the rhyodacite is important in considering hypothesis #1 of the possible magmatic plumbing systems. Least squares and simple subtraction calculations were used to model relationships of major element compositions of the rhyodacite to the basaltic andesite. The threshold for acceptable least squares residuals was set at 0.1, with 0.05 preferred. Models of fractional crystallization of the basaltic andesite using observed minerals (clinopyroxene, plagioclase, and ulvöspinel) required 58% crystallization and yielded residuals of 0.31, well above the maximum threshold. This calculation subtracts ~19% clinopyroxene, 31% plagioclase, and 9% ulvöspinel, which are reasonable proportions based on observed mineral abundances in the rhyodacite. However, orthopyroxene, an important mineral in the rhyodacite, is missing from this model, which either means orthopyroxene was not fractionated or this model does not represent the magmatic system. Simple subtraction calculations of fractional crystallization of the basaltic andesite to generate the rhyodacite compositions were similarly unsuccessful (Fig. 19) and a direct genetic relationship between the co-erupted basaltic andesite and rhyodacite were not possible. The oxides K_2O, Al_2O_3, and TiO_2 versus MgO in Fig. 19 are the most difficult to see a fractional crystallization relationship. These results are consistent with the least squares calculations and simple subtraction fractional crystallization results of Stelling (2003).

4.6 MELTS modeling

In order to completely rule out a fractional crystallization relationship between the basaltic andesite and the rhyodacite magmas, MELTS modeling was also used. MELTS software estimates liquid and mineral compositions during the process of fractional crystallization using phase equilibria and thermodynamic properties rather than input mineral chemistries and abundances, and represents a more rigorous test of a fractional crystallization than least squares calculations or simple subtraction fractional crystallization modeling. Specifically, the major element composition of the basaltic andesite matrix glass was theoretically cooled and fractionated to match the composition of rhyodacite matrix glass under a variety of environmental conditions (Fig. 20). MELTS models require ~60 – 70% fractional crystallization to reach the rhyodacite composition from the starting basaltic andesite composition (Table 16).

Table 12. Mass balance fractionation model compositions and amount fractionated for each stage. Stelling (2003) model uses the same amount fractionated but uses the mineral chemistries from this study.

Model	Stage 1 composition	Stage 1 fractionated	Stage 2 composition	Stage 2 fractionated
Stelling (2003)	60% plag, 20% cpx, 10% olv, 10% mt (BA)	10%	60% plag, 20% cpx, 10% olv, 10% mt (BA)	10%
Model 1	100% plag (BA)	4%	69% plag, 31% cpx (BA)	45%
Model 2	100% plag (BA)	4%	69% plag, 31% cpx (BA)	40%
Model 3	100% plag (BA)	5%	35% plag, 35% cpx, 30% ulv (BA)	40%

Model	Stage 3 composition	Stage 3 fractionated	Stage 4 composition	Stage 4 fractionated
Stelling (2003)	60% plag, 20% cpx, 10% olv, 10% mt (BA)	10%	60% plag, 20% cpx, 10% olv, 10% mt (BA)	10%
Model 1	40.3% opx, 56.7% ulv, 3% ap (RD)	20%	40% plag, 10% ilm, 40% ap (RD)	1%
Model 2	35% plag, 35% cpx, 30% ulv (BA)	10%	35% opx, 60% ulv, 5% ap (RD)	15%
Model 3	50% plag, 40% opx, 9% cpx, 1% ulv (RD)	1%	35% opx, 60% ulv, 5% ap (RD)	1%

Model	Stage 5 composition	Stage 5 fractionated	Stage 6	Total fractionated
Stelling (2003)	60% plag, 20% cpx, 10% olv, 10% mt (BA)	10%	Repeat previous stage	60%
Model 1	-	-	-	70%
Model 2	-	-	-	69%
Model 3	60% plag, 40% ap (RD)	2%	-	49%

Table 13. MELTS model parameters and results.
fO_2, pressure, and starting H_2O are inputs for the models. Any models with a final temperature >833°C ended with a quadratic minimization error.

fO_2 buffer	Pressure (kbar)	Starting H_2O (wt.%)	Liquidus Temperature (°C)	Melt Fraction remaining (F)	Total Fractionated	H_2O (wt.%) at end	Final temperature (°C)	First mineral(s) to crystallize	OPX present?	Ulv-Ilm present simultaneously?	OLV present?
QFM	0.5	2	1078	0.31	0.69	2.9	832	Ulv (Ulv 40)	YES; 1024 - 830°C; Wo 3.8-2.2 En 65-43 Fs 31-55	NO; Ulv 1078-832°C; No Ilm	YES; 1060-1027°C; Fo66-61
QFM	2	2	1082	0.34	0.66	5.8	833	Ulv	NO	NO; Ulv 1082-833°C; No Ilm	NO
QFM+1	2	0.5	1156	0.26	0.74	1.9	831	Plag (An69)	YES; 1041-876°C	YES; 996 - 830°C	NO
QFM	2	0.5	1153	0.24	0.76	2.1	833	Plag (An69)	NO	NO; Ulv 1103-843°C; Ilm 838-833°C	NO
QFM-1	2	0.5	1150	0.22	0.78	2.3	840	Plag (An68)	NO	NO; Ulv 1085-980°C; Ilm 935-840°C	YES; 975-900°C; Fo12-4
QFM-2	2	0.5	1148	0.24	0.76	2.0	908	Plag (An68)	NO	NO; Ulv 1068-963°C; Ilm 1078-1073, 958-908°C	YES; 1038-908°C; Fo24-2
QFM	1	0.5	1146	0.24	0.76	2.0	831	Plag (An70)	NO	NO; Ulv 1101-851°C; No Ilm	YES; 846-831°C; Fo17-16
QFM-1	1	2	1070	0.33	0.67	4.4	833	Plag (An77) + Olv (Fo61)	NO	NO; Ulv 1049-833°C; No Ilm	YES; 1070-962°C; Fo61-38
QFM-2	1	2	1076	0.33	0.67	4.4	830	Olv (Fo60)	NO	NO; No Ulv; Ilm 1046-830°C	YES; 1076-869°C; Fo59-13

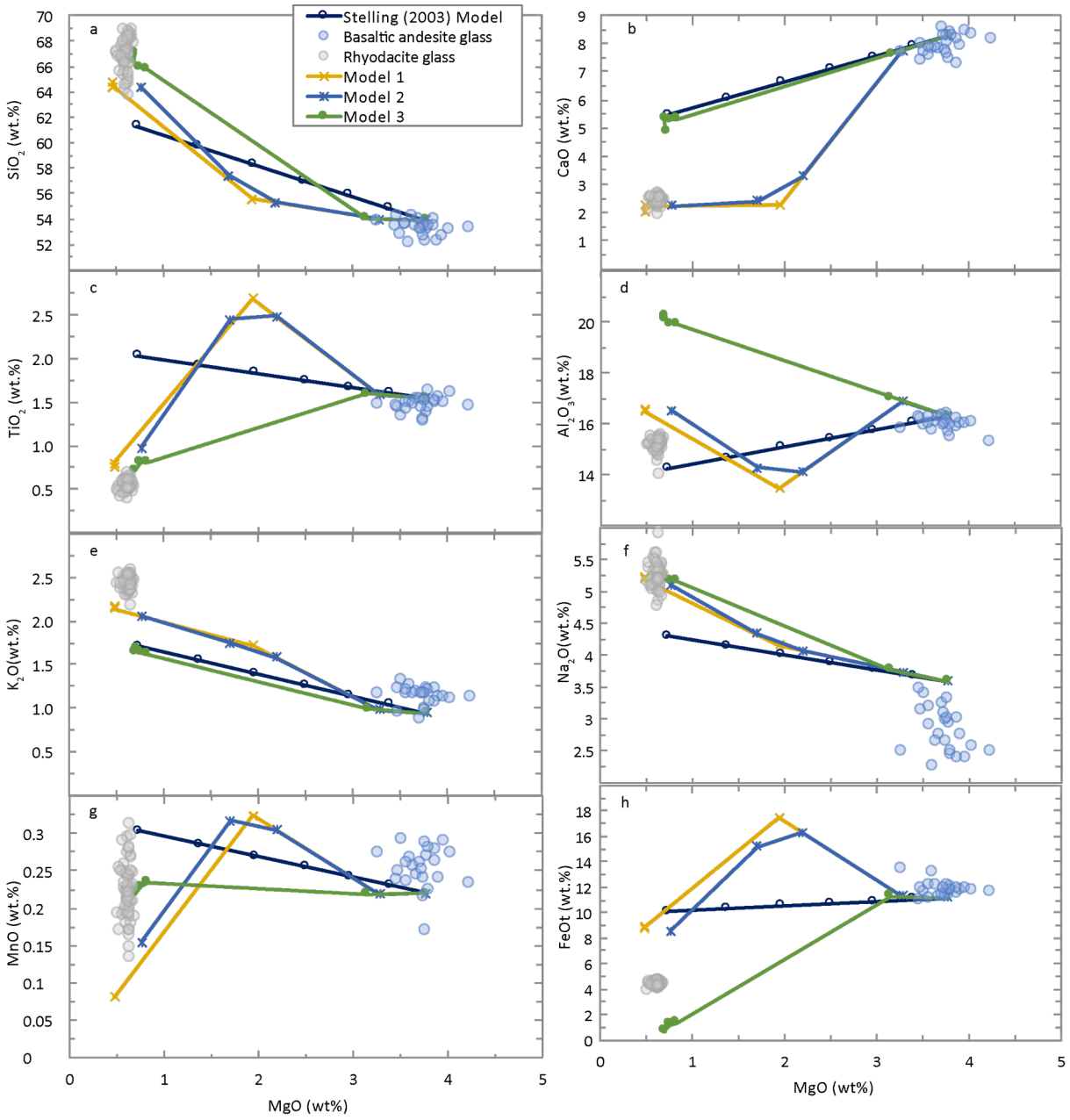

Figure 19. Simple subtraction calculation results of the liquid based on model inputs described in Table 12 where an assemblage of minerals is fractionated at up to six stages. The model labeled Stelling (2003) uses the EPMA data of those minerals obtained in this study but uses the same mineral proportions as Stelling (2003) of 60% plagioclase, 20% clinopyroxene, 10% olivine, and 10% magnetite (ulvöspinel). Models 1, 2, and 3 each start with plagioclase crystallizing, followed by clinopyroxene, ulvöspinel, orthopyroxene, and ilmenite. The differences between these models lies in different proportions of phases and different proportions of mafic phases versus silicic phases (see Table 12 for the phases fractionated in each stage). Models 1 and 2 are best fit models using simple subtraction fractional crystallization.

4.6.1 Liquid line of descent from MELTS modeling

MELTS models produce liquid lines of descent that track the liquid composition through the crystallization process. If the starting and ending magmatic compositions are related through fractional crystallization, the liquid lines of descent should pass through the daughter (rhyodacite) composition. MELTS liquid models (Fig. 20) work well for SiO_2, MgO, TiO_2, and FeOt and do not work well with respect to Na_2O, MnO, Al_2O_3, and P_2O_5 (Fig. 21), which suggests the MELTS models do not show a relationship between the two magmas. Notably, all model runs underestimated Al_2O_3 concentrations by ~4 – 6 wt.%. The most successful runs follow the QFM buffer, consistent with the two-oxide oxygen barometer results (QFM to QFM-1). For K_2O,

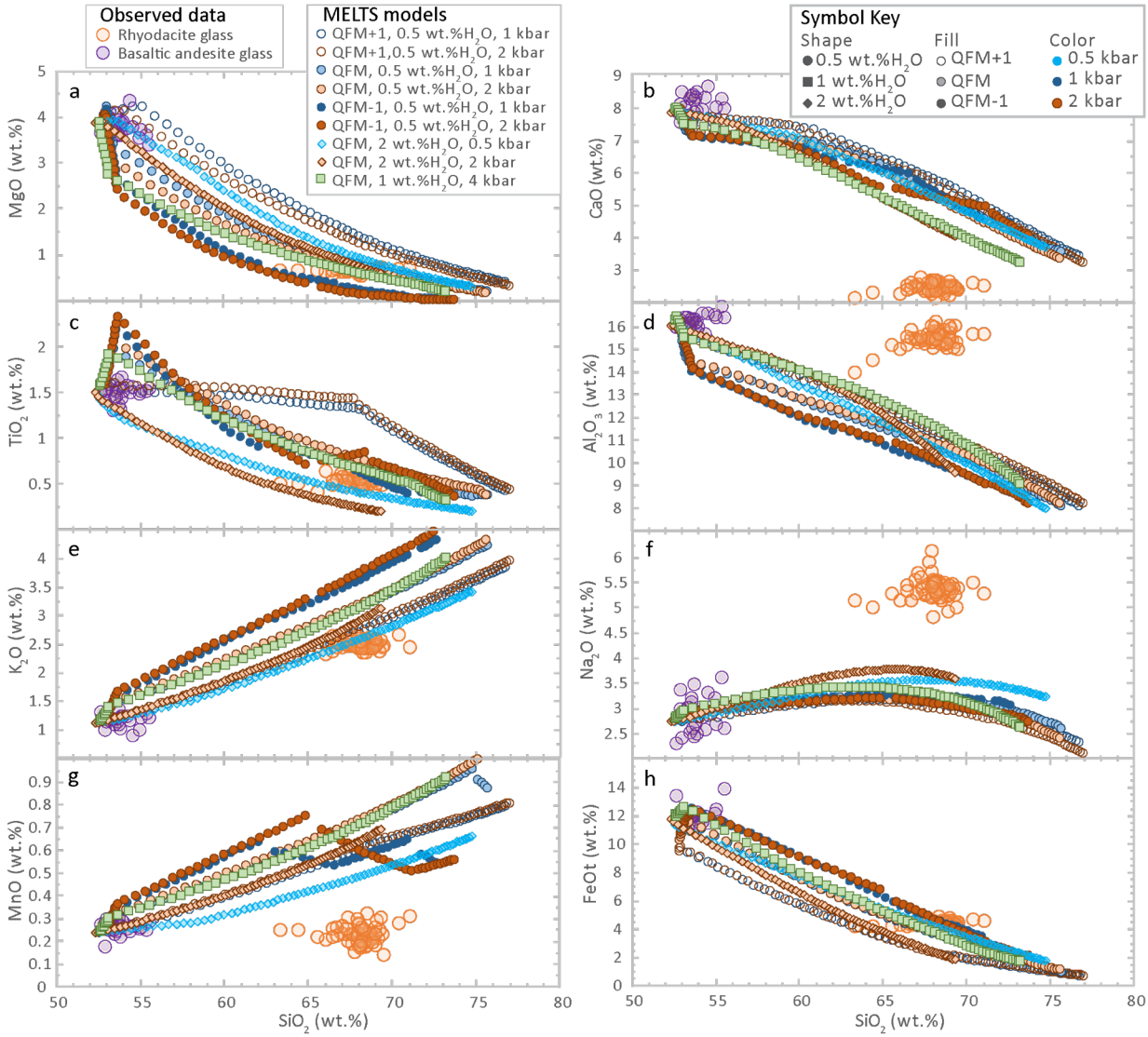

Figure 20. MELTS liquid model results. The models use basaltic andesite glass (large purple circles) as the starting composition. Ideal models will produce compositions similar to the rhyodacite (large orange circles).

QFM models starting with 2 wt.% H_2O at 0.5 kbar and 2 kbar work well. QFM+1 models match the observed K_2O concentrations.

In addition to modeling the liquid line of descent, MELTS can be used to determine the temperature of the occurrence of key mineral phases. Because P_2O_5 is only incorporated by apatite, the concentration of P_2O_5 can track the temperature of first occurrence of apatite during modeled fractionation from the basaltic andesite to the rhyodacite. This can be compared to the apatite saturation geothermometry results to assess the validity of the fractional crystallization modeling results. Figure 21 shows the P_2O_5 concentrations of the liquid changing with changing temperature. The inflection point in P_2O_5 concentration represents apatite saturation and subsequent crystallization. Models that saturate apatite at temperatures above calculated apatite saturation temperatures are considered a failed model. The models that work best with respect to apatite saturation are the ones at QFM, 2 wt.% H_2O, and at 0.5 or 2 kbar. The models show much higher concentration of P_2O_5 than what is observed in the rhyodacite. This may be because the MELTS model does not consider apatite inclusions, which often crystallize due to a local P_2O_5 pile-up surrounding crystallizing minerals (Harrison and Watson, 1984).

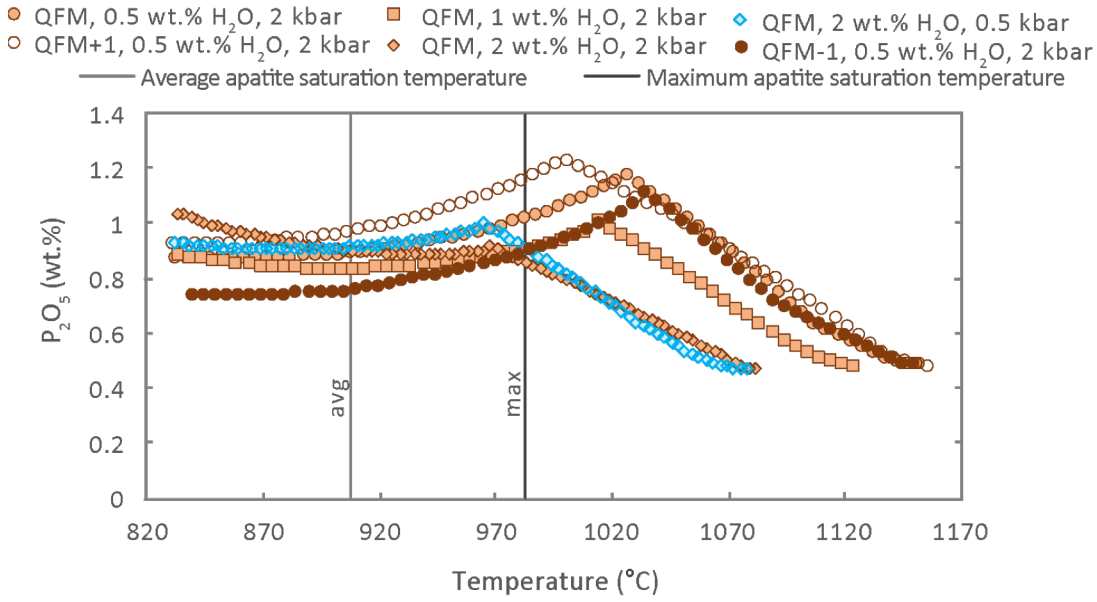

Figure 21. MELTS P_2O_5 versus temperature compared to average and maximum apatite saturation temperature results. Model runs in which saturation (inflection point in P_2O_5 concentration) occurs below the maximum temperature line (determined through apatite saturation geothermometry, error is unknown) are considered best results.

4.6.2 Fractionating minerals

Successful MELTS models should include crystallization and similar compositions of plagioclase, olivine, clinopyroxene and ulvöspinel in the basaltic andesite, and plagioclase, orthopyroxene, ulvöspinel, ilmenite, and apatite in the rhyodacite. Most models produce plagioclase, clinopyroxene, ulvöspinel, and apatite ± orthopyroxene, ±ilmenite, ±olivine. The paragenetic sequence from basaltic andesite to rhyodacite if they are related by fractional crystallization should be either plagioclase or ulvöspinel, olivine or clinopyroxene, orthopyroxene, apatite, and ilmenite. Olivine of the required Fo content is missing in MELTS models and clinopyroxene usually continues late into the crystallization sequence, which is not observed in the rhyodacite. A general crystallization sequence of plagioclase-clinopyroxene-ulvöspinel is seen in most MELTS models. Ulvöspinel is the first phase to crystallize in models starting with higher water content (~2 wt.% H_2O) and following the QFM buffer. Plagioclase compositions changed little and overlapped with the observed data in every run (Fig. 22a). MELTS models reproduce rhyodacite clinopyroxene chemistry when setting the redox conditions to the QFM buffer and starts with 0.5 wt.% H_2O (Fig. 22b). The MELTS models reproduce basaltic andesite clinopyroxene chemistry at redox conditions around QFM+1 when starting with 0.5 wt.% H_2O. Ulvöspinel and ilmenite occur at the same time during a fractionation sequence only when following a QFM+1 fO_2 path, but ulvöspinel and ilmenite do not occur together in QFM models.

Only two sets of starting MELTS conditions allow orthopyroxene to crystallize: 1) low pressures (e.g., 0.5 kbar), high initial water content (~2 wt.% H_2O), and QFM buffer; or 2) higher pressure (2 kbar), low initial water content (~0.5 wt.% H_2O), and QFM+1 buffer. The latter case is unlikely for the rhyodacite because its oxygen fugacity follows the QFM buffer based on two-oxide oxygen barometry results. In the former, ilmenite is absent from the phase assemblage. In both of these cases, modeled clinopyroxene appears late in the crystallization sequence and clinopyroxene chemistry does not match observed mineral compositions. Because the chemistry of the rhyodacite clinopyroxenes is not in equilibrium with the rhyodacite glass, it is unlikely that these clinopyroxenes formed late in the crystallization sequence and probably formed earlier or are unrelated to the rhyodacite.

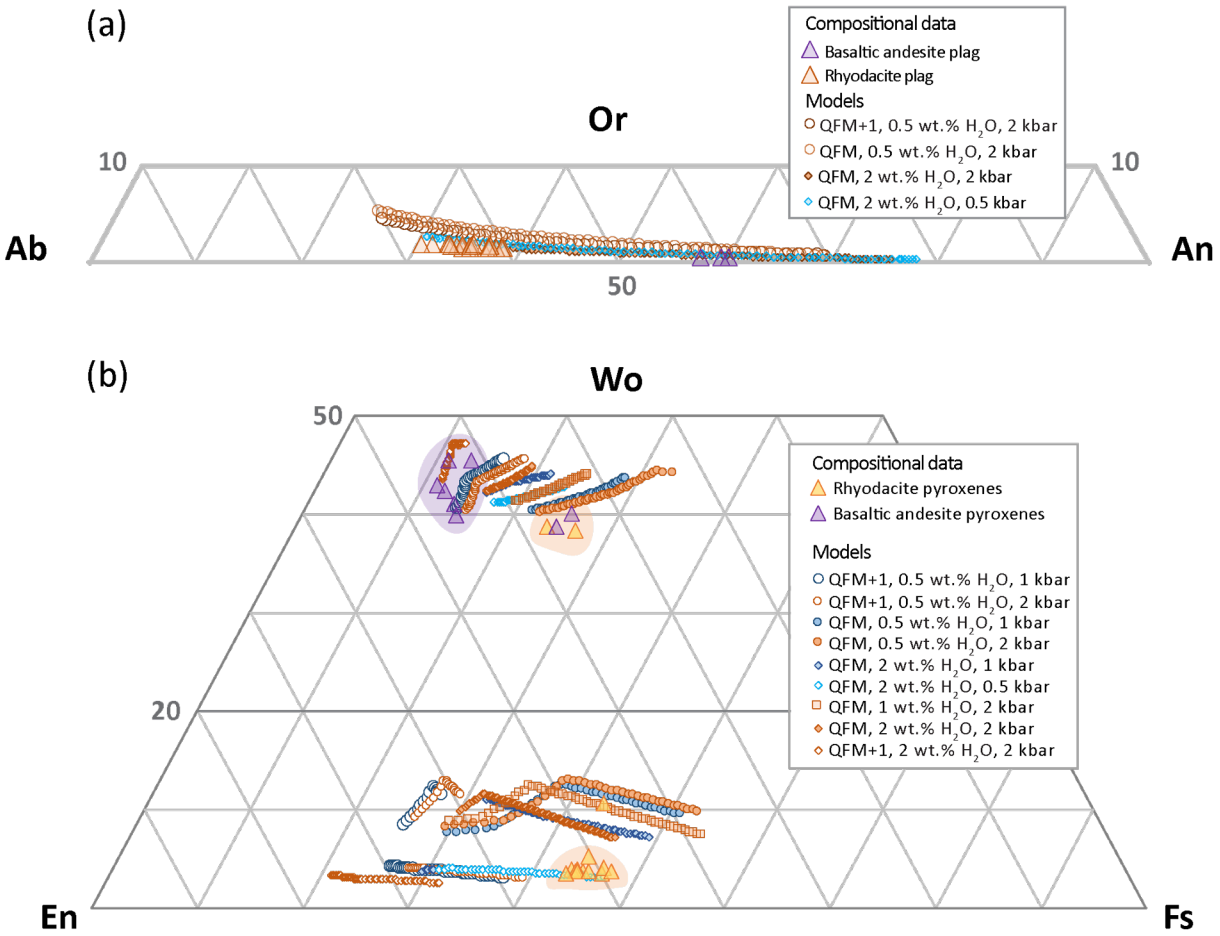

Figure 22. (a) Plagioclase MELTS models results with observed plagioclase compositions. Ab = albite, Or = orthoclase, An = anorthite. **(b)** Clinopyroxene and orthopyroxene MELTS models results with observed pyroxene data. Pyroxene compositions are only shown for when the liquid reaches ~70 wt.% SiO_2. Wo = wollastonite, En = enstatite, Fs = ferrosilite.

4.6.3 Intensive conditions: temperature and H_2O content

Ideally, MELTS should also produce temperature and water content conditions that match the conditions of the rhyodacite and basaltic andesite calculated using mineral equilibria. A few MELTS model runs (QFM buffer, 2 wt.% H_2O, 0.5 or 1 or 2 kbar) have liquidus temperatures consistent with calculated results and reasonably accurate rhyodacite compositions as the liquidus temperatures fall within the temperatures ranges calculated for the basaltic andesite (Fig. 23). However, these models do not accurately predict clinopyroxene compositions or Al_2O_3 glass concentrations. MELTS models that work best to obtain the water content of the rhyodacite are any models with pressures >0.5 kbar when the starting liquid has 2 wt.% H_2O, but since the MELTS modeling does not work then this pressure estimate cannot be trusted (Fig. 24).

4.6.4 Summary of MELTS modeling

Overall MELTS modeling does not support that the rhyodacite formed by fractional crystallization of the co-erupted basaltic andesite. Major element chemistry along the liquid lines of descent, the crystallization sequence, mineral chemistry, and water contents produced by MELTS did not match the observations of the rhyodacite and the basaltic andesite. Matching geothermometry calculations did work well, but that may be because the error bars were rather large for the temperature estimates in this study. This study started with FeO total in the MELTS models instead of calculating FeO and Fe_2O_3. The MELTS models would probably work better if the ratio of Fe_2O_3 to FeO was set at various probable values for arc magmas. Using this technique would allow for MELTS to run models without setting the system to run along a specified oxygen buffer, which forces the system to be slightly open system in order to maintain the system at the oxygen fugacities dictated by the oxygen buffer.

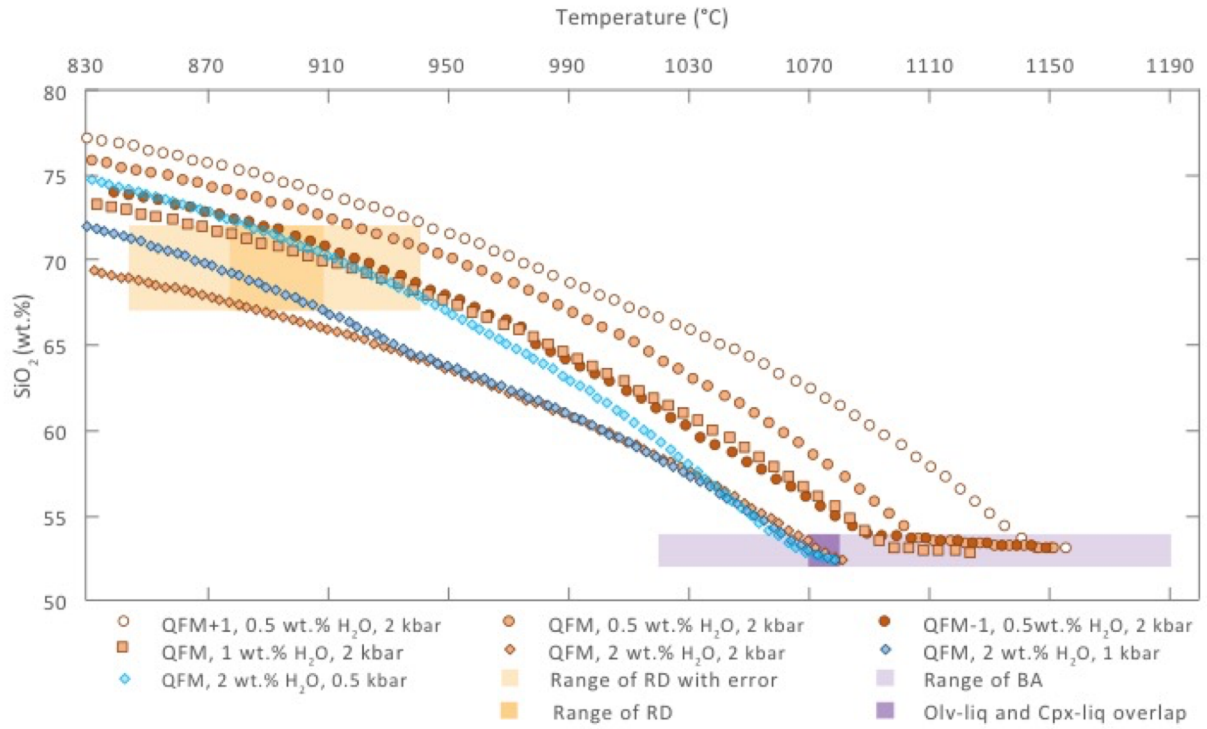

Figure 23. ***Temperature vs. SiO_2 plot of MELTS models.*** The purple box represents the SiO_2 and temperature range of the basaltic andesite. The light purple area represents the olivine-liquid and clinopyroxene-liquid temperature results, including error. The darker purple box represents the temperature range where the two thermometers overlap. Orange transparent box represents the SiO_2 and temperature range of the rhyodacite. The darker orange area represents the temperatures calculated while the lighter orange is the error on those calculations. The best fit models with respect to temperature and silica content are QFM, 2 wt.% H_2O at 0.5 kbar, 1 kbar, and 2 kbar. Another model that also works well is QFM, 1 wt.% H_2O, 2 kbar.

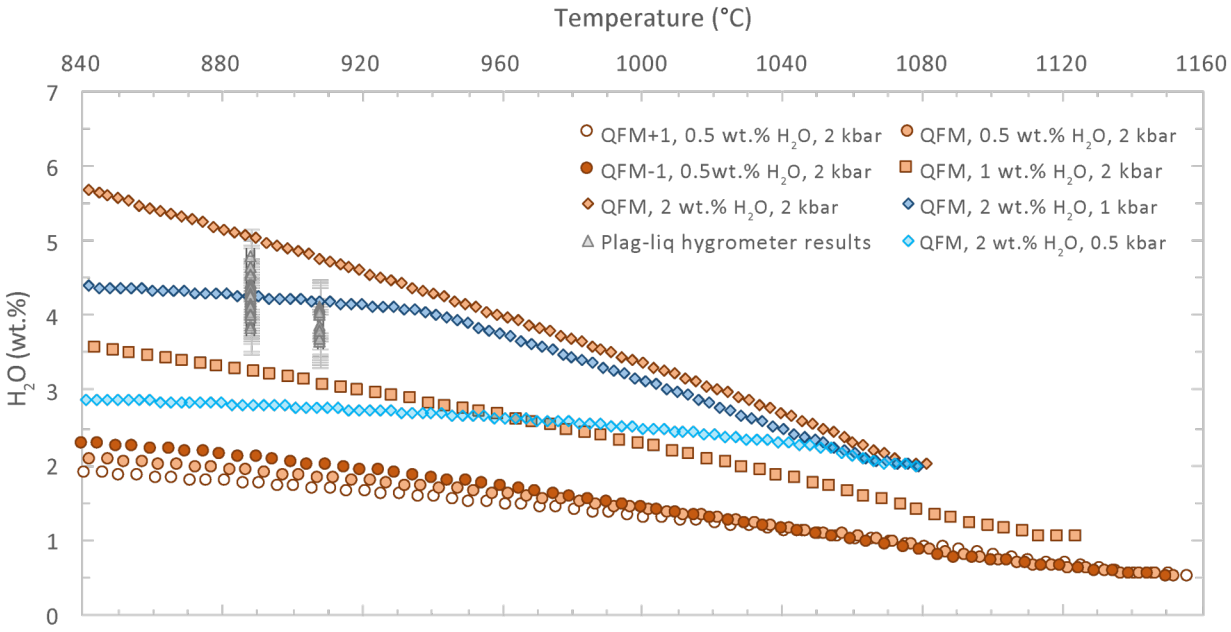

Figure 24. ***P-T-H_2O results from MELTS modeling.*** MELTS models starting with 0.5 wt.% H_2O, 1 wt.% H_2O, and 2 wt.% H_2O. Results of hygrometer calculations are shown in grey with 1 sigma error bars. In this plot, the MELTS models following QFM buffer, starting with 2 wt.% H_2O, and at pressures of 1 or 2 kbar work best.

5 Discussion

5.1 Unimak CFE: Fisher CFE or Shishaldin CFE?

The deposits studied here have been proposed to be from two different CFEs based on field evidence (Stelling, pers. comm.) S-type deposits have a diagnostic sequence of thin basal lapilli pumice layers, approximately equal thicknesses of blonde rhyodacite pumice and black basaltic andesite scoria, the latter two separated by a thin zone of banded pumice. These deposits occur on the flanks of Shishaldin Volcano and generally thicken toward the Shishaldin summit. In contrast, F-type deposits have a sharp basal contact between bedrock and overlying tan rhyodacite pumice, a sharp contact between the pumice fall and the overlying ignimbrite containing banded pumice, and lacks a discrete banded pumice layer and a separate scoria fall layer.

Rhyodacite and basaltic andesite from the different deposits are nearly identical in terms of their chemical compositions and mineral content. Because the crystallinity of both the basaltic andesite and rhyodacite is very low, subtle differences in observed mineral compositions and textures may be the result of incomplete sampling of the magma upon eruption. Although S-type samples contain compositionally zoned pyroxene and the F-type samples do not, these textures are only observed in the finely laminated lapilli-sized basal units that likely represent the initial phase of a single CFE. Oxygen isotope chemistry of S-type samples matches chemistry previously described for the Fisher CFE (Bindeman et al., 2001). The low $\delta^{18}O$ signatures observed in the S-type and F-type CFE phases are matched in only a few volcanic systems worldwide and only one other in the Aleutian Arc (Okmok; Bindeman et al., 2001). The low isotopic signature of the S-type and F-type deposits differs from other Shishaldin samples and pre-CFE Fisher samples that have higher $\delta^{18}O$ compositions (Bindeman et al., 2001). Therefore, based on the overwhelming compositional and textural similarity, I conclude that the S-type and F-type samples are from the same magma system, and that the different field characteristics of each deposit type represent complexity in eruption and depositional dynamics. The thickening of the S-type deposits toward Shishaldin may be due to local geomorphology and geographic blocking by Shishaldin. For the remainder of this discussion I will ignore the distinction between S-type and F-type rhyodacite. Additionally, because there appears to be only a single, complex eruption, the

source of this material is assumed to be Fisher based on the presence of a large caldera and prior mapping of Fisher CFE deposits.

5.2 Fisher CFE oxygen isotope geochemistry

Bindeman et al. (2001) suggests that the Fisher CFE deposits can be distinguished from other regional deposits by their low $\delta^{18}O$ values. The anomalously low $\delta^{18}O$ signature observed in the Fisher CFE rhyodacite requires unusual magmatic processes. Bindeman et al. (2001) interpreted the low $\delta^{18}O$ isotopic signature to reflect assimilation of low $\delta^{18}O$ rocks that are otherwise geochemically similar to the Fisher CFE magmas, presumably hydrothermally-altered wall rock. Oxygen isotope chemistry is so far the only evidence for assimilation in the pre-Fisher CFE magmatic system. To account for the exceptionally low $\delta^{18}O$ signature of Fisher rocks, Bindeman et al. (2001) further suggested alteration by heated glacial meltwater, which would be isotopically lighter than typical meteoric water.

The wide spread in $\delta^{18}O$ values (Figs. 17, 18) indicates that the light $\delta^{18}O$ signature is heterogeneous. There are several possible explanations for these isotopic signatures. One possibility is incomplete assimilation of wall rock material or that assimilation occurred shortly prior to eruption and was not well mixed within the magma. However, the lower oxygen isotope values of orthopyroxene collected from the basaltic andesite compared to those collected in the rhyodacite is mysterious (Fig. 17a). If the orthopyroxenes in the basaltic andesite were from the co-erupted rhyodacite, then the oxygen isotope values should match considering that oxygen isotope diffusion occurs over longer timescales than cation diffusion. The interpretation that the orthopyroxene was instead from the wall rock is also unlikely considering the basaltic andesite lacks orthopyroxene and thus wall rock that is similar in composition to the Fisher CFE basaltic andesite would likely also lack orthopyroxene. The wall rock is likely similar in composition to the basaltic andesite because most of the eruptive material on Unimak is basaltic andesitic in composition. Another possibility is that the rhyodacite had at least one population of antecrystic orthopyroxenes, which would mean that one or two populations of orthopyroxenes each came from a different magma and start with different $\delta^{18}O$ values. Yet it would seem odd that all of one population were only analyzed in the basaltic andesite and all of the other population was analyzed in the rhyodacite. Thus, either the orthopyroxenes in the basaltic

andesite are not from the co-erupted rhyodacite, the basaltic andesite entrained these crystals from a particular zone in the rhyodacite that the orthopyroxenes populate, or the basaltic andesite changed the $\delta^{18}O$ values of the rhyodacite-derived orthopyroxenes during entrainment of silicic selvedges from the co-erupted rhyodacite.

Outlier or multiple populations of oxygen isotope values may either represent antecrysts, crystals from the wall rock, or differential diffusion of oxygen within the magma. The anomalously light clinopyroxene analysis ($\delta^{18}O$ = 3.42‰; Figs. 17b, 17d, and 18d) represents a large (~1.5 x 1.25 mm), dark, equant crystal with slightly rounded edges whereas most rhyodacite clinopyroxene crystals are small, needle-like or prismatic crystals. This clinopyroxene crystal may have been incorporated from the wall rock. Although orthopyroxenes in the basaltic andesite (all of which are surrounded by silicic selvedges) are indistinguishable from those in the rhyodacite in terms of their petrography and major element chemistry, orthopyroxenes collected from the basaltic andesite are isotopically lighter than rhyodacite orthopyroxenes and are not in oxygen isotopic equilibrium with basaltic andesite plagioclase. Oxygen diffusion occurs at a much slower rate than cation diffusion, thus it is unlikely that the orthopyroxene's oxygen isotope chemistry is reacting to the basaltic andesite's oxygen isotope chemistry and not exhibiting changes in major element chemistry.

The oxygen isotope chemistry of the basaltic andesite is not well constrained in this study or in previous work as the silicic selvedges around crystals within the basaltic andesite were not considered during sampling. However, an olivine phenocryst from the Fisher CFE basaltic andesite has a $\delta^{18}O$ of 3.98‰, compared to typical magmatic olivine $\delta^{18}O$ values of ~4.8±0.1‰ ($\Delta^{18}O_{melt\text{-}olivine}$ = 0.7±0.1‰; Bindeman, 2008). The isotopically light olivine from the Fisher basaltic andesite is similar to cumulate inclusions erupted after the Fisher CFE (Bindeman et al., 2001). Because the olivine is isotopically similar to the olivine-bearing cumulate (~45% crystalline) and olivine is observed to be a phenocryst of the basaltic andesite, then it is unlikely an isotopic signature of the wall rock but it cannot be removed as a possibility since this study did not analyze that olivine. This also suggests assimilation in the basaltic andesite occurred prior to the

crystallization of the cumulates due to their low $\delta^{18}O$ values if the olivine-bearing cumulate is the solid residue of the basaltic andesite.

5.3 Fisher magmatic system

Three possible endmember magmatic plumbing systems are thought to be able to produce a bimodal eruption like that observed on Unimak Island (Hildreth et al., 1987; Fig. 1): (1) a single stratified magma chamber in which the mafic magma fractionates to a less dense felsic magma that rises to the top of the chamber (Hypothesis #1 in Fig. 1); (2) a hot mafic or primitive magma rising from mid- to deep crustal levels to inject into a shallow felsic magma reservoir, inciting eruption (Hypothesis #2 in Fig. 1)); or (3) multiple magma chambers existing simultaneously in the shallow crust that interact immediately prior to or during eruption (Hypothesis #3 in Fig. 1). Below I address each model in light of the above dataset.

5.3.1 Hypothesis #1

Models of fractional crystallization relationships between the basaltic andesite and rhyodacite are used as a test for hypothesis #1, that the rhyodacite magma and co-erupted basaltic andesite magma existed in a single stratified magma chamber. In this scenario, the rhyodacitic liquid is the residual liquid from fractional crystallization of the mafic magma. None of the fractionation models in this study could substantiate a genetic relationship based on major and minor element chemistry, mineral compositions, or paragenetic sequence. The discrepancies in the different fractionation models suggest a more complex arrangement than just a single, zoned magma chamber that Bindeman et al. (2001) suggests. Bindeman et al. (2001) argued that the basaltic andesite and rhyodacite were part of a single magma reservoir based on similar K/Rb and Zr/Hf ratios, as these ratios generally do not change with fractionation. However, the trace element modeling of Stelling (2003) does not show a fractionation link between the rhyodacite and the basaltic andesite, in agreement with the major element modeling of this study. Therefore hypothesis #1 can be rejected.

5.3.2 Hypothesis #2

The second hypothesis of pre-CFE magma plumbing is the injection of a mafic or primitive magma from the mid- to deep crust into a shallow, silicic magma reservoir. The basaltic andesite has a Mg# of ~36, suggesting

fractionation from a more primitive parent magma. It is possible for mantle-derived magmas to have low $\delta^{18}O$ values (<+5.5‰) but this would appear in all magmatic products derived from the primitive magmas. Pre-Fisher CFE deposits have normal $\delta^{18}O$ values (Bindeman et al., 2001) and thus the primitive magmatic source of the eruptive products must have a normal (~5.5‰) $\delta^{18}O$ signature. This suggests a different magmatic process for the Fisher pre-CFE and CFE magmas. Both the basaltic andesite and rhyodacite magmas have low $\delta^{18}O$, thus both magmas would have had to be in proximity to altered rocks, which could only occur near the surface (<7 km; Taylor, 1990). However, the basaltic andesite's low $\delta^{18}O$ signature is tenuous, but the pre-eruptive pressure estimates suggest the basaltic andesite was within the shallow crust of up to 4.7 kbar (which assuming a crustal density of 2.6 g/cm^3 is equivalent to ~12 km depth). This puts the basaltic andesite somewhere within the top third of the crust, which is approximately 35 km (Shillington et al., 2004). Thus, it is unlikely that the basaltic andesite came from the deep crust and inject into the rhyodacite, but the mid-crust cannot be ruled out conclusively.

5.3.3 Hypothesis #3

The third model for bimodal CFEs calls for magmas residing in separate, independent magma chambers. The lack of a fractional crystallization link between the Fisher CFE magmas suggests the magmas did not interact until shortly prior to eruption. The Fisher CFE also included an eruption of a lower silica dacite to the south of Fisher Volcano, called the Southern Dacite (Stelling, 2003; Stelling et al., 2005). These workers found the Southern Dacite magma to be compositionally unrelated to the North Dacite and the North Basaltic Andesite, and suggested this represented a physically and compositionally distinct magma reservoir. This lack of the South Dacite's relationship to the other Fisher CFE magmas further supports Stelling et al. (2005) and this study's conclusion that the Fisher system prior to its CFE was composed of multiple independent magma reservoirs (Fig. 25). Magmatic plumbing models of independent magma reservoirs may be more common than previously thought over single compositionally zoned magma chambers.

5.4 Assimilation in the Fisher CFE

A more plausible scenario to the low $\delta^{18}O$ signature of the Fisher CFE being mantle-derived is that the Fisher CFE magmas assimilated low $\delta^{18}O$ rocks. Because typical igneous rocks have $\delta^{18}O$ >5.5‰, the assimilated rock would need to have been hydrothermally altered by low-$\delta^{18}O$ meteoric water. To lower the $\delta^{18}O$ of the magmatic system, the rhyodacite would need to incorporate either a significant volume of slightly low $\delta^{18}O$ rock (altered by true meteoric waters), or a smaller volume of very low $\delta^{18}O$ rock. One possible source of very isotopically light material is rock altered by heated glacial meltwater, which has a $\delta^{18}O$ of ~-25‰ (Taylor and Sheppard, 1986; Bindeman et al., 2001). Alteration by glacial meltwater has been invoked to explain $\delta^{18}O$

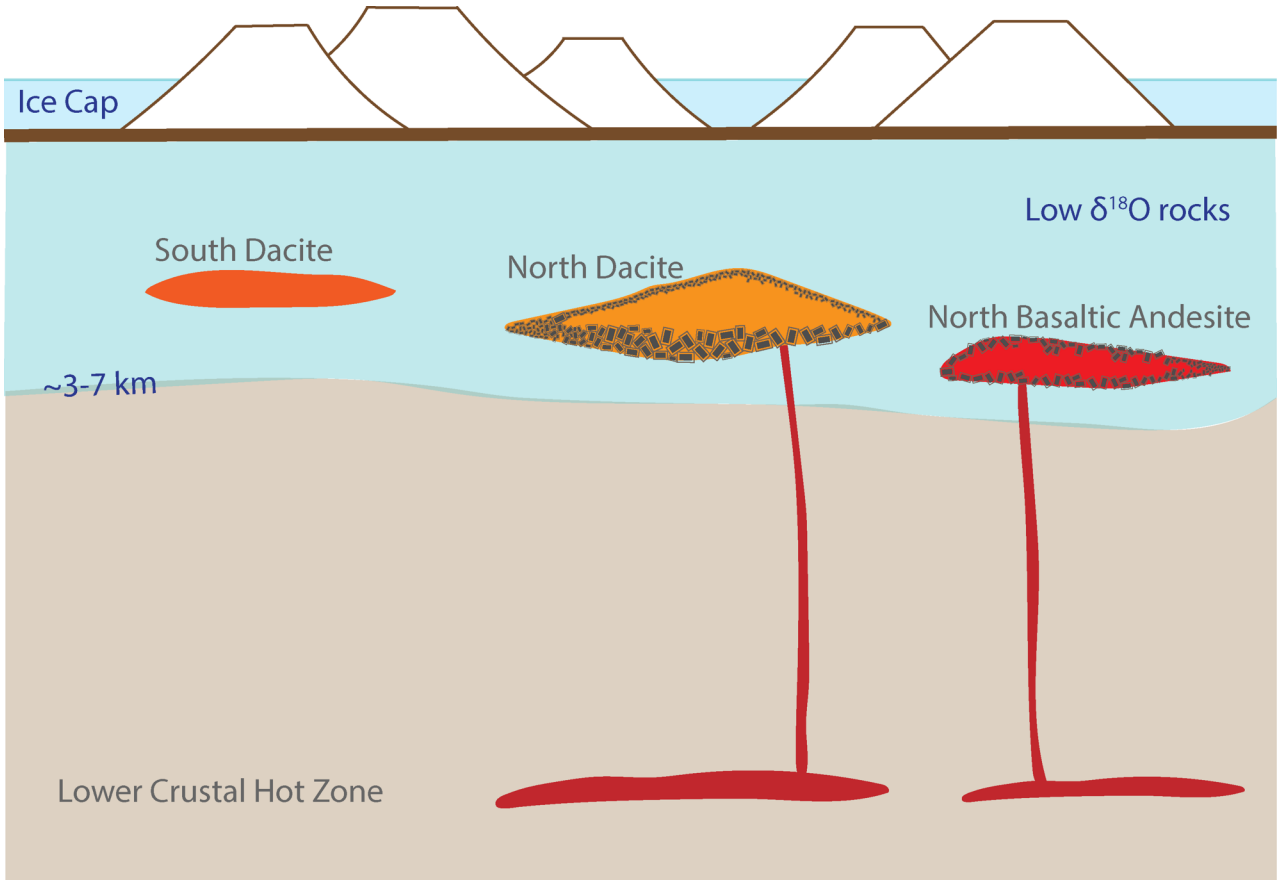

Figure 25. Petrogenetic model for the Fisher CFE. Only the Fisher CFE magmas are shown, but it is likely there were more compositionally-distinct magmas, such as a silicic magma that reaches ~72 wt.% (Stelling et al., 2005). The separate stratocones reflect the conclusions of Stelling (2003) and Stelling et al. (2005) that the Fisher system prior to the CFE was comprised of several stratocones. The blue zone in the crust represent the area that is likely hydrothermally-altered, low $\delta^{18}O$ rocks. However, it is not known if the South Dacite also has a low $\delta^{18}O$ signature. Figure is not to scale.

of -5‰ measured in a fossil hydrothermal system on Unalaska Island (Perfit and Lawrence, 1979). Fisher Caldera hosts a modern geothermal system and an older area of alteration is exposed in the northern caldera wall, suggesting additional alteration at depth. The infiltration of low $\delta^{18}O$ glacial meltwater was suggested by Bindeman et al., (2001) to be caused by highly fractured crust within an older caldera. These workers suggested the curved shape of the Tugamak Mountains (Fig. 2) could be the remnant of an old caldera that created permeable pathways for surface water to migrate to the subsurface. However, field work on Unimak Island found no evidence of an older caldera surrounding or at Fisher Volcano or as part of the Tugamak Mountains (P. Stelling pers. com.).

Although it is mathematically possible for meteoric water to infiltrate the magma and lower the $\delta^{18}O$ signature, it is unlikely to occur. Water cannot directly affect the lowering of the magmas for three main reasons according to Taylor and Sheppard (1986). One, the magma is under lithostatic pressure that is 2.5 to 3 times higher than the hydrostatic pressure in the fissure system. Two, grain-boundary diffusion from the fissure system into the magma would be required for water to directly affect the magma as any fractures at the contact zone would be filled with magma. Three, it would take the addition of ~15 wt.% H_2O to lower magmatic $\delta^{18}O$ by 2‰ (assuming $\delta^{18}O_{water}$ = -5‰). Given the volume estimates of the Fisher CFE of 20 – 100 km^3, (Stelling, 2003; Stelling et al., 2005; Gardner 2007), this would require infiltration of 3-15 km^3 of meteoric water into the Fisher CFE magmas. The incorporation of meteoric water could deplete $\delta^{18}O$ by at most 1‰, but it cannot account for any greater depletions.

5.5 Fisher CFE Pre-Eruptive Conditions

The mingling of the rhyodacite and basaltic andesite brought a hotter magma in contact with a cooler, more hydrous magma. The rhyodacite pre-eruptive temperature and water content were 844 – 941°C (including model error) and ~3.5 – 4.8 wt.% H_2O, respectively. The oxygen fugacity of the magma was -13.1 to -12.6 log units, which is an oxygen fugacity around the QFM buffer calculated at ~2 kbars.

Pre-eruptive conditions for the basaltic andesite are not as well-constrained as those of the rhyodacite. The pre-eruptive temperature of the basaltic andesite was between 1036°C and 1207°C (including model error), with H_2O content between ~0.5 – 2 wt.% H_2O. Pressure estimates of up to 4.7 kbar suggest

the basaltic andesite resided within the shallow crust. The low Mg# of the basaltic andesite suggests residence in the shallow crust as well. If the low $\delta^{18}O$ signature in the Fisher CFE magmas was due to interaction with a low-$\delta^{18}O$ source, this would require that the basaltic andesite resided within the upper crust (<7 km based on penetration depths of shallow surface water circulation; Taylor, 1990) for an extended time.

5.6 The Mingling Timescales of the Fisher CFE

Selvedges of rhyodacite glass around orthopyroxene, plagioclase, and Fe-Ti oxide phenocrysts in the basaltic andesite provide relative time constraints on the entrainment of rhyodacite components within basaltic andesite. No orthopyroxenes are observed in the basaltic andesite without a selvedge of more silicic glass. The selvedge-wrapped orthopyroxenes within the basaltic andesite are euhedral and show no signs of textural disequilibrium. These orthopyroxenes are not in chemical equilibrium with the silicic selvedge surrounding them, but are in equilibrium with a representative rhyodacite glass composition. The silicic selvedge surrounding the orthopyroxene has ~1 wt.% MgO whereas the rhyodacite glass has ~0.6 wt.% MgO, so the closer to 0.6 wt.% MgO, the closer to equilibrium the orthopyroxene would be with the silicic selvedge. The silicic selvedge compositions are heterogeneous and form a mixing line between the rhyodacite composition and the basaltic andesite (Fig. 5). In contrast, Fe-Ti oxides with selvedges exhibit ilmenite exsolution or are resorbed. Because Fe-Ti oxides equilibrate faster and are more sensitive to environmental changes than orthopyroxenes (Blundy and Cashman, 2008), the selvedges containing the rhyodacite crystals could not have been entrained longer than the equilibration time of the Fe-Ti oxides. The magmas interacted long enough for the Fe-Ti oxides to develop textural disequilibrium but not long enough for the orthopyroxenes to develop similar textures and to reach disequilibrium with the rhyodacite. Although precise time constraints cannot be determined from these data, they suggest that the interaction between the magmas was short and occurred just prior eruption. Plagioclase experiments show that this timing is likely on a scale of days or weeks. Donaldson (1985) suggests that a ~4 mm-diameter andesine crystal would require ~20 days to dissolve in a basaltic to andesitic melt. Most rhyodacite plagioclase crystals are smaller than 4 mm and have little to no petrographic evidence of resorption. Thus, for these crystals to be preserved with little to no resorption, less than 20 days passed between mingling and eruption.

The timing of assimilation of altered country rock is more difficult to quantify. At magmatic temperatures, oxygen isotope diffusion in minerals occurs on timescales of 1 to 100s of years, which is relatively short compared to crystal fractionation timescales (Bindeman, 2008) and the relatively rapid oxygen isotope diffusion in plagioclase requires shorter time scales yet than other minerals. Thus, assimilation likely occurred <100 years to preserve the oxygen isotope disequilibria seen in rhyodacite phenocrysts.

Compositional zoning in olivine and oxygen isotope heterogeneity in both basaltic andesite and rhyodacite magmas provide additional constraint on pre-eruptive processes. It is uncertain whether the olivine observed within the rhyodacite is from the co-erupted basaltic andesite or incorporated from the wall rock. The color of the olivine is similar to the olivines from the co-erupted basaltic andesite, but the rim shows chemical equilibration with the rhyodacite glass. The preservation of Fe-Mg zoning suggests that the olivine spent less than 100 years in the magma prior to eruption (Costa and Dungan, 2005). This is comparable to the time estimated to explain oxygen isotope disequilibria. Although xenocrystic olivine and pyroxene crystals are observed in the rhyodacite, none of the crystals have mafic glass selvedges and could be remnants of the wall rock after assimilation.

5.7 The Mechanics of the Fisher CFE

The eruption scenario proposed in this study needs to satisfy the presence of silicic selvedges within the basaltic andesite, little to no eruption of crystal mush of either erupting magma, and the sequence of compositions erupted. A plausible scenario for the Fisher CFE could be as follows: the rhyodacite began to erupt from a shallow reservoir, with an initial series of small, localized explosive eruptions depositing lapilli-sized clasts in fine layers on the lower west flanks of Shishaldin. The depressurization caused by the withdrawal of magma from the rhyodacite reservoir caused a nearby shallow reservoir of basaltic andesite to experience a pressure gradient, inciting it to erupt in response (Fig. 26). Mingling of the two magmas then occurs upon ascent, creating banded pumice, xenocrysts of plagioclase and orthopyroxene wrapped with silicic glass selvedges in the basaltic andesite, and other mingling textures. Following the eruption of mingled compositions, eruption a basaltic andesite scoria was directed eastward toward Shishaldin. Caldera collapse likely followed the basaltic andesite eruptive phase, increasing magma pathways and causing the eruption

column to collapse northward, creating a pyroclastic flow containing basaltic andesite scoria, rhyodacite pumice, and banded pumice. This proposed eruptive sequence accounts for the crystal poor nature of both magmas as well as the isotopic data, modeling results, and petrography. Exactly how the magmas interacted beneath the surface is still uncertain, but one of the magmas ascended toward the surface and intersected the other. It is possible the basaltic andesite intruded first into the rhyodacite before the rhyodacite started erupting but not long enough for disequilibrium textures to be obvious in crystals within silicic selvedges. The presence of rhyodacite selvedges within the basaltic andesite may suggest that the rhyodacite intruded into the basaltic andesite.

Assuming ascent rates of ~1-3 m/s (roughly comparable to ascent rates determined for the 18 May 1980 eruption of Mt. St. Helens; Rutherford and Gardner, 2015), it would take ~28-83 min for a magma to rise from 5 km depth to the surface. The dissolution rate of plagioclase is rapid enough that as much as 12 microns of dissolution could have occurred during the 83 minutes of ascent, assuming a linear dissolution model using 4 mm crystals dissolving in 20 days (Donaldson, 1985). Plagioclase crystals in the ignimbrite are only partially resorbed (up to ~150 μm) at the rim with some internal resorption and plagioclase crystals contained in silicic selvedges in the basaltic andesite show no resorption.

The Fisher CFE's deposits are consistent with interpretations of similar CFE deposits at Aniakchak Volcano at 3430 yBP in Alaska (Larsen, 2006). The Aniakchak eruption started with early rhyodacite pumice fall followed by a mingling zone of rhyodacite and andesite pyroclastic flow, followed by an andesite pyroclastic flow. Additionally, 10s of micron-sized rhyodacite glass blebs are contained within the basaltic andesite scoria away from the banded pumice zone at Aniakchak similar to the Fisher CFE deposits. These micron-scale blebs are similar to the selvedge-wrapped crystals observed in the Fisher CFE basaltic andesite. The Aniakchak CFE model for mingling does not require the two magmas to be related or that the mafic component came from the deep crust, which the Fisher CFE also does not require.

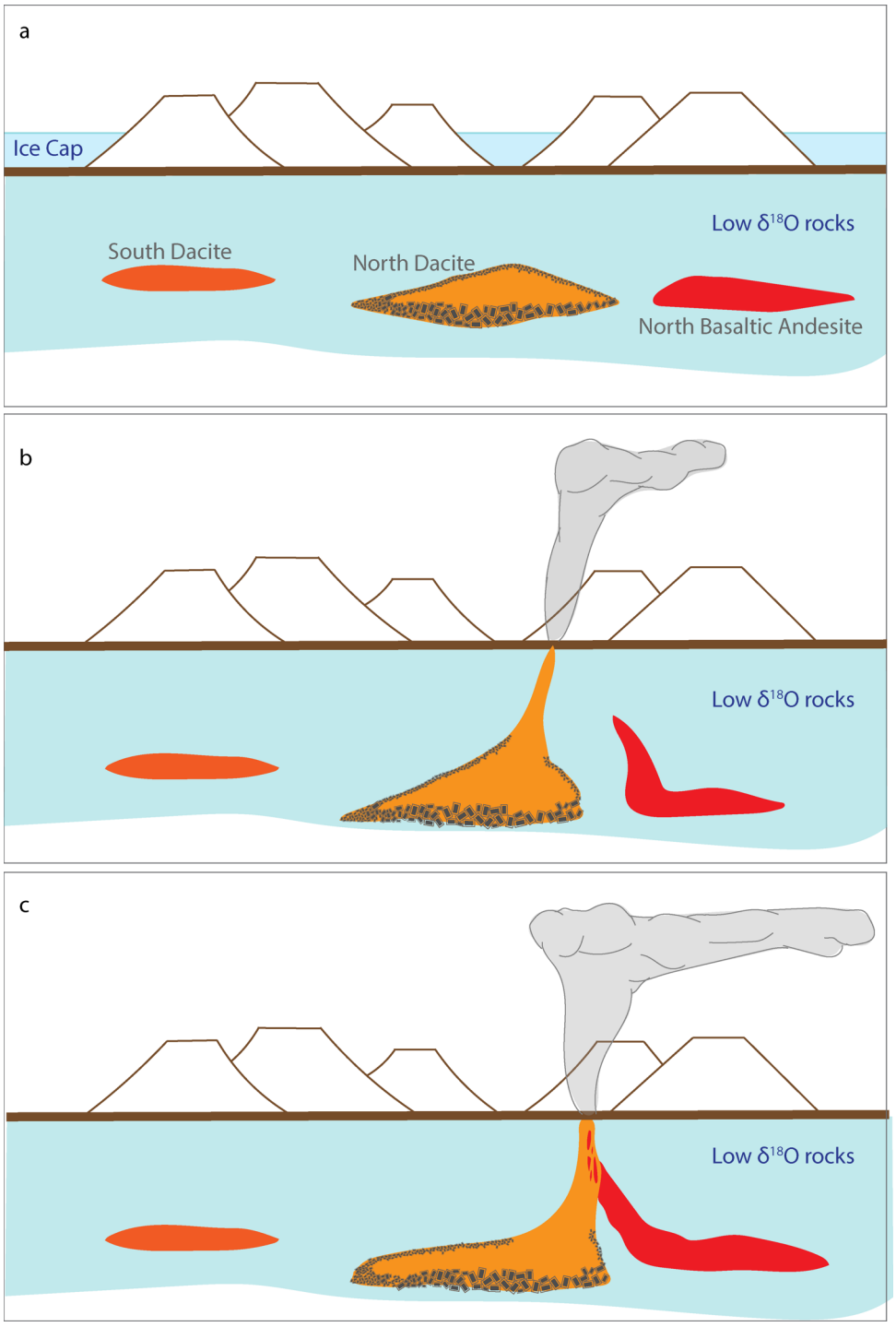

Figure 26. Fisher plumbing and CFE eruption. **(a)** Prior to the Fisher CFE, the glacial meltwater hydrothermally alters the shallow upper crust up to 7 km and the different magmas are in their respective, separate magma reservoirs. **(b)** Rhyodacite magma starts to erupt, causing the basaltic andesite to destabilize and start to ascend toward the surface. **(c)** Rhyodacite and basaltic andesite mingle as the basaltic andesite also starts to erupt. The exact timing of this mingling is unknown, likely only lasting a day at most to preserve disequilibrium textures, and could occur nearer or into the rhyodacite magma chamber. Soon the eruption will be predominantly basaltic andesite. Later mechanical overturn of the two magmas would cause both to erupt, eventually becoming a pyroclastic flow at the surface. Vent location for either the South Dacite or Northern magmas are unknown. Figure is not to scale. Model is based on Larsen (2006).

6 Conclusion

Bimodal CFEs are complex eruptions that have been proposed to have erupted from various magmatic plumbing systems. Two of the most prevalent magmatic plumbing systems are a single compositionally zoned magma chamber and a complex reservoir of multiple independent magmas, both of which have been proposed previously for the Fisher CFE. The magmatic plumbing system in this study was determined using pre-eruptive conditions (T, P, H_2O content), fractional crystallization modeling, and oxygen isotope chemistry. The presence of two different sequences of CFE deposits suggests the possibility of two CFEs on Unimak Island, one from Fisher Volcano and the other from Shishaldin Volcano. Based on compositional overlap in major element and oxygen isotope chemistry, this study concludes that the two different sequences represent eruptive complexities within a single eruption from Fisher Volcano. The Fisher CFE magmas have an uncommon low $\delta^{18}O$ signature. Most of the crystals examined in this study are in oxygen isotopic disequilibrium and plagioclase shows the greatest variability in $\delta^{18}O$ values.

The rhyodacite had a temperature range of 844 – 941°C, -13.1 to -12.6 log units fO_2 (~QFM buffer), ~3.5 – 4.8 wt.% H_2O, and resides within the shallow crust. The co-erupted basaltic andesite had a temperature of 1065 – 1147°C and 0 – 2.5 wt.% H_2O. Constraints on the oxygen fugacity of the basaltic andesite were not possible using two-oxide barometry, but based on MELTS models, the basaltic andesite clinopyroxene compositions are consistent with oxygen fugacities following the QFM+1 buffer, indicating more oxidizing conditions than for the rhyodacite.

Based on the geochemistry and fractionation modeling, the Fisher magmatic system is comprised of multiple, independent magma reservoirs prior to the Fisher CFE. However, it is possible that the basaltic andesite resided in the mid-crust due to a small dataset of pre-eruptive pressure. The rhyodacite does not appear to have evolved directly from the co-erupted basaltic andesite. Large compositionally zoned magma chambers may be less common than previously thought in support of smaller, independent magma reservoirs. Both the rhyodacite and the basaltic andesite have a low $\delta^{18}O$ signature (although the oxygen isotope values for the basaltic andesite are not well constrained), suggesting that the mechanism for $\delta^{18}O$ depletion was similar for both magmas. This could be the result of assimilation of isotopically light altered country rock as

suggested by Bindeman et al. (2001), which likely occurred <100 years prior to eruption to preserve the oxygen isotope disequilibria seen in rhyodacite phenocrysts, particularly plagioclase.

References

Andersen, D.J., & Lindsley, D.H. (1985). New (and final!) models for the Ti-magnetite/ilmenite geothermometer and oxygen barometer. *Abstract AGU 1985 Spring Meeting Eos Transactions. American Geophysical Union* **66**, 416.

Bacon, C.R., & Hirschmann, M.M. (1988). Mg/Mn partitioning as a test for equilibrium between coexisting Fe-Ti oxides. *American Mineralogist* **73**, 57-61.

Bea, F., Fershtater, G., & Corretgé, L. G. (1992). The geochemistry of phosphorus in granite rocks and the effect of aluminium. *Lithos* **29**, 43-56.

Beget, J., Nye, C., & Stelling, P.L. (1998). Postglacial collapse and regrowth of Shishaldin Volcano, Alaska, requires high eruption rates. *Transactions-American Geophysical Union* **70**, S359.

Beget, J.E., Nye, C.J., Schaefer, J.R., & Stelling, P. L. (2002). Preliminary volcano-hazard assessment for Shishaldin Volcano, Alaska. *Alaska Division of Geological & Geophysical Surveys Report of Investigations RI 2002-4*, 28 p., 1 sheet, scale 1:500,000.

Bernard, A., Knittel, U., Weber, B., Weis, D., Albrecht, A., Hattori, K., Klein, J., & Oles, D. (1996). Petrology and Geochemistry of the 1991 Eruption Products of Mount Pinatubo. In Newhall, C. G., & Punongbayan, R. S. (eds) *Fire and Mud. Eruptions and Lahars of Mount Pinatubo, Philippines*. Seattle: University of Washington Press, pp. 767-797.

Bindeman, I.N. (2008). Oxygen Isotopes in Mantle and Crustal Magmas as Revealed by Single Crystal Analysis. *Reviews in Mineralogy & Geochemistry* **69**, 445-478.

Bindeman, I.N., Fournelle, J.H., & Valley, J.W. (2001). Low-$\delta^{18}O$ tephra from a compositionally zoned magma body: Fisher Caldera, Unimak Island, Aleutians. *Journal of Volcanology and Geothermal Research* **111**, 35-53.

Braitseva, O.A., Melekestsev, I.V., Ponomareva, V.V., Kirianov, & V.Yu. (1996). The caldera-forming eruption of Ksudach volcano about cal. A.D. 240: the greatest explosive event of our era in Kamchatka, Russia. *Journal of Volcanology and Geothermal Research* **70**, 49-65.

Carson, E.C., Fournelle, J.H., Miller, T.P., & Mickelson, D.M. (2002). Holocene tephrochronology of the Cold Bay area, southwest Alaska Peninsula. *Quaternary Science Reviews* **21**, 2213–2228.

Chiba, H., Chacko, T., Clayton, R.N., & Goldsmith, J.R. (1989). Oxygen isotope fractionations involving diopside, forsterite, magnetite, and calcite: Application to geothermometry. *Geochimica et Cosmochimica Acta* **53**, 2985-2995.

Costa, F., & Dungan, M. (2005). Short time scales of magmatic assimilation from diffusion modeling of multiple elements in olivine. *Geology* **33**, 837-840.

Cusano, P., Palo, M., & West, M. E. (2015). Long-period seismicity at Shishaldin volcano (Alaska) in 2003–2004: Indications of an upward migration of the source before a minor eruption. *Journal of Volcanology and Geothermal Research* **291**, 14-24.

Donaldson, C.H. (1985). The rates of dissolution of olivine, plagioclase, and quartz in a basalt melt. *Mineralogical Magazine* **49**, 683-693.

Dreher, S.T., Eichelberger, J.C., & Larsen, J.F. (2005). The Petrology and Geochemistry of the Aniakchak Caldera-forming Ignimbrite, Aleutian Arc, Alaska. *Journal of Petrology* **46**, 1747–1768.

Eiler, J.M. (2001). Oxygen isotope variations in basaltic lavas and upper mantle rocks. *Reviews in Mineralogy and Geochemistry* **43**, 319-364.

Eiler, J. M., Crawford, A., Elliott, T. I. M., Farley, K. A., Valley, J. W., & Stolper, E. M. (2000). Oxygen isotope geochemistry of oceanic-arc lavas. *Journal of Petrology* **41**, 229-256.

Fournelle, J. H. (1988). The geology and petrology of Shishaldin volcano, Unimak Island, Aleutian arc, Alaska: Doctoral dissertation, Johns Hopkins University Press.

Funk, J.M. (1973). Late Quaternary geology of Cold Bay, Alaska, and vicinity: MS thesis, University of Connecticut.

Gardner, J.E. & Denis, M.H. (2004). Heterogeneous bubble nucleation on Fe-Ti oxide crystals in high-silica rhyolitic melts. *Geochimica et Cosmochimica Acta* **68**, 3587-3597.

Gardner, J. E., Burgisser, A., & Stelling, P.L. (2007). Eruption and deposition of the Fisher Tuff (Alaska): evidence for the evolution of pyroclastic flows. *The Journal of Geology* **115**, 417-435.

Ghiorso, M.S. (1994). Algorithms for the estimation of phase stability in heterogeneous thermodynamic systems. *Geochimica et Cosmochimica Acta* **58**, 5489–5501.

Ghiorso, M.S. & Sack, R.O. (1995). Chemical mass transfer in magmatic processes IV. A revised and internally consistent thermodynamic model for the interpolation and extrapolation of liquid-solid equilibria in magmatic systems at elevated temperatures and pressures. *Contributions to Mineralogy and Petrology* **119**, 197–212.

Ghiorso, M.S., & Evans, B.W. (2008). Thermodynamics of rhombohedral oxide solid solutions and a revision of the Fe-Ti two-oxide geothermometer and oxygen-barometer. *American Journal of Science* **308**, 957-1039.

Ghiorso, M.S., & Gualda, G.A. (2015). An H_2O–CO_2 mixed fluid saturation model compatible with rhyolite-MELTS. *Contributions to Mineralogy and Petrology* **169**, 1-30.

Gong, W., F.J. Meyer, C.-W. Lee, Z. Lu, J. & Freymueller. (2015). Measurement and interpretation of subtle deformation signals at Unimak Island from 2003 to 2010 using weather model-assisted timeseries InSAR. *Journal of Geophysical Research Solid Earth* **120**, 1174–1194, doi:10.1002/2014JB011384.

Gualda, G.A.R., Ghiorso M.S., Lemons R.V., & Carley T.L. (2012). Rhyolite-MELTS: A modified calibration of MELTS optimized for silica-rich, fluid-bearing magmatic systems. *Journal of Petrology* **53**, 875-890.

Harrison, T.M., & Watson, E.B. (1984). The behavior of apatite during crustal anatexis: equilibrium and kinetic considerations. *Geochimica et Cosmochimica Acta* **48**, 1467-1477.

Hildreth, W. (1987). New perspectives on the eruption of 1912 in the Valley of Ten Thousand Smokes, Katmai National Park, Alaska. *Bulletin of Volcanology* **49**, 680-693.

Hildreth, W., & Fierstein, J. (2000). Katmai volcanic cluster and the great eruption of 1912. *Geological Society of America Bulletin* **112**, 1594-1620.

Hildreth, W., & Fierstein, J. (2012). The Novarupta-Katmai eruption of 1912—largest eruption of the twentieth century; centennial perspectives: U.S. Geological Survey Professional Paper 1791, 259 p. (Available at https://pubs.usgs.gov/pp/1791/.)

Lange, R. A., Frey, H. M., & Hector, J. (2009). A thermodynamic model for the plagioclase-liquid hygrometer/thermometer. *American Mineralogist* **94**, 494-506.

Lepage, L. D. (2003). ILMAT: an Excel worksheet for ilmenite–magnetite geothermometry and geobarometry. *Computers & Geosciences* **29**, 673-678.

Mann, D.H., & Peteet, D.M. (1994). Extent and timing of the last glacial maximum in southwestern Alaska. *Quaternary Research* **42**, 136-148.

Miller, T.P., & Smith, R. L. (1977). Spectacular mobility of ash flows around Aniakchak and Fisher calderas, Alaska. *Geology* **5**, 173-176.

Miller, T.P., McGimsey, R.G., Richter, D.H., Riehle, J.R., Nye, C.J., Yount, M. E., & Dumoulin, J.A. (1998). Catalog of the historically active volcanoes of Alaska: US Geological Survey Open-File Report **98**, 582 p.

Moran, S.C., Kwoun, O., Masterlark, T., & Lu, Z. (2006). On the absence of InSAR-detected volcano deformation spanning the 1995–1996 and 1999 eruptions of Shishaldin Volcano, Alaska. *Journal of Volcanology and Geothermal Research* **150**, 119-131.

Neave, D. A., & Putirka, K. D. (2017). A new clinopyroxene-liquid barometer, and implications for magma storage pressures under Icelandic rift zones. *American Mineralogist* **102**, 777-794.

Pallister, J. S., Hoblitt, R.P. & Reyes, A. G. (1992). A basalt trigger for the 1991 eruptions of Pinatubo volcano? *Nature* **356**, 426-428.

Pallister, J. S., Hoblitt, R. P., Meeker, G. P., Knight, R. J., & Siems, D. F. (1996). Magma mixing at Mount Pinatubo volcano: petrographical and chemical evidence from the 1991 deposits. In Newhall, C. G., & Punongbayan, R. S. (eds) *Fire and Mud. Eruptions and Lahars of Mount Pinatubo, Philippines*. Seattle: University of Washington Press, pp. 687-732.

Perfit, M.R. & Lawrence, J.R. (1979). Oxygen isotopic evidence for meteoric water interaction with the Captains Bay Pluton, Aleutian Islands. *Earth and Planetary Science Letters* **45**, 16-22.

Plank, T., Kelley, K.A., Zimmer, M.M., Hauri, E.H., & Wallace, P.J. (2013). Why do mafic arc magmas contain ~4 wt% water on average? *Earth and Planetary Science Letters* **364**, 168-179, doi: 10.1016/j.epsl.2012.11.044.

Putirka, K.D. (1999). Clinopyroxene + liquid equilibria to 100 kbar and 2450 K. *Contributions to Mineralogy and Petrology* **135**, 151-163.

Putirka, K.D. (2008). Thermometers and Barometers for Volcanic Systems. *Reviews in Mineralogy and Geochemistry* **69**, 61-120.

Putirka, K., Johnson, M., Kinzler, R., Longhi, J., & Walker, D. (1996). Thermobarometry of mafic igneous rocks based on clinopyroxene-liquid equilibria, 0–30 kbar. *Contributions to Mineralogy and Petrology* **123**, 92-108.

Roeder, P.L., & Emslie, R.F. (1970). Olivine-liquid equilibrium. *Contributions to Mineralogy and Petrology* **29**, 275-289.

Rutherford, M.J., & Gardner, J.E. (2015). Rates of Magma Ascent. Sigurdsson, H., Houghton, B., McNutt, S., Rymer, H. and Stix, J., The Encyclopedia of Volcanoes. Elsevier, 207-218.

Ryan, W.B.F., Carbotte, S.M., Coplan, J.O., O'Hara, S., Melkonian, A., Arko, R., Weissel, R.A., Ferrini, V., Goodwillie, A., Nitsche, F., Bonczkowski, J., & Zemsky, R. (2009). Global Multi-Resolution Topography synthesis. *Geochemistry, Geophysics, Geosystems* **10**, Q03014, doi:10.1029/2008GC002332.

Shillington, D.J., Van Avendonk, H.J., Holbrook, W.S., Kelemen, P.B., and Hornbach, M.J. (2004). Composition and structure of the central Aleutian island arc from arc-parallel wide-angle seismic data. *Geochemistry, Geophysics, Geosystems* **5**, Q10006, doi:10.1029/2004GC000715.

Sparks, R.S.J., & Marshall, L.A. (1986). Thermal and Mechanical Constraints on Mixing Between Mafic and Silicic Magmas. *Journal of Volcanology and Geothermal Research* **29**, 99-124.

Sparks, R.S.J., & Sigurdsson, H. (1977). Magma mixing: a mechanism for triggering acid explosive eruptions. *Nature* **267**, 315-318.

Stelling, P.L. (2003). Volcanism on Unimak Island, Alaska, USA: A special focus on Shishaldin and Fisher volcanos [Ph.D. thesis]: University of Alaska Fairbanks, 193 p.

Stelling, P., Gardner, J. E., & Begét, J. (2005). Eruptive history of Fisher Caldera, Alaska, USA. *Journal of Volcanology and Geothermal Research* **139**, 163-183.

Stormer Jr, J.C. (1983). The effects of recalculation on estimates of temperature and oxygen fugacity from analyses of multicomponent iron-titanium oxides. *American Mineralogist* **68**, 586-594.

Syracuse, E.M., & Abers, G.A. (2006). Global compilation of variations in slab depth beneath arc volcanoes and implications. *Geochemistry, Geophysics, Geosystems* **7**, Q05017, doi:10.1029/2005GC001045.

Taylor Jr, H.P. (1990). Oxygen and hydrogen isotope constraints on the deep circulation of surface waters into zones of hydrothermal metamorphism and melting. *The role of fluids in crustal processes* ***72***, 72-95.

Taylor Jr., H.P. & Sheppard, S.M.F. (1986). Igneous rocks: I. Processes of isotopic fractionation and isotopic systematics. *Reviews in Mineralogy and Geochemistry* **16**, 227-272.

Waters, L.E., & Lange, R.A. (2015). An updated calibration of the plagioclase-liquid hygrometer-thermometer applicable to basalts through rhyolites. *American Mineralogist* **100**, 2172-2184.

Zimmer, M.M. (2008). Water in Aleutian Magmas: Its Origin in the Subduction Zone and its Effects on Magma Evolution: Ph.D. Thesis. Boston University, Boston, MA, 448 p.

Zimmer, M.M., Plank, T., Hauri, E.H., Yogodzinski, G.M., Stelling, P., Larsen, J., Singer, B., Jicha, B., Mandeville, C., & Nye, C.J. (2010). The role of water in generating the calc-alkaline trend: new volatile data for Aleutian magmas and a new tholetiitic index. *Journal of Petrology* **51**, 2411–2444, doi:10.1093/petrology/egq062.

Appendix A1. Major element chemistry of glass in rhyodacite samples.
Abbreviations: S-type = Shishaldin-type, F-type = Fisher-type, RD = rhyodacite
*Glass analyses done by Alaska Volcano Observatory (AVO) at USGS Menlo Park, CA.

Sample	Analysis ID	Description	SiO_2	Al_2O_3	TiO_2	FeOt	MnO	MgO	CaO	Na_2O	K_2O	Cl	P_2O_5	Total	Mg #
15S-PS-5E	15S-PS-5E_g2	S-type pumice RD	66.91	14.39	0.61	4.29	0.20	0.63	2.27	1.83	2.09	0.18	0.20	93.59	21
	15S-PS-5E_g1	S-type pumice RD	66.02	14.69	0.48	4.08	0.19	0.65	2.28	6.34	2.31	0.16	0.19	97.40	22
	15S-PS-5E_g3	S-type pumice RD	67.46	15.33	0.58	4.52	0.24	0.63	2.38	6.21	2.53	0.20	0.17	100.25	20
	15S-PS-5E_g4	S-type pumice RD	67.16	15.04	0.48	4.32	0.19	0.63	2.35	6.18	2.58	0.17	0.18	99.27	21
	15S-PS-5E_g5	S-type pumice RD	65.36	14.81	0.56	4.18	0.24	0.65	2.34	5.50	2.37	0.19	0.20	96.39	22
	15S-PS-5E_g6	S-type pumice RD	67.45	15.20	0.63	3.98	0.20	0.64	2.41	5.24	2.32	0.18	0.17	98.40	22
	15S-PS-5E_g7	S-type pumice RD	69.06	15.43	0.66	4.15	0.18	0.65	2.57	5.33	2.46	0.17	0.17	100.84	22
FC-177B	177B_g1	S-type lapilli-sized RD - lithic?	69.22	15.11	0.53	3.75	0.19	0.48	2.18	5.25	2.54	0.17	0.20	99.61	19
	177B_g1	S-type lapilli-sized RD - lithic?	67.76	15.02	0.47	3.82	0.19	0.60	2.26	5.28	2.35	0.13	0.18	98.05	22
	177B_g2	S-type lapilli-sized RD	67.82	15.28	0.62	4.43	0.20	0.63	2.16	6.68	2.40	0.16	0.19	100.57	20
	177B_g2	S-type lapilli-sized RD	67.48	15.34	0.60	4.24	0.20	0.64	2.24	6.09	2.38	0.17	0.19	99.56	21
	177B_g4	S-type lapilli-sized RD	68.54	15.65	0.53	4.13	0.17	0.68	2.28	6.62	2.42	0.15	0.15	101.32	23
	177B_g4	S-type lapilli-sized RD	67.43	15.66	0.65	4.27	0.22	0.70	2.33	6.21	2.37	0.18	0.19	100.21	22
	177B_g4	S-type lapilli-sized RD	67.77	15.47	0.65	4.48	0.18	0.67	2.37	6.17	2.43	0.19	0.21	100.59	21
	177B_g5	S-type lapilli-sized RD	70.98	15.44	0.60	4.20	0.21	0.61	2.25	1.72	2.38	0.17	0.19	98.77	21
	177B_g6	S-type lapilli-sized RD	68.86	15.45	0.64	4.26	0.18	0.61	2.22	5.93	2.52	0.14	0.16	100.96	20
	177B_g7	S-type lapilli-sized RD	68.03	15.25	0.59	4.15	0.19	0.67	2.26	6.38	2.42	0.19	0.18	100.32	22
	177B_g7	S-type lapilli-sized RD	68.56	15.64	0.55	4.06	0.22	0.68	2.22	7.52	2.37	0.19	0.17	102.18	23
	177B_g7	S-type lapilli-sized RD	67.28	15.24	0.53	4.21	0.19	0.66	2.30	6.13	2.39	0.18	0.18	99.28	22
	177B_g8	S-type lapilli-sized RD	68.25	15.65	0.54	4.47	0.22	0.67	2.44	3.12	2.40	0.15	0.19	98.11	21
	177B_g8	S-type lapilli-sized RD	68.74	15.70	0.58	4.30	0.18	0.63	2.25	6.77	2.51	0.15	0.19	101.97	21
	177B_g9	S-type lapilli-sized RD	63.93	14.47	0.48	4.18	0.17	0.60	2.07	6.63	2.24	0.17	0.17	95.12	20
	177B_g9	S-type lapilli-sized RD	66.86	14.99	0.66	4.03	0.20	0.59	2.16	6.78	2.42	0.14	0.19	99.04	21
	177B_g9	S-type lapilli-sized RD	67.59	15.32	0.55	4.08	0.19	0.61	2.10	6.73	2.39	0.18	0.18	99.92	21
FC-183	FC183_g1	F-type pumice RD	66.25	15.15	0.69	4.93	0.22	0.77	2.57	6.12	2.25	0.17	0.27	99.40	22
	FC183_g2	F-type pumice RD	66.11	15.45	0.69	5.40	0.22	0.83	3.14	6.00	2.35	0.19	0.25	100.63	22
	FC183_g3	F-type pumice RD	66.53	15.48	0.70	5.47	0.24	0.83	2.88	6.48	2.20	0.16	0.25	101.23	21
	FC183_g4	F-type pumice RD	67.07	15.50	0.71	4.85	0.19	0.75	2.66	5.44	2.34	0.12	0.27	99.89	22
	FC183_g5	F-type pumice RD	66.19	15.09	0.73	5.60	0.24	0.89	3.16	6.50	2.24	0.17	0.26	101.07	22
	FC183_g6	F-type pumice RD	66.83	15.96	0.76	4.56	0.20	0.71	2.44	5.35	2.23	0.14	0.26	99.43	22
	FC183_g7	F-type pumice RD	67.49	15.35	0.80	5.69	0.24	0.87	2.90	5.19	2.22	0.17	0.29	101.22	21
	FC183_g7	F-type pumice RD	67.15	15.53	0.74	5.79	0.22	0.86	3.05	5.74	2.27	0.19	0.23	101.77	21
	FC183_g8	F-type pumice RD	66.57	15.62	0.68	5.21	0.20	0.81	2.88	5.01	2.24	0.14	0.22	99.60	22
	FC183_g8	F-type pumice RD	67.04	15.91	0.83	5.20	0.23	0.88	2.76	5.68	2.28	0.14	0.26	101.21	23
	FC183_g8	F-type pumice RD	66.97	15.78	0.75	5.22	0.25	0.87	2.98	5.37	2.18	0.15	0.26	100.78	23
	FC183_g9	F-type pumice RD	67.44	15.45	0.74	5.28	0.24	0.87	2.90	4.58	2.25	0.15	0.25	100.15	23
	FC183_g9	F-type pumice RD	66.22	15.39	0.66	5.11	0.18	0.79	2.50	6.25	2.29	0.12	0.25	99.77	22
	FC183_g9	F-type pumice RD	67.61	15.55	0.64	5.31	0.22	0.82	2.94	5.54	2.25	0.15	0.27	101.31	22
15S-PS-2i	PS-2l_g1	S-type lapilli-sized RD	69.30	15.37	0.64	4.40	0.18	0.62	2.33	5.97	2.35	0.20	0.20	101.57	20
	PS-2l_g1	S-type lapilli-sized RD	68.79	15.42	0.50	4.24	0.22	0.57	2.23	5.24	2.42	0.18	0.19	100.01	19
	PS-2l_g1	S-type lapilli-sized RD	68.53	14.95	0.55	4.25	0.19	0.65	2.21	5.85	2.37	0.20	0.18	99.92	21
	PS-2l_g2	S-type lapilli-sized RD	66.70	15.16	0.58	5.41	0.18	0.96	2.41	5.74	2.25	0.14	0.21	99.73	24
	PS-2l_g3	S-type lapilli-sized RD	67.59	16.03	0.63	4.33	0.20	0.58	2.42	5.23	2.34	0.14	0.21	99.70	19
	PS-2l_g4	S-type lapilli-sized RD	68.16	14.82	0.60	4.66	0.22	0.63	1.98	5.55	2.63	0.19	0.18	99.63	19

Sample	Analysis ID	Description	SiO_2	Al_2O_3	TiO_2	FeOt	MnO	MgO	CaO	Na_2O	K_2O	Cl	P_2O_5	Total	Mg #
15S-PS-2i	PS-2l_g5	S-type lapilli-sized RD	69.37	15.53	0.65	4.52	0.20	0.59	2.03	5.87	2.55	0.15	0.18	101.62	19
	PS-2l_g7	S-type lapilli-sized RD	69.28	15.10	0.58	4.46	0.19	0.67	2.22	5.89	2.45	0.19	0.21	101.26	21
	PS-2l_g8	S-type lapilli-sized RD	68.29	15.36	0.68	4.33	0.21	0.63	2.18	5.50	2.42	0.16	0.19	99.96	21
	PS-2l_g9	S-type lapilli-sized RD	68.73	15.44	0.62	4.38	0.23	0.64	2.41	5.96	2.44	0.15	0.18	101.19	21
	PS-2l_g11	S-type lapilli-sized RD	68.20	15.31	0.62	4.59	0.20	0.66	2.29	5.87	2.44	0.19	0.19	100.56	20
	PS-2l_g12	S-type lapilli-sized RD	68.95	14.64	0.61	4.29	0.21	0.58	2.12	6.48	2.45	0.17	0.21	100.70	19
	PS-2l_g12	S-type lapilli-sized RD	68.82	15.26	0.63	4.12	0.19	0.57	2.25	5.94	2.40	0.18	0.16	100.52	20
	PS-2l_g13	S-type lapilli-sized RD	68.58	15.15	0.58	4.35	0.20	0.53	2.02	5.32	2.51	0.16	0.15	99.54	18
	PS-2l_g13	S-type lapilli-sized RD	67.81	15.25	0.64	4.09	0.20	0.57	2.19	6.07	2.51	0.17	0.19	99.68	20
	PS-2l_g14	S-type lapilli-sized RD	69.13	15.24	0.54	4.22	0.20	0.49	2.03	5.88	2.44	0.18	0.19	100.54	17
	PS-2l_g14	S-type lapilli-sized RD	69.02	15.70	0.54	4.24	0.20	0.48	2.12	6.44	2.50	0.18	0.14	101.56	17
	PS-2l_g14	S-type lapilli-sized RD	69.89	15.13	0.52	4.21	0.21	0.45	1.91	5.82	2.46	0.16	0.15	100.91	16
	PS-2l_g15	S-type lapilli-sized RD	68.75	15.88	0.65	4.30	0.19	0.64	2.22	6.75	2.45	0.14	0.20	102.17	21
	PS-2l_g15	S-type lapilli-sized RD	68.85	15.57	0.66	4.31	0.19	0.62	2.37	6.14	2.44	0.15	0.20	101.49	21
	PS-2l_g15	S-type lapilli-sized RD	67.89	15.67	0.58	4.09	0.20	0.59	2.19	6.09	2.46	0.14	0.24	100.16	21
	PS-2l_g16	S-type lapilli-sized RD	68.04	15.42	0.64	4.56	0.21	0.71	2.52	6.34	2.31	0.18	0.23	101.18	22
	PS-2l_g16	S-type lapilli-sized RD	69.17	15.76	0.71	4.33	0.20	0.65	2.33	5.48	2.28	0.15	0.19	101.26	21
	PS-2l_g16	S-type lapilli-sized RD	68.10	15.03	0.60	4.42	0.23	0.76	2.55	5.90	2.38	0.20	0.22	100.39	23
	PS-2l_g17	S-type lapilli-sized RD	69.52	15.46	0.65	4.47	0.21	0.55	2.14	5.57	2.43	0.17	0.15	101.31	18
	PS-2l_g17	S-type lapilli-sized RD	67.83	14.75	0.56	5.33	0.27	1.25	2.48	6.57	2.38	0.18	0.16	101.75	30
	PS-2l_g18	S-type lapilli-sized RD	67.10	15.54	0.54	4.14	0.21	0.60	2.34	5.22	2.58	0.15	0.16	98.58	21
	PS-2l_g18	S-type lapilli-sized RD	69.33	15.15	0.64	4.24	0.20	0.47	1.98	6.26	2.52	0.17	0.16	101.11	17
	PS-2l_g18	S-type lapilli-sized RD	68.10	15.41	0.58	4.68	0.19	0.58	2.38	5.61	2.37	0.20	0.18	100.29	18
	PS-2l_g19	S-type lapilli-sized RD	67.95	15.57	0.71	4.44	0.17	0.60	2.16	6.85	2.51	0.17	0.20	101.33	20
FC-175c*	175C_10	S-type lapilli-sized RD	65.76	15.02	0.53	4.18	0.16	0.63	2.31	5.24	2.32	0.12	0.09	96.35	21
	175C_11	S-type lapilli-sized RD	65.88	14.66	0.47	4.17	0.22	0.60	2.25	5.56	2.44	0.17	0.13	96.54	20
	175C_12	S-type lapilli-sized RD	65.50	14.73	0.65	4.04	0.20	0.59	2.15	5.31	2.40	0.16	0.08	95.82	21
	175C_13	S-type lapilli-sized RD	65.95	14.94	0.49	4.07	0.16	0.65	2.24	5.27	2.38	0.21	0.25	96.62	22
	175C_15	S-type lapilli-sized RD	64.34	14.59	0.48	4.24	0.19	0.54	2.20	4.99	2.28	0.18	0.14	94.18	19
	175C_16	S-type lapilli-sized RD	65.52	14.95	0.53	4.15	0.20	0.61	2.25	5.11	2.42	0.14	0.19	96.06	21
	175C_17	S-type lapilli-sized RD	65.02	14.86	0.61	4.19	0.13	0.67	2.37	5.10	2.32	0.12	0.18	95.58	22
	175C_18	S-type lapilli-sized RD	65.30	14.78	0.49	4.04	0.18	0.54	2.28	4.94	2.43	0.15	0.14	95.27	19
	175C_19	S-type lapilli-sized RD	66.66	14.92	0.57	4.30	0.19	0.61	2.34	5.65	2.29	0.18	0.18	97.90	20
	175C_20	S-type lapilli-sized RD	66.87	15.05	0.59	4.25	0.23	0.63	2.25	5.62	2.46	0.15	0.18	98.28	21
	175C_21	S-type lapilli-sized RD	66.08	14.62	0.66	3.94	0.20	0.61	2.34	5.13	2.31	0.15	0.13	96.17	22
	175C_24	S-type lapilli-sized RD	66.08	14.94	0.55	4.22	0.21	0.67	2.23	5.20	2.38	0.17	0.15	96.80	22
	175C_25	S-type lapilli-sized RD	65.83	14.90	0.55	4.19	0.31	0.65	2.26	5.24	2.38	0.13	0.17	96.61	22
	175C_26	S-type lapilli-sized RD	65.93	14.77	0.55	4.26	0.27	0.69	2.30	5.21	2.53	0.16	0.25	96.91	22
	175C_27	S-type lapilli-sized RD	66.37	15.11	0.60	3.91	0.24	0.69	2.33	5.49	2.50	0.14	0.18	97.57	24
	175C_28	S-type lapilli-sized RD	65.68	14.87	0.38	4.46	0.14	0.65	2.27	5.24	2.32	0.13	0.16	96.30	21
	175C_32	S-type lapilli-sized RD	66.39	14.99	0.49	4.34	0.21	0.52	2.21	5.54	2.35	0.14	0.08	97.27	18
	175C_33	S-type lapilli-sized RD	66.64	15.07	0.43	4.28	0.20	0.64	2.21	5.48	2.41	0.15	0.12	97.63	21
	175C_34	S-type lapilli-sized RD	66.39	15.11	0.51	4.24	0.19	0.59	2.42	5.10	2.46	0.17	0.08	97.26	20
	175C_35	S-type lapilli-sized RD	66.34	14.93	0.57	4.21	0.25	0.60	2.50	5.13	2.45	0.16	0.08	97.22	20
	175C_37	S-type lapilli-sized RD	66.44	15.12	0.47	4.22	0.16	0.64	2.23	5.16	2.48	0.12	0.14	97.17	21
	175C_38	S-type lapilli-sized RD	66.24	14.72	0.56	4.34	0.21	0.62	2.34	5.42	2.49	0.16	0.16	97.26	20
	175C_39	S-type lapilli-sized RD	66.25	14.67	0.55	4.11	0.24	0.67	2.24	5.53	2.38	0.19	0.18	97.01	23
FC-175b*	175B_53	S-type lapilli-sized RD	63.83	14.68	0.42	4.14	0.18	0.61	2.48	4.70	2.19	0.16	0.23	93.61	21
	175B_55	S-type lapilli-sized RD	64.41	14.95	0.48	4.34	0.22	0.67	2.35	4.75	2.30	0.20	0.16	94.84	22
	175B_57	S-type lapilli-sized RD	64.96	14.77	0.45	4.08	0.23	0.57	2.25	4.81	2.38	0.16	0.15	94.80	20
	175B_58	S-type lapilli-sized RD	66.61	15.28	0.45	4.33	0.11	0.59	2.23	5.13	2.44	0.18	0.15	97.52	20

Sample	Analysis ID	Description	SiO_2	Al_2O_3	TiO_2	FeOt	MnO	MgO	CaO	Na_2O	K_2O	Cl	P_2O_5	Total	Mg #
FC-175b*	175B_59	S-type lapilli-sized RD	65.81	14.84	0.57	4.27	0.15	0.58	2.18	5.02	2.36	0.20	0.15	96.13	20
	175B_60	S-type lapilli-sized RD	66.45	14.98	0.52	4.27	0.15	0.54	2.01	5.40	2.32	0.12	0.13	96.89	18
	175B_62	S-type lapilli-sized RD	65.62	14.75	0.48	3.84	0.21	0.54	2.23	4.99	2.59	0.19	0.11	95.55	20
	175B_63	S-type lapilli-sized RD	66.51	14.78	0.53	4.24	0.20	0.57	2.29	5.08	2.36	0.17	0.15	96.87	19
	175B_64	S-type lapilli-sized RD	66.69	15.11	0.48	4.00	0.18	0.55	2.09	5.51	2.45	0.10	0.16	97.31	20
	175B_65	S-type lapilli-sized RD	67.14	15.23	0.45	4.27	0.21	0.62	2.36	5.27	2.48	0.13	0.20	98.36	21
	175B_66	S-type lapilli-sized RD	67.75	15.23	0.40	4.05	0.18	0.51	2.18	5.28	2.58	0.09	0.18	98.43	18
	175B_67	S-type lapilli-sized RD	66.89	15.40	0.46	4.41	0.22	0.66	2.27	5.24	2.59	0.19	0.21	98.57	21
	175B_68	S-type lapilli-sized RD	65.70	15.18	0.54	4.35	0.21	0.62	2.33	5.53	2.40	0.14	0.17	97.18	20
	175B_69	S-type lapilli-sized RD	65.58	14.94	0.38	4.24	0.17	0.53	1.97	5.14	2.53	0.16	0.15	95.79	18
	175B_70	S-type lapilli-sized RD	65.97	15.17	0.45	4.10	0.27	0.45	1.99	5.08	2.43	0.18	0.09	96.17	16
	175B_71	S-type lapilli-sized RD	66.09	14.82	0.43	4.08	0.27	0.51	2.10	5.31	2.31	0.15	0.14	96.22	18
	175B_72	S-type lapilli-sized RD	66.72	15.06	0.45	4.24	0.25	0.53	2.11	5.33	2.54	0.19	0.18	97.61	18
	175B_73	S-type lapilli-sized RD	67.49	15.20	0.49	4.31	0.23	0.54	2.13	5.11	2.65	0.16	0.14	98.46	18
	175B_74	S-type lapilli-sized RD	66.14	15.02	0.37	4.17	0.24	0.54	2.20	5.21	2.54	0.14	0.17	96.73	19
	175B_75	S-type lapilli-sized RD	66.20	14.89	0.37	3.85	0.18	0.52	2.12	5.43	2.37	0.14	0.15	96.23	19
	175B_76	S-type lapilli-sized RD	65.40	15.01	0.59	4.49	0.22	0.55	2.33	5.42	2.52	0.18	0.10	96.80	18
	175B_77	S-type lapilli-sized RD	67.01	15.10	0.49	4.46	0.20	0.59	2.26	5.28	2.64	0.17	0.11	98.30	19
	175B_78	S-type lapilli-sized RD	66.46	15.26	0.56	4.47	0.24	0.56	2.27	5.51	2.49	0.14	0.08	98.05	18
FC-06c*	06c_88	F-type pumice RD	68.45	15.27	0.46	4.11	0.14	0.50	2.18	5.34	2.44	0.20	0.12	99.20	18
	06c_89	F-type pumice RD	67.78	15.12	0.49	4.17	0.15	0.47	2.02	5.07	2.54	0.19	0.12	98.10	17
	06c_90	F-type pumice RD	67.34	15.07	0.45	3.95	0.15	0.48	2.09	5.17	2.42	0.18	0.11	97.41	18
	06c_91	F-type pumice RD	68.93	15.12	0.45	4.12	0.24	0.52	2.35	5.47	2.41	0.20	0.08	99.89	18
	06c_92	F-type pumice RD	69.37	14.71	0.51	4.18	0.19	0.49	2.02	5.50	2.55	0.17	0.02	99.72	17
	06c_93	F-type pumice RD	67.44	14.95	0.46	3.96	0.19	0.49	2.23	5.59	2.51	0.17	0.07	98.06	18
	06c_94	F-type pumice RD	69.11	15.21	0.51	4.20	0.27	0.52	2.19	5.50	2.59	0.16	0.08	100.31	18
	06c_95	F-type pumice RD	68.89	15.08	0.46	4.26	0.19	0.47	2.10	5.94	2.37	0.17	0.09	100.02	17
	06c_96	F-type pumice RD	69.13	15.21	0.49	4.21	0.27	0.48	2.15	5.26	2.51	0.16	0.11	99.97	17
	06c_97	F-type pumice RD	69.29	15.25	0.39	4.01	0.19	0.54	2.30	3.47	2.44	0.20	0.15	98.21	19
	06c_100	F-type pumice RD	66.59	15.04	0.43	3.92	0.22	0.51	2.12	5.24	2.50	0.19	0.09	96.84	19
	06c_101	F-type pumice RD	68.02	15.24	0.44	3.81	0.14	0.50	2.01	5.16	2.53	0.14	0.11	98.10	19
	06c_102	F-type pumice RD	65.87	15.03	0.50	3.93	0.20	0.43	2.14	5.50	2.29	0.15	0.09	96.14	16
	06c_103	F-type pumice RD	67.95	15.11	0.48	3.98	0.22	0.44	2.14	5.28	2.56	0.24	0.08	98.49	16
	06c_104	F-type pumice RD	67.40	15.05	0.44	4.33	0.22	0.43	2.00	5.19	2.39	0.21	0.11	97.77	15
	06c_105	F-type pumice RD	67.70	14.91	0.50	3.90	0.16	0.52	2.16	5.53	2.52	0.21	0.10	98.22	19
	06c_106	F-type pumice RD	66.76	15.41	0.47	3.86	0.18	0.48	2.12	5.50	2.37	0.16	0.06	97.37	18
	06c_111	F-type pumice RD	67.84	14.97	0.46	3.74	0.18	0.49	2.08	5.45	2.56	0.17	0.12	98.06	19
	06c_112	F-type pumice RD	65.85	14.60	0.57	3.79	0.27	0.47	2.06	5.46	2.27	0.14	0.13	95.60	18
	06c_113	F-type pumice RD	65.42	14.52	0.47	4.07	0.31	0.47	2.17	5.04	2.44	0.17	0.20	95.28	17
	06c_114	F-type pumice RD	65.61	14.79	0.51	4.16	0.26	0.49	1.90	5.20	2.47	0.12	0.17	95.68	17
	06c_115	F-type pumice RD	67.18	15.30	0.53	4.01	0.19	0.50	2.13	5.46	2.53	0.18	0.14	98.16	18
	06c_116	F-type pumice RD	66.28	15.01	0.44	4.21	0.19	0.50	2.27	5.20	2.49	0.15	0.15	96.89	18
	06c_117	F-type pumice RD	67.74	15.17	0.49	4.03	0.22	0.50	2.04	5.34	2.52	0.18	0.10	98.33	18
	06c_118	F-type pumice RD	67.34	15.22	0.46	4.04	0.14	0.48	2.14	5.62	2.41	0.15	0.14	98.14	17
	06c_119	F-type pumice RD	66.00	14.60	0.55	3.85	0.16	0.46	2.10	4.96	2.35	0.17	0.12	95.34	18
97S-PS-34a*	34a_130	S-type pumice RD	67.78	15.41	0.53	4.32	0.19	0.69	2.40	5.26	2.46	0.13	0.16	99.32	22
	34a_131	S-type pumice RD	68.43	15.16	0.53	4.44	0.27	0.65	2.48	5.32	2.58	0.17	0.15	100.18	21
	34a_134	S-type pumice RD	67.16	15.00	0.53	3.98	0.31	0.64	2.40	5.06	2.45	0.12	0.12	97.79	22
	34a_135	S-type pumice RD	66.64	15.13	0.55	4.36	0.29	0.63	2.36	5.27	2.42	0.12	0.15	97.92	20
	34a_136	S-type pumice RD	68.02	15.27	0.53	4.13	0.21	0.64	2.36	4.84	2.48	0.14	0.18	98.81	22
	34a_138	S-type pumice RD	64.53	14.51	0.49	4.16	0.24	0.62	2.29	4.99	2.28	0.23	0.13	94.47	21

Sample	Analysis ID	Description	SiO_2	Al_2O_3	TiO_2	FeOt	MnO	MgO	CaO	Na_2O	K_2O	Cl	P_2O_5	Total	Mg #
97S-PS-34a*	34a_139	S-type pumice RD	68.18	15.45	0.53	4.49	0.27	0.65	2.47	5.22	2.51	0.19	0.17	100.14	21
	34a_141	S-type pumice RD	63.67	14.00	0.49	4.16	0.24	0.65	2.13	5.15	2.18	0.23	0.13	93.04	22
	34a_142	S-type pumice RD	68.83	15.23	0.55	4.41	0.21	0.68	2.40	5.41	2.48	0.14	0.17	100.51	22
	34a_143	S-type pumice RD	68.35	14.93	0.57	4.40	0.21	0.62	2.45	5.15	2.42	0.20	0.21	99.51	20
	34a_144	S-type pumice RD	68.18	15.03	0.49	4.50	0.20	0.64	2.28	5.23	2.39	0.13	0.20	99.26	20
	34a_145	S-type pumice RD	67.74	15.16	0.52	4.49	0.19	0.62	2.40	5.37	2.38	0.20	0.16	99.23	20
	34a_146	S-type pumice RD	67.49	15.14	0.50	4.37	0.23	0.65	2.40	5.28	2.41	0.18	0.21	98.84	21
	34a_147	S-type pumice RD	68.44	15.03	0.47	4.35	0.23	0.67	2.38	4.91	2.39	0.15	0.09	99.11	22
	34a_148	S-type pumice RD	66.90	15.40	0.64	4.12	0.21	0.65	2.39	5.39	2.45	0.19	0.23	98.57	22
	34a_149	S-type pumice RD	66.41	15.19	0.57	4.46	0.19	0.59	2.39	5.32	2.43	0.18	0.13	97.86	19
	34a_150	S-type pumice RD	67.42	15.14	0.51	4.59	0.22	0.62	2.13	5.11	2.48	0.24	0.16	98.60	19
	34a_151	S-type pumice RD	67.43	14.87	0.61	3.95	0.27	0.62	2.38	4.76	2.43	0.14	0.19	97.65	22
	34a_152	S-type pumice RD	67.75	15.22	0.60	4.10	0.23	0.59	2.33	5.52	2.39	0.16	0.21	99.09	20
	34a_154	S-type pumice RD	68.18	15.38	0.55	4.29	0.25	0.68	2.37	5.25	2.31	0.19	0.24	99.68	22
	34a_155	S-type pumice RD	68.17	15.55	0.61	4.25	0.18	0.66	2.34	5.10	2.52	0.21	0.20	99.78	22
	34a_156	S-type pumice RD	68.20	15.13	0.53	4.06	0.20	0.65	2.41	5.36	2.53	0.17	0.18	99.42	22
	34a_157	S-type pumice RD	67.94	15.09	0.64	4.40	0.17	0.63	2.39	5.13	2.31	0.21	0.17	99.08	20
	34a_158	S-type pumice RD	68.39	14.71	0.60	4.33	0.13	0.65	2.33	5.29	2.40	0.23	0.21	99.26	21
	34a_160	S-type pumice RD	68.55	15.09	0.52	4.34	0.30	0.65	2.39	5.08	2.35	0.19	0.11	99.58	21
	34a_161	S-type pumice RD	65.92	14.91	0.63	4.20	0.20	0.60	2.23	5.09	2.29	0.17	0.20	96.44	20
	34a_162	S-type pumice RD	68.74	14.89	0.56	4.26	0.24	0.64	2.46	5.33	2.33	0.15	0.10	99.72	21
	34a_172	S-type pumice RD	66.17	15.26	0.58	4.17	0.23	0.67	2.44	5.45	2.43	0.19	0.15	97.75	22
	34a_173	S-type pumice RD	66.96	15.23	0.57	4.65	0.19	0.64	2.58	5.21	2.35	0.19	0.17	98.73	20
	34a_174	S-type pumice RD	66.30	15.07	0.45	4.41	0.22	0.60	2.49	5.58	2.49	0.20	0.08	97.88	20
	34a_175	S-type pumice RD	66.84	15.43	0.55	4.37	0.16	0.64	2.51	5.39	2.40	0.19	0.22	98.69	21
	34a_176	S-type pumice RD	66.66	14.99	0.47	4.26	0.23	0.62	2.20	5.97	2.39	0.20	0.15	98.14	20
	34a_177	S-type pumice RD	66.80	15.01	0.50	4.57	0.22	0.64	2.30	5.18	2.50	0.18	0.15	98.04	20
	34a_178	S-type pumice RD	67.57	15.34	0.46	4.42	0.25	0.58	2.37	5.10	2.50	0.16	0.10	98.86	19
	34a_179	S-type pumice RD	66.76	15.34	0.52	4.17	0.23	0.62	2.17	5.32	2.52	0.11	0.10	97.87	21
	34a_180	S-type pumice RD	66.61	15.06	0.52	4.23	0.19	0.58	2.26	5.06	2.37	0.18	0.14	97.20	20
	34a_181	S-type pumice RD	66.11	15.25	0.50	4.55	0.22	0.64	2.50	5.32	2.48	0.22	0.16	97.95	20
	34a_182	S-type pumice RD	66.30	15.24	0.56	4.34	0.26	0.59	2.41	5.20	2.40	0.18	0.17	97.64	20
	34a_183	S-type pumice RD	66.94	15.24	0.67	4.14	0.21	0.62	2.62	5.60	2.49	0.19	0.15	98.88	21
	34a_184	S-type pumice RD	67.05	15.15	0.53	4.28	0.17	0.52	2.47	5.36	2.53	0.17	0.22	98.46	18
	34a_185	S-type pumice RD	67.24	15.41	0.48	4.38	0.28	0.63	2.43	5.14	2.42	0.15	0.18	98.74	20
	34a_186	S-type pumice RD	67.10	15.16	0.50	3.85	0.19	0.52	2.07	5.14	2.41	0.15	0.16	97.24	19
	34a_187	S-type pumice RD	66.77	15.24	0.47	4.42	0.25	0.54	2.49	5.44	2.37	0.19	0.19	98.37	18
	34a_188	S-type pumice RD	68.02	15.53	0.55	4.48	0.15	0.65	2.32	5.89	2.47	0.21	0.18	100.44	20
	34a_189	S-type pumice RD	68.78	15.35	0.60	4.32	0.18	0.59	2.44	5.32	2.43	0.20	0.13	100.36	20
	34a_190	S-type pumice RD	68.29	15.11	0.52	4.40	0.19	0.64	2.41	5.33	2.39	0.22	0.13	99.63	20
	34a_191	S-type pumice RD	67.92	15.33	0.48	4.12	0.25	0.60	2.28	5.48	2.38	0.19	0.18	99.20	21
	34a_192	S-type pumice RD	64.11	14.80	0.40	4.05	0.21	0.61	1.90	5.13	2.40	0.09	0.20	93.89	21
	34a_193	S-type pumice RD	66.66	15.38	0.59	4.16	0.29	0.58	2.33	5.03	2.44	0.14	0.17	97.76	20
	34a_194	S-type pumice RD	65.19	15.09	0.53	4.23	0.21	0.65	2.32	5.00	2.43	0.19	0.20	96.06	21
	34a_195	S-type pumice RD	65.59	15.11	0.50	4.63	0.24	0.62	2.67	5.43	2.47	0.22	0.17	97.64	19
	34a_196	S-type pumice RD	66.21	15.34	0.59	4.03	0.22	0.62	2.48	5.20	2.46	0.14	0.18	97.46	21
	34a_197	S-type pumice RD	65.28	14.90	0.45	4.09	0.23	0.59	2.48	5.10	2.45	0.14	0.16	95.87	20
	34a_198	S-type pumice RD	64.62	15.34	0.50	4.05	0.25	0.65	2.49	4.97	2.34	0.14	0.14	95.50	22
	34a_199	S-type pumice RD	65.53	15.51	0.41	4.19	0.25	0.55	2.54	5.07	2.43	0.21	0.19	96.87	19
	34a_200	S-type pumice RD	64.88	15.17	0.51	4.11	0.17	0.65	2.55	5.21	2.41	0.20	0.15	96.01	22
	34a_201	S-type pumice RD	64.53	15.03	0.51	4.02	0.21	0.61	2.29	5.16	2.54	0.19	0.15	95.24	21

Sample	Analysis ID	Description	SiO_2	Al_2O_3	TiO_2	FeOt	MnO	MgO	CaO	Na_2O	K_2O	Cl	P_2O_5	Total	Mg #
97S-PS-34a*	34a_202	S-type pumice RD	65.41	15.36	0.60	4.25	0.28	0.64	2.45	5.18	2.51	0.21	0.12	97.01	21
FC-175d*	175D_220	S-type pumice RD	66.64	15.41	0.37	4.15	0.15	0.57	2.26	5.67	2.41	0.17	0.20	98.01	20
	175D_221	S-type pumice RD	66.85	15.18	0.51	4.37	0.22	0.61	2.38	5.39	2.43	0.17	0.21	98.32	20
	175D_222	S-type pumice RD	66.57	14.86	0.49	4.41	0.22	0.58	2.28	5.11	2.38	0.16	0.19	97.24	19
	175D_223	S-type pumice RD	66.55	15.08	0.42	4.38	0.24	0.63	2.47	5.43	2.31	0.19	0.18	97.88	20
	175D_224	S-type pumice RD	66.77	14.98	0.51	4.16	0.23	0.63	2.27	5.42	2.50	0.15	0.14	97.76	21
	175D_225	S-type pumice RD	66.57	14.97	0.45	4.01	0.16	0.62	2.22	5.39	2.48	0.16	0.10	97.15	22
	175D_226	S-type pumice RD	66.66	15.20	0.52	4.23	0.20	0.64	2.28	5.06	2.45	0.11	0.13	97.48	21
	175D_227	S-type pumice RD	66.74	15.11	0.54	4.42	0.24	0.61	2.34	5.08	2.42	0.16	0.15	97.83	20
	175D_228	S-type pumice RD	66.65	15.11	0.61	4.53	0.21	0.59	2.45	5.35	2.36	0.18	0.20	98.22	19
	175D_229	S-type pumice RD	64.89	14.72	0.52	4.25	0.21	0.63	2.19	4.92	2.30	0.14	0.11	94.88	21
	175D_230	S-type pumice RD	67.68	14.87	0.51	4.37	0.21	0.60	2.28	5.12	2.46	0.14	0.09	98.33	20
	175D_231	S-type pumice RD	67.49	14.99	0.44	4.26	0.20	0.60	2.21	5.37	2.43	0.10	0.12	98.21	20
	175D_232	S-type pumice RD	65.79	15.10	0.50	3.70	0.17	0.55	2.04	5.12	2.36	0.17	0.21	95.70	21
	175D_233	S-type pumice RD	67.43	15.00	0.50	4.08	0.21	0.61	2.30	5.71	2.51	0.17	0.21	98.72	21
	175D_234	S-type pumice RD	67.32	15.17	0.57	4.51	0.23	0.61	2.45	5.12	2.34	0.17	0.20	98.69	20
	175D_235	S-type pumice RD	67.15	15.13	0.54	4.24	0.18	0.61	2.58	5.52	2.38	0.14	0.13	98.59	20
	175D_236	S-type pumice RD	66.98	15.11	0.54	4.52	0.21	0.64	2.49	5.57	2.37	0.16	0.20	98.79	20
	175D_237	S-type pumice RD	66.78	14.96	0.56	4.35	0.18	0.61	2.49	5.01	2.20	0.18	0.17	97.49	20
	175D_238	S-type pumice RD	67.02	15.02	0.43	4.24	0.30	0.62	2.29	5.21	2.42	0.14	0.13	97.82	21
	175D_239	S-type pumice RD	67.41	15.06	0.45	4.29	0.32	0.55	2.48	5.32	2.46	0.20	0.13	98.67	19
	175D_240	S-type pumice RD	67.68	14.86	0.46	4.31	0.26	0.66	2.57	5.17	2.44	0.21	0.12	98.74	21
	175D_241	S-type pumice RD	65.93	15.18	0.47	4.23	0.20	0.58	2.42	5.72	2.40	0.19	0.19	97.51	19
	175D_242	S-type pumice RD	65.69	14.46	0.53	4.14	0.15	0.58	2.42	5.54	2.46	0.17	0.18	96.32	20
	175D_243	S-type pumice RD	66.82	15.42	0.52	4.18	0.23	0.57	2.27	5.66	2.34	0.17	0.14	98.32	20
	175D_244	S-type pumice RD	66.34	14.72	0.57	4.25	0.22	0.61	2.46	5.09	2.48	0.20	0.14	97.08	20
	175D_245	S-type pumice RD	66.21	14.67	0.45	4.41	0.24	0.64	2.32	5.35	2.30	0.15	0.15	96.89	20

Appendix A2. Major element chemistry of glass in basaltic andesite samples.
Abbreviations: S-type = Shishaldin-type, RD = rhyodacite, BA = basaltic andesite
*Glass analyses done by Alaska Volcano Observatory (AVO) at USGS Menlo Park, CA.

Sample	Analysis ID	Description	SiO_2	Al_2O_3	TiO_2	FeOt	MnO	MgO	CaO	Na_2O	K_2O	Cl	P_2O_5	Total	Mg #
97S-PS-34b	34b_g1	Silicic glass in scoria	61.56	15.30	0.89	9.08	0.27	1.75	4.35	3.22	2.53	0.16	0.35	99.47	26
	34b_g2	Silicic glass in scoria	59.66	15.38	1.05	8.97	0.25	1.94	4.61	4.16	2.64	0.12	0.37	99.15	28
	34b_g3	Silicic glass in scoria	66.55	15.17	0.71	4.39	0.11	1.10	2.45	5.74	3.14	0.09	0.17	99.61	31
	34b_g4	Silicic glass in scoria	65.57	14.97	0.59	5.33	0.20	1.21	2.63	5.22	3.03	0.17	0.24	99.17	29
	34b_g5	Silicic glass in scoria	66.92	15.12	0.59	4.87	0.16	1.04	2.64	5.24	3.03	0.14	0.22	99.96	28
	34b_g6	Silicic glass in scoria	67.66	15.24	0.86	5.15	0.13	1.12	2.81	4.10	3.38	0.10	0.23	100.80	28
	34b_g7	Silicic glass in scoria	65.77	15.18	0.94	5.78	0.15	1.54	3.58	4.96	2.91	0.13	0.20	101.13	32
	34b_g8	Silicic glass in scoria	68.79	15.48	0.70	4.07	0.12	0.93	2.55	4.60	3.22	0.09	0.19	100.72	29
	34b_g9	Silicic glass in scoria	63.46	14.54	1.39	6.34	0.19	1.76	4.37	4.17	2.77	0.18	0.33	99.51	33
	34b_g10	Scoria glass	52.71	15.31	2.04	12.44	0.39	3.20	7.33	1.17	1.51	0.25	0.63	96.99	31
	34b_g12	Scoria glass	54.21	15.05	1.80	13.64	0.23	1.86	5.61	2.85	1.52	0.11	0.44	97.33	20
	34b_g11	Scoria glass	53.05	15.48	1.58	10.58	0.23	2.49	6.31	4.85	2.08	0.10	0.43	97.18	30
	34b_g13	Scoria glass --or silicic glass b/c of behavior	56.15	14.65	1.88	10.82	0.27	2.14	5.31	4.34	2.48	0.17	0.45	98.68	26
	34b_g14	Silicic glass in scoria	68.01	15.19	0.68	4.26	0.23	0.74	2.51	5.11	3.25	0.14	0.18	100.30	24
	34b_g15	Silicic glass in scoria	68.30	15.42	0.55	3.87	0.16	0.62	2.59	6.49	3.17	0.17	0.20	101.54	22
	34b_g15	Silicic glass in scoria	68.82	15.62	0.58	4.28	0.19	0.64	2.71	5.81	3.14	0.17	0.18	102.15	21
	34b_g17	Scoria glass --or silicic glass b/c of behavior	57.92	15.73	1.34	8.67	0.22	2.64	4.85	4.54	2.46	0.11	0.35	98.83	35
	34b_g16	Silicic glass in scoria	67.18	15.57	0.80	4.00	0.12	0.73	2.60	3.49	3.57	0.10	0.20	98.36	24
	34Bvp_g1	Silicic glass in scoria	65.56	14.85	0.83	9.27	0.22	0.73	1.58	4.08	2.30	0.12	0.14	99.69	12
	34Bvp_g2	Silicic glass in scoria	59.18	14.90	2.29	14.87	0.27	1.13	1.24	2.64	1.75	0.05	0.30	98.62	12
	34Bvp_g3	Scoria glass	55.58	16.98	1.87	7.62	0.21	2.92	8.45	3.98	0.91	0.03	0.47	99.03	41
	34Bvp_g4	Silicic glass in scoria	65.79	14.47	0.82	5.87	0.22	1.92	4.09	4.51	2.53	0.08	0.22	100.52	37
	34Bvp_g5	Silicic glass in scoria	62.02	14.60	1.02	6.96	0.19	2.33	5.46	4.39	2.10	0.06	0.31	99.44	37
	34Bvp_g6	Silicic glass in scoria	61.64	15.00	1.35	8.38	0.38	2.70	5.54	3.14	1.58	0.13	0.38	100.21	36
15S-PS-2C	15S-PS-2C_g1	Silicic glass in scoria	68.71	15.00	0.58	4.20	0.22	0.62	2.38	4.69	2.45	0.19	0.23	99.28	21
	15S-PS-2C_g3	Silicic glass in scoria	67.85	14.92	0.58	4.65	0.24	0.63	2.26	3.54	2.30	0.19	0.19	97.35	20
	15S-PS-2C_g2	Silicic glass in scoria	65.34	14.88	0.51	4.59	0.23	0.64	2.38	5.58	2.47	0.19	0.20	97.00	20
	15S-PS-2C_g4	Scoria glass	55.26	14.74	1.56	9.26	0.26	3.43	8.00	3.60	1.59	0.11	0.48	98.31	40
	15S-PS-2C_g5	Scoria glass	54.75	15.66	1.42	9.21	0.30	3.71	7.48	3.28	1.77	0.10	0.48	98.14	42
15S-PS-5B	15S-PS-5B_mfgl1	Scoria glass	52.03	13.83	2.03	14.26	0.26	2.89	6.08	3.39	1.98	0.07	0.55	97.37	27
	15S-PS-5B_mfgl2	Scoria glass	53.09	15.05	2.33	12.12	0.40	3.74	8.94	1.04	1.28	0.15	0.51	98.65	35
	15S-PS-5B_mfgl4	Scoria glass	52.68	16.06	1.72	11.95	0.28	3.84	8.53	1.86	1.37	0.08	0.49	98.84	36
	15S-PS-5B_mfgl5	Scoria glass	51.79	16.11	1.62	11.92	0.26	3.79	8.36	1.85	1.28	0.07	0.50	97.56	36
	15S-PS-5B_mfgl6	Scoria glass	52.91	16.65	1.66	10.54	0.27	3.51	8.53	2.86	1.59	0.11	0.48	99.10	37
97S-PS-34b*	34B_385	Shishaldin-type scoria glass	53.95	15.91	1.50	11.52	0.28	3.87	7.23	3.00	1.22	0.11	0.47	99.06	37
	34B_386	Shishaldin-type scoria glass	53.77	15.84	1.48	13.37	0.27	3.27	7.68	2.49	1.15	0.08	0.47	99.89	30
	34B_387	Shishaldin-type scoria glass	52.25	15.67	1.38	11.34	0.27	3.78	7.43	2.91	1.23	0.10	0.40	96.75	37
	34B_388	Shishaldin-type scoria glass	53.39	16.25	1.54	11.25	0.25	3.67	7.79	2.75	1.18	0.07	0.43	98.57	37
	34B_389	Shishaldin-type scoria glass	52.75	15.96	1.33	11.62	0.29	3.51	7.68	3.38	1.31	0.08	0.44	98.34	35
	34B_390	Shishaldin-type scoria glass	52.24	16.05	1.56	11.76	0.24	3.91	7.87	2.74	1.12	0.05	0.47	98.00	37
	34B_391	Shishaldin-type scoria glass	52.17	15.73	1.49	13.13	0.27	3.59	7.78	2.25	1.26	0.08	0.40	98.15	33
	34B_392	Shishaldin-type scoria glass	53.19	15.51	1.64	12.01	0.28	3.79	8.36	2.43	1.20	0.08	0.39	98.89	36
	34B_393	Shishaldin-type scoria glass	53.56	16.04	1.31	11.32	0.22	3.75	8.26	2.65	0.98	0.09	0.44	98.61	37
	34B_394	Shishaldin-type scoria glass	54.21	16.24	1.45	11.85	0.25	3.48	7.40	3.13	0.95	0.10	0.43	99.49	34
	34B_395	Shishaldin-type scoria glass	53.31	15.28	1.47	11.62	0.23	4.23	8.14	2.49	1.12	0.10	0.44	98.44	39
	34B_396	Shishaldin-type scoria glass	53.16	16.02	1.29	11.22	0.24	3.74	7.69	2.97	1.16	0.08	0.37	97.93	37
	34B_397	Shishaldin-type scoria glass	53.46	16.39	1.52	11.71	0.29	3.76	7.58	2.99	1.17	0.09	0.43	99.40	36
	34B_398	Shishaldin-type scoria glass	53.90	16.31	1.53	11.28	0.26	3.70	8.53	3.24	0.87	0.06	0.42	100.10	37
	34B_399	Shishaldin-type scoria glass	52.68	16.01	1.49	11.82	0.29	3.95	8.42	2.38	1.12	0.06	0.44	98.65	37
	34B_400	Shishaldin-type scoria glass	53.40	16.19	1.52	11.90	0.26	3.87	8.13	2.39	1.05	0.06	0.49	99.28	37
	34B_401	Shishaldin-type scoria glass	53.10	16.06	1.60	11.71	0.27	4.03	8.28	2.56	1.10	0.06	0.49	99.27	38
	34B_402	Shishaldin-type scoria glass	53.38	15.93	1.43	11.77	0.22	3.80	8.22	2.49	1.07	0.09	0.52	98.92	37
	34B_403	Shishaldin-type scoria glass	53.57	16.29	1.50	12.12	0.24	3.57	7.53	3.17	1.16	0.11	0.37	99.63	34
	34B_404	Shishaldin-type scoria glass	54.17	16.10	1.48	12.12	0.25	3.63	7.85	2.63	1.17	0.11	0.43	99.95	35
	34B_405	Shishaldin-type scoria glass	53.55	16.04	1.42	11.04	0.26	3.56	7.82	2.89	1.19	0.08	0.44	98.29	36
	34B_406	Shishaldin-type scoria glass	52.66	16.14	1.51	12.07	0.17	3.76	8.03	3.32	0.96	0.11	0.47	99.21	36
	34B_407	Shishaldin-type scoria glass	53.10	15.95	1.43	11.89	0.25	3.73	8.25	3.08	1.15	0.08	0.42	99.33	36
	34B_408	Shishaldin-type scoria glass	53.45	16.27	1.45	10.99	0.24	3.47	7.94	3.46	1.22	0.08	0.47	99.03	36

Appendix A3. Major element chemistry of plagioclase.
Abbreviations: S-type = Shishaldin-type, F-type = Fisher-type, RD = rhyodacite, BA = basaltic andesite, inter. = intermediate, ulv = ulvöspinel, opx = orthopyroxene, ap = apatite, plag = plagioclase, ox = oxide, BSE = backscattered electron; b.d. = below detection; n.a. = not analyzed, MI = melt inclusion
Analyses for 34A, 06c, and 34B are from Stelling (2003), but are included since they were used in plagioclase-liquid hygrometer calculations.
*A crystal found within the basaltic andesite, but is from a silicic magma.

Deposit type	Sample	Location	Description	SiO_2	TiO_2	Al_2O_3	FeOt	MnO	MgO	CaO	Na_2O	K_2O	Cr_2O_3	Total	Ab	Or	An
S-type RD	175_plag1	rim	euhedral, small (~50	58.94	b.d.	26.05	0.38	b.d.	0.04	7.40	7.59	0.32	b.d.	100.74	63.84	1.78	34.38
S-type RD	175_plag2	core	µm), elongate	59.28	0.05	26.25	0.40	b.d.	0.03	7.24	7.46	0.28	b.d.	100.99	64.05	1.59	34.36
S-type RD	175_plag3	rim	euhedral, ~100 µm,	58.84	0.04	25.44	0.41	b.d.	0.04	6.75	7.43	0.34	0.13	99.42	65.28	1.96	32.77
S-type RD	175_plag4	core	elongate	57.03	0.06	25.32	0.46	b.d.	0.04	7.20	6.82	0.26	0.34	97.52	62.15	1.58	36.27
S-type RD	175_plag5	rim	euhedral, large (~750	58.39	b.d.	26.88	0.33	b.d.	0.03	7.91	6.87	0.27	b.d.	100.66	60.18	1.54	38.28
S-type RD	175_plag6	int	µm), tabular	58.20	0.03	26.45	0.31	b.d.	0.04	7.78	6.93	0.28	b.d.	100.02	60.75	1.61	37.65
S-type RD	175_plag7	core		58.86	0.03	26.43	0.33	b.d.	0.04	7.47	6.89	0.28	b.d.	100.34	61.50	1.67	36.83
S-type RD	175_plag8	rim	subhedral, large,	58.33	0.05	26.89	0.38	0.03	0.04	7.91	7.09	0.28	b.d.	101.00	60.87	1.59	37.54
S-type RD	175_plag9	int	contains large MI,	57.97	0.04	26.55	0.32	b.d.	0.04	7.91	6.89	0.26	b.d.	99.98	60.28	1.49	38.23
S-type RD	175_plag10	core	tabular	59.25	b.d.	26.13	0.34	b.d.	0.04	7.16	7.52	0.30	b.d.	100.73	64.43	1.68	33.89
S-type RD	175_plag11	rim	euhedral, large,	58.54	0.06	26.07	0.39	b.d.	0.04	7.44	7.40	0.29	b.d.	100.24	63.26	1.61	35.13
S-type RD	175_plag12	int	elongate	58.81	0.03	26.51	0.31	b.d.	0.03	7.41	7.34	0.30	b.d.	100.73	63.12	1.68	35.20
S-type RD	175_plag13	core		59.65	b.d.	25.71	0.32	b.d.	0.02	6.81	7.16	0.31	b.d.	99.98	64.36	1.83	33.81
S-type RD	5E_plag1	rim	~150 µm, long slender	60.57	0.08	25.98	0.43	b.d.	0.05	7.03	7.27	0.32	b.d.	101.72	63.95	1.88	34.17
S-type RD	5E_plag2	core		59.02	0.06	26.16	0.44	b.d.	0.04	7.30	7.30	0.31	b.d.	100.63	63.30	1.74	34.96
S-type RD	5E_plag3	rim	subhedral, ~80 x 20 µm, elongate	58.99	0.03	25.73	0.41	b.d.	0.04	6.97	7.53	0.32	b.d.	100.01	64.97	1.82	33.21
S-type RD	5E_plag4	rim	euhedral, ~100µm,	59.10	0.05	25.95	0.43	b.d.	0.04	7.16	7.05	0.32	b.d.	100.09	62.88	1.85	35.27
S-type RD	5E_plag5	core	elongate	59.80	0.03	25.48	0.34	b.d.	0.03	6.46	7.57	0.33	b.d.	100.06	66.64	1.93	31.43
S-type RD	5E_plag6	rim	euhderal, ~50µm long	59.41	0.03	25.58	0.41	b.d.	0.04	6.74	7.33	0.34	b.d.	99.89	65.01	1.99	33.00
S-type RD	5E_plag7	core		58.23	0.05	25.58	0.44	b.d.	0.05	7.19	6.61	0.27	b.d.	98.42	61.40	1.67	36.93
S-type RD	5E_plag8	rim	subhedral, attached to	59.98	b.d.	25.37	0.37	b.d.	0.03	6.38	7.89	0.34	b.d.	100.37	67.79	1.91	30.30
S-type RD	5E_plag9	core	opx, ~200 µm long	58.52	b.d.	26.59	0.38	b.d.	0.03	7.83	7.24	0.28	b.d.	100.87	61.61	1.55	36.84
S-type RD	2I_plag1	rim	euhedral, elongate	58.84	0.03	25.86	0.38	b.d.	0.03	7.20	7.36	0.28	b.d.	99.98	63.87	1.61	34.53
S-type RD	2I_plag2	core		58.15	0.03	24.95	0.29	b.d.	0.04	6.93	7.54	0.30	b.d.	98.24	65.17	1.71	33.12
S-type RD	2I_plag3	rim	subhedral, associated	57.35	b.d.	26.20	0.42	b.d.	0.04	7.73	7.05	0.25	b.d.	99.04	61.39	1.41	37.19
S-type RD	2I_plag4	core	glass contains	57.40	0.03	25.88	0.39	b.d.	0.04	7.56	7.31	0.24	b.d.	98.85	62.76	1.37	35.87
S-type RD	2I_plag5	rim	subhedral, elongate,	57.53	0.04	26.21	0.35	b.d.	0.03	7.84	6.88	0.23	b.d.	99.11	60.58	1.31	38.11
S-type RD	2I_plag6	core	fragmented end	58.41	0.05	26.07	0.34	b.d.	0.04	7.40	7.28	0.29	b.d.	99.88	62.96	1.64	35.40
S-type RD	2I_plag7	rim	euhedral, elongate	57.99	0.04	26.45	0.41	b.d.	0.05	7.79	7.07	0.27	b.d.	100.07	61.18	1.52	37.30
S-type RD	2I_plag8	core		57.09	0.04	26.56	0.35	b.d.	0.04	8.00	6.84	0.25	b.d.	99.17	59.89	1.43	38.68
S-type RD	2I_plag9	rim	euhedral, elongate	57.98	b.d.	26.35	0.43	b.d.	0.03	7.82	7.06	0.24	b.d.	99.91	61.21	1.35	37.44
S-type RD	2I_plag10	core		59.81	0.03	25.27	0.30	b.d.	0.03	6.57	7.71	0.32	b.d.	100.04	66.74	1.82	31.45
S-type RD	2I_plag11	rim	part of px-ulv cluster;	58.01	0.03	26.02	0.37	b.d.	0.04	7.56	7.11	0.25	b.d.	99.39	62.06	1.45	36.49
S-type RD	2I_plag12	core	fragmented; equant	57.94	0.04	26.00	0.37	b.d.	0.03	7.49	7.15	0.26	b.d.	99.29	62.41	1.47	36.13
S-type RD	2I_plag14	core	subhedral (fragmented), elongate	58.33	0.04	26.02	0.34	b.d.	0.05	7.53	7.24	0.25	b.d.	99.79	62.62	1.40	35.98
S-type RD	2I_plag15	rim	subhedral	58.61	0.06	25.93	0.45	b.d.	0.05	7.09	7.43	0.28	b.d.	99.89	64.41	1.60	33.98
S-type RD	2I_plag16	core		61.07	0.04	24.17	0.34	b.d.	0.03	5.50	8.25	0.38	b.d.	99.79	71.49	2.17	26.34
S-type RD	177B_plag1	rim	strong zoning from	58.98	b.d.	25.09	0.42	b.d.	0.04	6.81	7.32	0.32	b.d.	98.98	64.80	1.86	33.34
S-type RD	177B_plag2	core	dark rim to bright core	53.56	0.07	28.97	0.65	b.d.	0.12	10.97	5.13	0.10	b.d.	99.57	45.54	0.61	53.85
S-type RD	177B_plag3	rim	euhedral, elongate,	58.28	b.d.	25.79	0.37	b.d.	0.05	7.38	7.28	0.26	b.d.	99.42	63.15	1.51	35.34
S-type RD	177B_plag4	int	contains large MI	59.10	b.d.	25.58	0.32	b.d.	0.04	6.84	7.36	0.31	b.d.	99.55	64.90	1.79	33.31
S-type RD	177B_plag5	core		59.29	0.03	25.88	0.27	b.d.	0.04	7.04	7.40	0.31	b.d.	100.26	64.40	1.76	33.84
S-type RD	177B_plag7	rim	thin and elongate	58.83	0.08	26.20	0.35	b.d.	0.03	7.33	7.34	0.28	b.d.	100.44	63.40	1.59	35.01
S-type RD	177B_plag8	rim	euhedral, equant, large,	58.05	0.03	26.50	0.45	b.d.	0.05	8.04	6.86	0.25	b.d.	100.21	59.83	1.42	38.75
S-type RD	177B_plag9	int	slight BSE zoning	58.73	0.03	26.15	0.28	b.d.	0.04	7.66	7.08	0.28	b.d.	100.27	61.56	1.62	36.82
S-type RD	177B_plag10	core		59.83	0.03	25.28	0.29	b.d.	0.03	6.49	7.82	0.34	b.d.	100.10	67.22	1.92	30.85

Deposit type	Sample	Location	Description	SiO_2	TiO_2	Al_2O_3	FeOt	MnO	MgO	CaO	Na_2O	K_2O	Cr_2O_3	Total	Ab	Or	An
S-type RD	34a_UN57_0	core	small, good condition	57.63	n.a.	26.62	0.42	n.a.	n.a.	8.19	7.12	0.14	n.a.	100.12	60.64	0.81	38.56
S-type RD	34a_UN57_385	rim		58.80	n.a.	25.85	0.38	n.a.	n.a.	7.09	7.31	0.33	n.a.	99.76	63.86	1.90	34.24
S-type RD	34a_UN58_0	core	tiny, good condition	59.78	n.a.	25.84	0.29	n.a.	n.a.	7.50	7.31	0.39	n.a.	101.12	62.42	2.20	35.37
S-type RD	34a_UN58_121	rim		58.99	n.a.	25.49	0.29	n.a.	n.a.	7.28	7.01	0.36	n.a.	99.43	62.21	2.11	35.68
S-type RD	34a_UN60_0	core	medium, good	57.34	n.a.	26.12	0.43	n.a.	n.a.	7.97	6.76	0.24	n.a.	98.86	59.71	1.38	38.91
S-type RD	34a_UN60_308	rim	condition	58.72	n.a.	26.22	0.34	n.a.	n.a.	7.92	7.04	0.29	n.a.	100.54	60.68	1.64	37.68
S-type RD	34a_UN61_0	core	large, good condition	60.34	n.a.	25.49	0.40	n.a.	n.a.	6.41	7.93	0.30	n.a.	100.87	67.96	1.69	30.34
S-type RD	34a_UN61_384	rim		57.62	n.a.	26.18	0.35	n.a.	n.a.	7.72	6.96	0.25	n.a.	99.07	61.13	1.43	37.44
S-type RD	34a_UN62_0	core	tiny, good condition	57.90	n.a.	26.46	0.44	n.a.	n.a.	8.30	6.75	0.19	n.a.	100.03	58.88	1.06	40.06
S-type RD	34a_UN62_64	rim		59.60	n.a.	24.92	0.40	n.a.	n.a.	5.81	7.71	1.22	n.a.	99.66	65.78	6.86	27.37
S-type RD	34a_UN63_0	core	tiny, good condition	59.11	n.a.	26.35	0.34	n.a.	n.a.	7.56	7.34	0.31	n.a.	101.01	62.60	1.74	35.66
S-type RD	34a_UN63_81	rim		59.11	n.a.	25.52	0.51	n.a.	n.a.	6.52	7.78	0.21	n.a.	99.64	67.55	1.18	31.26
S-type RD	34a_UN64_0	core	small shard, good	59.16	n.a.	26.36	0.44	n.a.	n.a.	7.50	7.04	0.23	n.a.	100.74	62.12	1.32	36.57
S-type RD	34a_UN64_	rim	condition	57.38	n.a.	26.35	0.28	n.a.	n.a.	7.57	6.93	0.24	n.a.	98.75	61.49	1.38	37.13
S-type RD	34a_UN65_0	core	large shard, good	59.33	n.a.	26.42	0.46	n.a.	n.a.	7.41	7.21	0.37	n.a.	101.20	62.42	2.12	35.46
S-type RD	34a_UN65_	rim	condition	59.39	n.a.	26.45	0.40	n.a.	n.a.	7.61	7.12	0.43	n.a.	101.39	61.31	2.46	36.23
S-type RD	34a_UN65_	rim	first of 2 in t-	59.60	n.a.	26.18	0.32	n.a.	n.a.	7.27	7.38	0.21	n.a.	100.95	63.97	1.18	34.85
S-type RD	34a_UN65_	rim	intersection, good	58.25	n.a.	25.66	0.37	n.a.	n.a.	7.27	6.96	0.40	n.a.	98.92	61.91	2.36	35.73
S-type RD	34a_UN66_0	core	second of 2 in t-	59.48	n.a.	25.84	0.36	n.a.	n.a.	6.75	7.57	0.22	n.a.	100.23	66.15	1.25	32.60
S-type RD	34a_UN66_	rim	intersection, good	58.53	n.a.	26.44	0.33	n.a.	n.a.	7.54	7.39	0.33	n.a.	100.56	62.78	1.85	35.38
S-type RD	34a_UN67_	core	broken but good	59.87	n.a.	25.51	0.29	n.a.	n.a.	6.34	7.78	0.52	n.a.	100.32	66.93	2.93	30.14
S-type RD	34a_UN67_	rim	condition	58.80	n.a.	26.67	0.43	n.a.	n.a.	7.60	7.23	0.27	n.a.	101.00	62.29	1.52	36.19
S-type RD	34a_UN68_0	core	broken but good	58.96	n.a.	26.95	0.33	n.a.	n.a.	7.72	7.22	0.29	n.a.	101.45	61.83	1.63	36.54
S-type RD	34a_UN68_	rim	condition	59.11	n.a.	26.44	0.35	n.a.	n.a.	7.08	7.12	0.00	n.a.	100.11	64.56	0.00	35.44
S-type RD	34a_UN69_0	core	small, good condition	55.74	n.a.	27.94	0.74	n.a.	n.a.	9.96	5.28	0.51	n.a.	100.17	47.48	3.03	49.49
S-type RD	34a_UN70_0	core	tiny, good condition	51.44	n.a.	30.65	1.15	n.a.	n.a.	12.91	3.85	0.42	n.a.	100.42	34.17	2.44	63.39
S-type RD	34a_UN71_	rim	tiny, good condition	55.92	n.a.	27.83	0.99	n.a.	n.a.	9.69	5.67	0.74	n.a.	100.84	49.27	4.22	46.51
S-type RD	34a_UN76_0	core	small shard, good	49.35	n.a.	32.37	0.63	n.a.	n.a.	14.36	3.17	0.13	n.a.	100.01	28.30	0.77	70.93
S-type RD	34a_UN76_	rim	condition	48.80	n.a.	32.94	0.61	n.a.	n.a.	14.95	2.91	0.21	n.a.	100.42	25.74	1.24	73.02
S-type RD	34a_UN77_0	core	large shard, good condition	57.12	n.a.	25.90	1.25	n.a.	n.a.	8.84	5.74	0.99	n.a.	99.84	50.92	5.76	43.33
S-type RD	34a_UN77_	rim	1st of 2 in t-intersection, good condition	46.34	n.a.	33.94	0.49	n.a.	n.a.	16.42	1.77	0.07	n.a.	99.02	16.24	0.43	83.33
S-type RD	34a_UN78_0	core	2nd of 2 in t-intersection, good condition	49.78	n.a.	32.40	0.58	n.a.	n.a.	14.52	3.18	0.16	n.a.	100.61	28.12	0.94	70.94
S-type RD	34a_UN80_0	core	broken but good condition	59.59	n.a.	22.14	3.00	n.a.	n.a.	5.99	5.39	2.60	n.a.	98.72	51.79	16.42	31.79
S-type BA	5B_plag1*	rim	subhedral, slightly	58.67	b.d.	25.24	0.40	b.d.	0.04	6.72	7.69	0.32	b.d.	99.09	66.21	1.83	31.96
S-type BA	5B_plag2*	int	rounded, microlites	58.99	b.d.	25.85	0.39	b.d.	0.03	7.13	7.44	0.28	b.d.	100.12	64.30	1.61	34.08
S-type BA	5B_plag3*	core	surround xtl	57.28	0.05	26.95	0.42	b.d.	0.03	8.37	6.75	0.24	b.d.	100.08	58.56	1.35	40.09
S-type BA	2C_plag1	rim	euhedral, small, equant, microlites up to xtl rim	52.43	0.05	29.53	1.08	b.d.	0.20	12.22	4.56	0.12	b.d.	100.18	40.04	0.67	59.30
S-type BA	2C_plag2	int		51.21	0.06	29.14	0.68	0.03	0.12	11.84	4.80	0.11	b.d.	97.98	42.08	0.62	57.29
S-type BA	2C_plag3	core		52.08	0.07	29.60	0.63	b.d.	0.10	12.15	4.40	0.11	b.d.	99.15	39.30	0.67	60.03
S-type BA	34B_UN81_0c	core	small	59.07	n.a.	25.91	0.53	n.a.	n.a.	7.06	7.58	0.45	n.a.	100.61	64.33	2.54	33.13
S-type BA	34B_UN81_83r	rim		60.84	n.a.	24.05	1.16	n.a.	n.a.	6.37	6.83	0.84	n.a.	100.10	62.66	5.06	32.28
S-type BA	34B_UN82_0c	core	small	58.09	n.a.	26.47	0.63	n.a.	n.a.	7.56	7.10	0.24	n.a.	100.09	62.08	1.37	36.55
S-type BA	34B_UN82_57r	rim		59.13	n.a.	26.20	0.46	n.a.	n.a.	7.40	7.27	0.31	n.a.	100.77	62.86	1.76	35.38
S-type BA	34B_UN83_0c	core		59.67	n.a.	25.94	0.35	n.a.	n.a.	6.99	7.49	0.39	n.a.	100.85	64.50	2.23	33.28
S-type BA	34B_UN83_635m	int	huge	58.67	n.a.	26.01	0.35	n.a.	n.a.	7.00	7.29	0.61	n.a.	99.94	63.05	3.47	33.48
S-type BA	34B_UN83_957r	rim		59.47	n.a.	25.87	0.32	n.a.	n.a.	6.78	7.40	0.42	n.a.	100.25	64.76	2.44	32.79
S-type BA	34B_UN86_0c	core	large	59.52	n.a.	25.68	0.36	n.a.	n.a.	6.84	7.66	0.61	n.a.	100.67	64.66	3.39	31.94
S-type BA	34B_UN86_123r	rim		57.64	n.a.	26.64	0.60	n.a.	n.a.	7.73	7.14	0.38	n.a.	100.14	61.20	2.15	36.65
S-type BA	34B_UN87_0c	core	small	55.82	n.a.	27.01	0.66	n.a.	n.a.	9.02	6.32	0.42	n.a.	99.25	54.58	2.39	43.03
S-type BA	34B_UN87_39r	rim		59.46	n.a.	25.46	0.62	n.a.	n.a.	6.97	7.17	0.32	n.a.	100.00	63.84	1.88	34.29

Deposit type	Sample	Location	Description	SiO_2	TiO_2	Al_2O_3	FeOt	MnO	MgO	CaO	Na_2O	K_2O	Cr_2O_3	Total	Ab	Or	An
S-type BA	34B_UN88_0c	core	small	47.25	n.a.	33.40	0.88	n.a.	n.a.	16.02	2.35	0.27	n.a.	100.17	20.64	1.57	77.78
S-type BA	34B_UN88_83r	rim		54.06	n.a.	26.40	2.09	n.a.	n.a.	10.97	5.23	0.44	n.a.	99.18	45.16	2.49	52.35
S-type BA	34B_UN89_119r	rim	long slender	46.63	n.a.	34.51	0.02	n.a.	n.a.	17.35	1.58	0.17	n.a.	100.26	13.98	1.00	85.02
F-type RD	183_plag1	rim	euhedral, subtle zoning in BSE, large (~200 µm long), tabular	56.96	0.04	26.85	0.42	b.d.	0.05	8.55	6.56	0.19	b.d.	99.63	57.50	1.11	41.39
F-type RD	183_plag2	int		57.53	b.d.	26.76	0.42	b.d.	0.06	8.30	6.74	0.21	b.d.	100.02	58.81	1.20	39.99
F-type RD	183_plag3	int		58.29	0.03	26.10	0.31	b.d.	0.05	7.56	7.14	0.26	b.d.	99.74	62.13	1.52	36.35
F-type RD	183_plag4	core		57.75	0.03	26.39	0.37	b.d.	0.05	7.98	6.89	0.24	b.d.	99.70	60.14	1.38	38.48
F-type RD	183_plag5	rim	subhedral (fragmented), elongate, large (~500 µm long)	57.46	0.04	26.59	0.44	b.d.	0.05	8.34	6.75	0.24	b.d.	99.92	58.60	1.38	40.03
F-type RD	183_plag6	core		57.28	0.04	26.52	0.40	b.d.	0.05	8.16	6.91	0.26	b.d.	99.62	59.64	1.47	38.89
F-type RD	183_plag8	int	euhderal, tabular, ~150 µm long	58.84	0.06	25.78	0.33	b.d.	0.04	7.30	7.33	0.27	b.d.	99.95	63.54	1.54	34.92
F-type RD	183_plag9	core		58.69	0.07	25.70	0.38	b.d.	0.06	7.34	7.37	0.29	b.d.	99.90	63.46	1.65	34.89
F-type RD	183_plag10	rim	subhedral, elongate, huge ~1 mm long	57.62	0.03	26.78	0.44	b.d.	0.06	8.33	6.56	0.24	b.d.	100.06	57.92	1.39	40.69
F-type RD	183_plag11	core		58.47	b.d.	25.78	0.37	b.d.	0.05	7.38	7.18	0.26	b.d.	99.49	62.84	1.48	35.69
F-type RD	183_plag12	rim	subhedral, ~500 µm long	56.73	0.04	27.21	0.39	b.d.	0.05	8.66	6.51	0.21	b.d.	99.80	56.92	1.23	41.85
F-type RD	183_plag13	core		58.35	0.04	26.10	0.36	b.d.	0.05	7.58	7.07	0.25	b.d.	99.80	61.91	1.41	36.68
F-type RD	183_plag14	rim	subhedral, ~500 µm long	57.06	0.08	26.71	0.38	b.d.	0.04	8.27	6.74	0.23	b.d.	99.50	58.78	1.31	39.91
F-type RD	183_plag15	core		57.69	0.05	26.27	0.40	b.d.	0.05	7.77	6.94	0.25	b.d.	99.41	60.91	1.42	37.67
F-type RD	183_plag16	rim	euhedral, ~200 µm long, tabular	56.84	0.07	26.88	0.45	0.04	0.05	8.41	6.72	0.22	b.d.	99.69	58.37	1.27	40.35
F-type RD	183_plag17	core		56.58	0.06	27.09	0.38	b.d.	0.05	8.75	6.55	0.22	b.d.	99.69	56.84	1.24	41.93
F-type RD	06c_UN4c	core	large xtl	59.78	n.a.	26.38	0.25	n.a.	n.a.	6.68	7.52	0.54	n.a.	101.16	65.02	3.06	31.92
F-type RD	06c_UN4m	int		60.93	n.a.	25.68	0.46	n.a.	n.a.	6.24	7.91	0.22	n.a.	101.44	68.78	1.24	29.98
F-type RD	06c_UN4r	rim		60.18	n.a.	26.45	0.37	n.a.	n.a.	6.58	7.79	0.48	n.a.	101.85	66.36	2.67	30.98
F-type RD	06c_UN6c	core	huge xtl	60.85	n.a.	25.81	0.24	n.a.	n.a.	6.22	7.72	0.41	n.a.	101.25	67.55	2.39	30.06
F-type RD	06c_UN6r	rim		59.54	n.a.	26.79	0.28	n.a.	n.a.	7.09	7.14	0.29	n.a.	101.14	63.48	1.69	34.83
F-type RD	06c_UN7c	core	huge xtl, other half of xtl UN6	59.93	n.a.	25.87	0.21	n.a.	n.a.	6.40	7.62	0.47	n.a.	100.50	66.46	2.67	30.87
F-type RD	06c_UN7r	rim		59.11	n.a.	26.22	0.45	n.a.	n.a.	7.09	7.41	0.29	n.a.	100.58	64.33	1.65	34.02
F-type RD	06c_UN8c	core	small	59.45	n.a.	25.77	0.34	n.a.	n.a.	6.83	7.40	0.43	n.a.	100.22	64.58	2.49	32.93
F-type RD	06c_UN8r	rim		60.07	n.a.	25.72	0.30	n.a.	n.a.	6.97	7.31	0.21	n.a.	100.57	64.70	1.20	34.09
F-type RD	06c_UN9c	core	large	59.02	n.a.	26.50	0.44	n.a.	n.a.	7.89	7.21	0.29	n.a.	101.35	61.30	1.61	37.08
F-type RD	06c_UN9m	int		59.06	n.a.	26.85	0.34	n.a.	n.a.	7.64	7.03	0.10	n.a.	101.02	62.12	0.60	37.28
F-type RD	06c_UN9r	rim		57.79	n.a.	27.69	0.50	n.a.	n.a.	7.96	7.08	0.35	n.a.	101.37	60.48	1.97	37.55
F-type RD	06c_UN10c	core	small	58.86	n.a.	26.27	0.28	n.a.	n.a.	7.17	7.64	0.34	n.a.	100.57	64.60	1.89	33.51
F-type RD	06c_UN10r	rim		58.78	n.a.	26.74	0.28	n.a.	n.a.	7.97	7.24	0.29	n.a.	101.29	61.18	1.61	37.22
F-type RD	06c_UN11c	core	small	58.53	n.a.	26.14	0.41	n.a.	n.a.	7.17	7.42	0.32	n.a.	99.98	64.02	1.82	34.16
F-type RD	06c_UN11r	rim		58.92	n.a.	26.16	0.34	n.a.	n.a.	7.41	7.06	0.54	n.a.	100.41	61.35	3.07	35.58
F-type RD	06c_UN12c	core	small	59.70	n.a.	25.97	0.40	n.a.	n.a.	7.42	7.41	0.41	n.a.	101.31	62.90	2.31	34.80
F-type RD	06c_UN12r	rim		59.00	n.a.	26.57	0.30	n.a.	n.a.	7.59	7.07	0.36	n.a.	100.89	61.45	2.07	36.48

Appendix A4. Major element chemistry of orthopyroxenes. Mg# = $Mg^{2+}/(Mg^{2+} + Fe^{2+})*100$; Wo = $Ca/(Ca+Mg+Fe^{2+})*100$; En = $Mg/(Ca+Mg+Fe^{2+})*100$; Fs = $Fe^{2+}/(Ca+Mg+Fe^{2+})*100$
Abbreviations: S-type = Shishaldin-type, F-type = Fisher-type, RD = rhyodacite, BA = basaltic andesite, inter. = intermediate, ulv = ulvöspinel, opx = orthopyroxene, ap = apatite, plag = plagioclase, BSE = backscattered electron
*A crystal found within the basaltic andesite, but is from a silicic magma.

Deposit type	Sample	Location	Description	SiO_2	TiO_2	Al_2O_3	FeOt	MnO	MgO	CaO	Na_2O	K_2O	Cr_2O_3	NiO	Total	Mg #	Wo	En	Fs
S-type RD	34a_Un62c	core	-	50.33	0.12	0.42	27.42	1.73	16.77	1.65	0.04	n.a.	0.00	0.02	98.50	53.2	3.6	51.2	45.2
S-type RD	34a_UN62r	rim	-	50.97	0.30	0.50	26.95	1.70	17.70	1.72	0.04	n.a.	0.00	0.12	99.99	55.2	3.7	53.2	43.1
S-type RD	34a_UN64c	core	-	51.49	0.00	0.48	26.84	1.70	17.24	2.45	0.09	n.a.	0.00	0.06	100.35	54.6	5.3	51.7	43.0
S-type RD	34a_UN64r	rim	-	53.29	0.24	2.02	23.93	1.30	16.79	1.71	0.55	n.a.	0.00	0.00	99.82	55.6	3.9	53.4	42.7
S-type RD	34a_UN66c	core	-	50.72	0.00	0.44	27.04	2.02	17.74	1.80	0.06	n.a.	0.00	0.00	99.80	56.5	4.0	54.2	41.8
S-type RD	34a_UN66r	rim	-	51.06	0.71	0.62	27.46	1.70	18.00	1.78	0.06	n.a.	0.00	0.05	101.42	55.9	3.8	53.7	42.4
S-type RD	34a_UN68c	core	-	51.43	0.00	0.56	28.13	2.09	16.99	1.96	0.00	n.a.	0.00	0.02	101.18	53.2	4.2	51.0	44.8
S-type RD	34a_UN68r	rim	-	52.67	0.12	3.24	22.67	1.74	14.64	4.65	0.98	n.a.	0.00	0.00	100.72	53.5	10.9	47.7	41.4
S-type RD	34a_UN71c	core	-	51.17	0.47	0.48	28.12	1.85	16.82	1.75	0.05	n.a.	0.01	0.05	100.76	52.3	3.8	50.4	45.9
S-type RD	34a_UN71r	rim	-	51.59	0.00	0.52	27.67	1.86	17.89	1.74	0.07	n.a.	0.04	0.00	101.38	55.7	3.7	53.6	42.6
S-type RD	34a_UN72c	core	-	51.60	0.00	0.54	27.90	1.66	17.63	1.78	0.00	n.a.	0.04	0.02	101.17	54.4	3.8	52.4	43.9
S-type RD	34a_UN72r	rim	-	52.71	0.00	0.95	25.71	1.55	18.61	1.67	0.17	n.a.	0.00	0.05	101.42	56.7	3.5	54.7	41.8
S-type BA	34b_px9r	rim		50.47	0.23	0.52	27.04	1.60	17.06	1.87	0.03	0.01	b.d.	n.a.	98.83	53.9	4.1	51.7	44.2
S-type BA	34b_px10i	inter.	euhedral	50.25	0.19	0.48	27.13	1.67	16.84	1.81	0.04	b.d.	b.d.	n.a.	98.40	53.5	4.0	51.4	44.6
S-type BA	34b_px11c	core		50.41	0.18	0.40	27.89	1.72	16.65	1.75	0.02	b.d.	b.d.	n.a.	99.02	52.6	3.8	50.6	45.6
S-type RD	2I_px1r	rim		52.33	0.32	0.82	21.74	1.25	21.11	1.56	0.02	b.d	b.d	n.a.	99.15	63.4	3.3	61.3	35.4
S-type RD	2I_px2i	inter.	elongate	51.81	0.36	1.29	21.86	1.27	20.87	1.72	0.03	b.d	b.d	n.a.	99.19	63.4	3.6	61.1	35.3
S-type RD	2I_px3c	core		52.07	0.34	0.91	22.29	1.25	21.01	1.51	0.02	b.d	b.d	n.a.	99.42	63.2	3.2	61.2	35.6
S-type RD	2I_px4r	rim		50.96	0.32	1.02	26.31	1.71	17.14	1.88	0.09	0.02	b.d	n.a.	99.44	53.9	4.1	51.7	44.2
S-type RD	2I_px5i	inter.	equant, small	51.05	0.24	0.52	26.77	1.62	17.55	1.76	0.03	b.d	b.d	n.a.	99.54	54.7	3.8	52.6	43.6
S-type RD	2I_px6c	core		50.73	0.23	0.37	26.84	1.73	16.94	1.79	0.02	b.d	b.d	n.a.	98.65	53.2	3.9	51.1	45.0
S-type RD	2I_px9c	core	opx core of cpx xtl	52.64	0.29	0.53	19.16	1.06	23.34	1.61	0.03	b.d	0.06	n.a.	98.73	69.4	3.3	67.1	29.5
S-type RD	2I_px20r	rim	euhedral, small, part	50.69	0.18	0.46	26.41	1.73	17.07	1.61	0.02	b.d	b.d	n.a.	98.17	53.5	3.5	51.7	44.8
S-type RD	2I_px21c	core	of px cluster	50.69	0.37	0.70	26.20	1.66	17.14	1.80	0.03	b.d	b.d	n.a.	98.60	53.8	3.9	51.7	44.4
S-type RD	2I_px22r	rim		50.79	0.35	0.98	25.35	1.55	18.29	1.85	0.07	0.01	b.d	n.a.	99.23	57.5	4.0	55.1	40.8
S-type RD	2I_px23i	inter.	euhedral, tabular, rim has different BSE brightness	51.23	0.21	0.63	25.27	1.58	18.47	1.63	0.02	b.d	b.d	n.a.	99.06	57.1	3.5	55.1	41.4
S-type RD	2I_px23i	inter.		51.10	0.25	0.64	25.77	1.52	18.47	1.60	0.01	b.d	b.d	n.a.	99.35	57.1	3.4	55.1	41.4
S-type RD	2I_px24c	core		51.20	0.35	0.83	24.44	1.46	19.00	1.91	0.03	b.d	b.d	n.a.	99.22	58.9	4.1	56.5	39.4
S-type RD	5E_px3r	rim	elongate & thin, subhedral, in contact with ox (ox3)	51.13	0.34	0.78	25.97	1.67	17.99	1.86	0.03	b.d	b.d	n.a.	99.76	56.0	4.0	53.8	42.2
S-type RD	5E_px4c	core		50.95	0.26	0.65	27.35	1.65	16.79	1.77	0.03	b.d	b.d	n.a.	99.44	52.4	3.8	50.4	45.8
S-type RD	5E_px5r	rim	euhedral, equant,	50.32	0.31	0.91	25.44	1.60	17.85	2.22	0.14	0.05	b.d	n.a.	98.85	57.7	4.9	54.9	40.2
S-type RD	5E_px6c	core	small (10-15 um)	50.64	0.34	1.04	22.59	1.46	19.22	3.04	0.04	b.d	b.d	n.a.	98.38	62.0	6.6	57.9	35.5
S-type RD	5E_px7r	rim	euhedral, elongate,	51.02	0.26	0.63	26.20	1.76	17.62	1.80	0.02	b.d	b.d	n.a.	99.30	55.0	3.9	52.9	43.2
S-type RD	5E_px8c	core	large	50.63	0.21	0.43	27.87	1.82	16.53	1.75	0.02	b.d	b.d	n.a.	99.25	52.1	3.8	50.1	46.1
S-type RD	34A_px3r	rim	small, euhedral,	50.79	0.24	0.42	26.78	1.78	17.00	1.76	0.02	b.d	b.d	n.a.	98.79	53.4	3.8	51.3	44.9
S-type RD	34A_px4c	core	equant	50.62	0.28	0.41	27.57	1.73	16.89	1.77	0.02	b.d	b.d	n.a.	99.27	53.1	3.8	51.1	45.1
S-type RD	34A_px5r	rim	large, subhedral,	50.92	0.27	0.57	25.77	1.62	17.83	1.94	0.02	b.d	0.04	n.a.	98.98	55.8	4.2	53.5	42.3
S-type RD	34A_px6c	core	fragmented?	50.60	0.22	0.57	27.53	1.74	16.40	1.95	0.04	b.d	b.d	n.a.	99.06	52.0	4.2	49.8	46.0
S-type RD	175_px8r	rim	small, subhedral	50.42	0.33	0.83	25.66	1.68	16.73	2.59	0.04	0.01	b.d	n.a.	98.29	53.9	5.7	50.9	43.5
S-type RD	175_px9c	core		50.56	0.31	0.75	25.49	1.68	17.20	2.46	0.03	0.02	b.d	n.a.	98.48	55.0	5.3	52.1	42.6
S-type RD	175_px10r	rim	large, subhedral	50.99	0.21	0.50	27.35	1.73	16.86	1.71	0.03	b.d	b.d	n.a.	99.38	52.6	3.7	50.7	45.6
S-type RD	175_px11c	core		50.42	0.23	0.39	28.86	1.94	15.47	1.77	0.02	b.d	b.d	n.a.	99.12	49.1	3.9	47.2	48.9
S-type RD	177B_px2	rim	small acicular px, rounded w/ cpx core	49.79	0.34	0.98	27.38	1.70	16.44	1.51	0.02	b.d	b.d	n.a.	98.16	52.3	3.3	50.5	46.1
S-type RD	177B_px3r	rim		50.61	0.28	0.60	27.16	1.76	17.15	1.64	0.03	b.d	b.d	n.a.	99.23	53.8	3.6	51.9	44.5
S-type RD	177B_px6c	core	anhedral, resorbed?, w/ cpx rim, attached to ulv	50.90	0.23	0.48	25.83	1.59	17.71	1.72	0.03	b.d	b.d	n.a.	98.48	55.3	3.7	53.2	43.1
S-type RD	177B_px7r	rim	anhedral, resorbed, coexisting with resorbed oxides	51.50	0.23	0.58	24.95	1.54	18.46	1.81	0.02	b.d	b.d	n.a.	99.09	56.9	3.9	54.7	41.4
S-type RD	177B_px8c	core		50.56	0.28	0.74	25.87	1.57	17.99	1.79	0.03	b.d	b.d	n.a.	98.83	56.6	3.9	54.4	41.7

Deposit type	Sample	Location	Description	SiO_2	TiO_2	Al_2O_3	FeOt	MnO	MgO	CaO	Na_2O	K_2O	Cr_2O_3	NiO	Total	Mg #	Wo	En	Fs
S-type RD	177B_px9r	rim	long acicular, so thin though this may not be the	50.33	0.26	0.66	26.63	1.62	17.47	1.73	0.02	b.d	b.d	n.a.	98.73	55.2	3.8	53.1	43.1
S-type RD	177B_px10c	core	"core"	50.31	0.29	0.56	27.46	1.69	16.21	2.08	0.03	b.d	b.d	n.a.	98.64	51.7	4.6	49.3	46.1
S-type RD	177B_px12		small euhedral xtl	51.31	0.31	1.05	22.70	1.30	20.25	1.74	0.04	0.02	b.d	n.a.	98.73	62.4	3.7	60.1	36.2
S-type RD	177B_px13r	rim	zoned, mostly	50.70	0.25	0.48	27.12	1.69	16.93	1.73	0.03	b.d	b.d	n.a.	98.94	53.2	3.8	51.2	45.1
S-type RD	177B_px14i	inter.	euhedral except one	49.89	0.26	0.46	27.66	1.77	16.68	1.71	0.02	b.d	b.d	n.a.	98.45	53.3	3.8	51.3	44.9
S-type BA	34b_px9r*	rim		50.47	0.23	0.52	27.04	1.60	17.06	1.87	0.03	0.01	b.d.	n.a.	98.83	53.9	4.1	51.7	44.2
S-type BA	34b_px10i*	inter.	euhedral	50.25	0.19	0.48	27.13	1.67	16.84	1.81	0.04	b.d.	b.d.	n.a.	98.40	53.5	4.0	51.4	44.6
S-type BA	34b_px11c*	core		50.41	0.18	0.40	27.89	1.72	16.65	1.75	0.02	b.d.	b.d.	n.a.	99.02	52.6	3.8	50.6	45.6
F-type RD	06c_UN183c	core	-	51.18	0.06	0.43	27.02	1.71	17.35	1.77	0.07	n.a.	0.09	0.00	99.68	54.3	3.8	52.2	43.9
F-type RD	06c_UN183r	rim	-	51.63	0.12	0.65	27.17	1.67	17.50	2.17	0.05	n.a.	0.00	0.00	100.96	54.6	4.6	52.1	43.3
F-type RD	06c_UN184c	core	-	53.08	0.30	2.45	25.16	1.52	14.66	1.75	0.81	n.a.	0.00	0.09	99.81	51.0	4.2	48.8	47.0
F-type RD	06c_UN184r	rim	-	51.18	0.47	0.46	27.29	1.99	16.92	1.66	0.05	n.a.	0.03	0.00	100.07	52.7	3.6	50.8	45.6
F-type RD	06c_UN185r	rim	-	50.69	0.24	0.59	27.48	1.89	16.63	1.92	0.01	n.a.	0.01	0.00	99.47	52.5	4.2	50.4	45.5
F-type RD	06c_UN186c	core	-	51.27	0.00	0.39	29.74	2.04	16.05	1.70	0.07	n.a.	0.08	0.00	101.35	50.4	3.7	48.6	47.7
F-type RD	06c_UN187c	core	-	50.79	0.00	0.46	27.78	1.63	16.82	1.92	0.00	n.a.	0.03	0.10	99.53	52.9	4.2	50.7	45.1
F-type RD	06c_UN187r	rim	-	51.49	0.30	0.36	28.41	1.87	17.01	1.77	0.01	n.a.	0.00	0.11	101.33	52.6	3.8	50.6	45.6
F-type RD	06c_UN188c	core	-	51.50	0.24	0.62	27.52	1.73	16.89	1.83	0.00	n.a.	0.08	0.00	100.41	52.2	3.9	50.2	45.9
F-type RD	06c_UN188r	rim	-	50.76	0.18	0.58	27.30	1.94	16.60	1.68	0.07	n.a.	0.02	0.03	99.16	52.5	3.7	50.5	45.8
F-type RD	183_px1r	rim	small, euhedral	51.19	0.30	0.53	24.97	1.34	18.46	1.84	0.02	b.d	b.d	n.a.	98.66	57.0	3.9	54.8	41.3
F-type RD	183_px2c	core		51.02	0.32	0.63	25.15	1.31	18.29	1.82	0.03	0.01	b.d	n.a.	98.57	56.7	3.9	54.5	41.6
F-type RD	183_px3r	rim	equant, euhedral	50.63	0.29	0.64	25.30	1.37	18.68	1.82	0.03	0.02	b.d	n.a.	98.77	58.5	3.9	56.2	39.8
F-type RD	183_px4c	core		50.30	0.24	0.60	26.95	1.50	17.30	1.86	0.02	b.d	b.d	n.a.	98.78	54.7	4.0	52.5	43.4
F-type RD	183_px5r	rim	large, seems	51.07	0.27	0.62	25.53	1.43	18.30	1.77	0.05	0.02	b.d	n.a.	99.05	56.9	3.8	54.8	41.4
F-type RD	183_px6c	core	euhedral but it is	50.53	0.27	0.63	27.09	1.49	17.02	1.90	0.02	b.d	b.d	n.a.	98.96	53.6	4.1	51.4	44.5
F-type RD	193_px1r	rim	large, subhedral	50.88	0.33	0.63	25.04	1.33	18.50	1.78	0.02	b.d	b.d	n.a.	98.49	57.4	3.8	55.2	41.0
F-type RD	193_px2c	core		50.47	0.31	0.66	27.00	1.41	16.50	2.35	0.03	b.d	b.d	n.a.	98.72	52.5	5.1	49.8	45.1
F-type RD	193_px3r	rim	small, subhedral but	51.31	0.32	0.91	24.66	1.30	17.68	1.83	0.07	0.07	b.d	n.a.	98.15	56.1	4.0	53.9	42.1
F-type RD	193_px4i	inter.	well-shaped, with	51.05	0.37	0.54	26.59	1.47	17.36	1.92	0.02	b.d	b.d	n.a.	99.31	54.0	4.1	51.8	44.1
F-type RD	193_px5c	core	coexisting ox	51.05	0.28	0.53	25.35	1.38	17.93	1.80	0.01	b.d	b.d	n.a.	98.33	55.8	3.9	53.6	42.5
F-type RD	193_px6r	rim	large subhedral with	51.54	0.31	0.61	25.59	1.37	17.57	1.77	0.03	0.02	b.d	n.a.	98.81	55.0	3.8	52.9	43.2
F-type RD	193_px7c	core	ulv attached & ap	51.04	0.24	0.45	26.05	1.41	17.86	1.83	0.02	b.d	b.d	n.a.	98.89	55.5	3.9	53.3	42.8
F-type RD	193_px8r	rim	large, euhedral,	51.15	0.27	0.65	25.09	1.34	18.45	1.77	0.06	0.01	b.d	n.a.	98.79	57.2	3.8	55.1	41.1
F-type RD	193_px9c	core	elongate with good	50.71	0.31	0.61	26.64	1.46	17.20	1.80	0.02	b.d	b.d	n.a.	98.76	53.8	3.9	51.7	44.4

Appendix A5. Major element chemistry of clinopyroxenes. Mg# = $Mg^{2+}/(Mg^{2+} + Fe^{2+})*100$; Wo = $Ca/(Ca+Mg+Fe^{2+})*100$; En = $Mg/(Ca+Mg+Fe^{2+})*100$; Fs = $Fe^{2+}/(Ca+Mg+Fe^{2+})*100$
Abbreviations: S-type = Shishaldin-type, F-type = Fisher-type, RD = rhyodacite, BA = basaltic andesite, inter. = intermediate, ulv = ulvöspinel, opx = orthopyroxene, ap = apatite, plag = plagioclase, BSE = backscattered electron
*A crystal found within the basaltic andesite, but is from a silicic magma.

Deposit type	Sample	Location	Description	SiO_2	TiO_2	Al_2O_3	FeOt	MnO	MgO	CaO	Na_2O	K_2O	Cr_2O_3	NiO	Total	Mg #	Wo	En	Fs
S-type RD	34a_UN69c	core	-	50.89	0.12	0.81	16.79	1.10	11.74	17.75	0.27	n.a.	0.04	b.d.	99.52	58.3	38.8	35.7	25.5
S-type RD	34a_UN69r	rim		51.46	0.74	1.15	15.13	1.12	12.77	18.31	0.27	n.a.	b.d.	b.d.	100.96	62.7	39.2	38.1	22.7
S-type RD	2I_px7r	rim	with opx core, partially resorbed?	50.41	0.56	1.63	17.38	1.32	12.94	14.80	0.29	0.02	b.d	n.a.	99.34	59.0	32.7	39.7	27.6
S-type RD	2I_px8i	inter.		45.88	2.18	6.43	12.80	0.71	11.79	18.42	0.45	0.01	b.d	n.a.	98.68	69.2	43.7	39.0	17.3
S-type RD	2I_px13r	rim	elongate subhedral w/ melt & ap inclusions	52.54	0.28	1.64	15.86	1.13	11.48	17.03	0.37	0.09	b.d	n.a.	100.42	56.3	37.5	35.2	27.3
S-type RD	2I_px14i	inter.		50.60	0.33	0.90	16.53	1.24	11.67	17.20	0.28	b.d	b.d	n.a.	98.74	57.4	37.8	35.7	26.5
S-type RD	2I_px15c	core		50.66	0.31	0.78	20.07	1.38	12.34	14.30	0.23	b.d	b.d	n.a.	100.06	54.9	31.4	37.7	31.0
S-type RD	2I_px16r	rim	part of cluster of ox & plag, fragmented	51.01	0.31	0.97	14.62	1.06	12.08	18.31	0.29	0.01	b.d	n.a.	98.67	60.9	39.9	36.6	23.5
S-type RD	2I_px17c	core		50.76	0.37	1.02	14.62	0.96	12.21	18.40	0.30	b.d	b.d	n.a.	98.65	62.1	40.2	37.1	22.7
S-type RD	2I_px18r	rim	subhedral, well-formed xtl	49.69	0.72	2.49	14.75	0.93	11.65	18.21	0.37	0.02	b.d	n.a.	98.83	61.1	40.7	36.2	23.1
S-type RD	2I_px19c	core		51.11	0.37	1.04	14.41	1.00	12.20	18.53	0.29	b.d	b.d	n.a.	98.95	61.5	40.2	36.8	23.0
S-type RD	5E_px1r	rim	subhedral, part of cluster of ox & plag & px	52.88	0.50	3.69	12.71	0.85	10.62	16.34	0.91	0.33	b.d	n.a.	98.83	59.8	39.8	36.0	24.2
S-type RD	5E_px2c	core		50.90	0.32	1.10	15.38	1.17	12.36	17.50	0.30	b.d	b.d	n.a.	99.04	61.0	38.3	37.6	24.1
S-type RD	175_px1r	rim	elongate, subhedral, with melt & ap inclusions	49.69	0.69	1.80	15.02	1.10	11.99	17.27	0.29	0.02	b.d	n.a.	97.86	60.4	38.4	37.2	24.4
S-type RD	175_px2i	inter.		51.33	0.34	0.94	15.28	1.15	11.99	18.26	0.30	b.d	b.d	n.a.	99.59	59.8	39.6	36.1	24.3
S-type RD	175_px3c	core		50.97	0.36	1.03	14.72	1.09	11.95	18.70	0.31	b.d	b.d	n.a.	99.13	61.2	40.8	36.3	23.0
S-type RD	175_px6r	rim	elongate, subhedral, with melt channel in interior?	47.23	1.75	5.23	12.71	0.65	12.27	18.39	0.44	0.02	b.d	n.a.	98.69	68.9	42.6	39.6	17.8
S-type RD	175_px7c	core		50.85	0.48	1.14	14.86	1.13	12.73	17.36	0.28	0.03	b.d	n.a.	98.86	62.2	37.9	38.7	23.5
S-type RD	177B_px4c	core	rounded w/ opx rim	49.25	1.36	3.52	13.48	0.63	14.68	15.46	0.33	0.03	b.d	n.a.	98.74	68.8	34.2	45.2	20.5
S-type RD	177B_px5r	rim	anhedral, resorbed, w/ opx core, attached to ulv	49.64	1.07	2.77	12.45	0.70	14.15	17.05	0.38	0.03	b.d	n.a.	98.24	70.2	37.8	43.6	18.5
S-type BA	34b_px1r	rim	small, subhedral	50.53	0.43	1.21	15.50	1.05	12.17	17.88	0.28	0.02	b.d.	n.a.	99.07	61.1	39.2	37.2	23.6
S-type BA	34b_px2c	core		50.81	0.40	0.85	15.25	1.03	11.57	18.62	0.29	b.d.	b.d.	n.a.	98.82	59.1	40.6	35.1	24.3
S-type BA	34b_px3r	rim	euhedral, attached to px5-8	51.19	0.66	2.34	9.71	0.29	15.39	19.41	0.21	b.d.	b.d.	n.a.	99.19	76.9	41.1	45.3	13.6
S-type BA	34b_px4c	core		51.83	0.73	2.10	8.39	0.27	15.65	20.24	0.25	b.d.	b.d.	n.a.	99.46	79.1	42.4	45.6	12.1
S-type BA	34b_px5r	rim	sector-zoned, BSE-dark zone	50.04	0.83	3.03	10.50	0.29	15.19	18.47	0.21	b.d.	b.d.	n.a.	98.56	75.9	39.9	45.6	14.5
S-type BA	34b_px6c	core		51.41	0.63	2.09	8.47	0.24	15.63	20.36	0.25	0.02	b.d.	n.a.	99.09	80.7	43.0	46.0	11.0
S-type BA	34b_px7r	rim	sector-zoned, BSE-lighter zone	46.49	1.64	6.38	10.83	0.28	12.83	19.58	0.32	0.02	b.d.	n.a.	98.37	75.9	45.4	41.4	13.2
S-type BA	34b_px8c	core		48.57	1.32	4.62	9.56	0.24	14.00	20.39	0.35	b.d.	b.d.	n.a.	99.05	79.8	45.5	43.5	11.0
S-type BA	2C_px1-rim*	rim	large, splintery, subhedral, fragmented, w/ long apatite inclusion	50.78	0.45	1.53	13.76	0.93	12.31	18.53	0.32	b.d	b.d	n.a.	98.62	62.8	40.4	37.4	22.1
S-type BA	2C_px2-core*	core		50.91	0.32	0.96	14.84	1.03	11.88	18.57	0.29	b.d	b.d	n.a.	98.81	60.5	40.5	36.0	23.5
S-type BA	2C_px3-rim*	rim		50.41	0.40	1.00	14.49	1.05	12.63	18.35	0.29	b.d	b.d	n.a.	98.62	64.9	40.4	38.7	20.9
S-type BA	2C_px1 (34B)r	rim	resorbed cluster of px & ox	50.38	0.54	1.82	14.73	1.26	12.58	16.80	0.38	0.03	b.d	n.a.	98.54	62.2	37.4	38.9	23.7
S-type BA	2C_px2 (34B)c	core		48.95	1.26	3.40	15.18	0.97	12.85	15.71	0.40	b.d	b.d	n.a.	98.70	62.4	35.4	40.3	24.3
S-type BA	2C_px3(34B)r	rim	equant & euhedral	46.01	2.15	7.27	11.35	0.27	12.07	19.71	0.41	0.02	b.d	n.a.	99.26	73.1	46.2	39.3	14.5
S-type BA	2C_px4(34B)c	core		49.11	1.45	4.00	9.88	0.41	14.09	19.71	0.34	b.d	b.d	n.a.	98.99	76.6	43.5	43.3	13.2
F-type RD	06c_UN189c	core	-	50.94	0.98	0.78	18.69	1.50	12.36	15.19	0.23	n.a.	b.d.	b.d.	100.66	55.4	32.9	37.2	29.9
F-type RD	06c_UN189r	rim		51.53	0.87	0.77	16.64	1.29	11.81	17.55	0.24	n.a.	b.d.	b.d.	100.69	56.1	37.5	35.1	27.4
F-type RD	06c_UN190		-	51.43	0.31	0.92	14.66	1.21	12.41	18.29	0.26	n.a.	0.05	0.04	99.58	61.6	39.5	37.3	23.3

Appendix A6. Major element chemistry of ulvöspinel.
Ulvöspinel (ulv) fraction calculated using Stormer (1983).
Abbreviations: S-type = Shishaldin-type, F-type = Fisher-type, RD = rhyodacite, BA = basaltic andesite, inter. = intermediate, b.d. = below detection, w/ = with, ap = apatite, opx = orthopyroxene, cpx = clinopyroxene

Deposit Type	Sample	Location	Description	SiO_2	TiO_2	Al_2O_3	FeOt	MnO	MgO	CaO	Na_2O	K_2O	Cr_2O_3	V_2O_3	NiO	Total	Ulv fraction
S-type RD	2I_ox1	rim	Attached to ox3-4 w/ ap	0.06	17.24	1.80	72.46	1.12	1.81	0.02	b.d.	0.02	b.d.	b.d.	b.d.	94.53	0.51
S-type RD	2I_ox2	core	inclusion between them	b.d.	19.23	1.84	72.65	1.09	1.66	0.00	b.d.	b.d.	b.d.	0.04	b.d.	96.51	0.56
S-type RD	2I_ox3	rim	Attached to ox1-2	0.07	16.71	1.99	73.33	1.05	1.73	0.04	b.d.	0.01	b.d.	0.03	b.d.	94.97	0.49
S-type RD	2I_ox4	core		0.03	18.50	1.93	72.52	1.06	1.73	0.03	b.d.	b.d.	0.03	0.02	b.d.	95.84	0.54
S-type RD	2I_ox5	rim	subhedral, part of plag-cpx clot	0.07	19.56	1.85	69.43	0.94	1.70	0.03	b.d.	b.d.	b.d.	b.d.	b.d.	93.58	0.59
S-type RD	2I_ox6	core		0.03	19.48	1.86	71.45	1.11	1.69	0.01	b.d.	b.d.	b.d.	0.05	b.d.	95.69	0.58
S-type RD	5E_ox1	rim	subhedral, attached to cpx	0.06	18.22	1.93	71.18	1.06	1.70	0.06	b.d.	0.02	b.d.	b.d.	b.d.	94.23	0.55
S-type RD	5E_ox2	core		0.28	18.58	1.94	72.26	1.01	1.64	0.00	b.d.	b.d.	b.d.	b.d.	b.d.	95.72	0.55
S-type RD	5E_ox3	rim	subhedral, attached to px3-4 (opx)	0.09	18.08	1.98	70.85	1.14	1.63	0.02	b.d.	0.01	b.d.	0.06	b.d.	93.87	0.55
S-type RD	5E_ox4	rim	Ilmenite exsolution on opposite end of xtl where it touches vesicle	0.12	18.37	2.00	71.20	1.10	1.32	0.05	b.d.	0.02	b.d.	b.d.	b.d.	94.19	0.56
S-type RD	5E_ox5	rim	subhedral, attached to ox7-8	0.07	17.07	2.02	71.37	1.01	1.72	0.05	b.d.	0.01	b.d.	b.d.	b.d.	93.32	0.52
S-type RD	5E_ox6	core		b.d.	17.92	2.07	72.77	1.03	1.71	0.01	b.d.	b.d.	b.d.	b.d.	b.d.	95.50	0.53
S-type RD	5E_ox7	rim	subhedral, attached to ox5-6	0.03	17.34	2.08	72.48	1.05	1.67	0.02	b.d.	0.01	b.d.	0.06	b.d.	94.74	0.52
S-type RD	5E_ox8	core		b.d.	17.85	2.06	72.48	1.01	1.67	0.03	b.d.	b.d.	b.d.	0.04	b.d.	95.15	0.53
S-type RD	34A_ox2	rim	euhedral except for side attached to small opx, small ~15 µm long	0.09	17.73	1.94	71.39	1.04	1.59	0.10	b.d.	0.01	b.d.	0.04	b.d.	93.93	0.53
S-type RD	175_ox1	rim	subhedral	4.73	16.41	3.34	69.29	1.02	1.53	0.11	0.44	0.15	b.d.	0.05	0.02	97.07	0.63
S-type RD	175_ox2	core		0.03	19.33	2.06	69.60	0.89	1.58	0.03	b.d.	0.02	0.01	0.06	0.03	93.63	0.59
S-type RD	175_ox4	rim	euhedral, small ~10 µm long	0.41	17.15	2.03	71.10	1.09	1.67	0.06	0.04	0.05	b.d.	0.02	0.01	93.64	0.53
S-type RD	175_ox5	rim	anhedral, attached to opx (px10-11)	b.d.	18.16	1.89	72.01	0.99	2.02	0.03	b.d.	0.00	b.d.	0.03	0.01	95.14	0.53
S-type RD	175_ox6	core		b.d.	19.30	1.84	71.62	1.14	1.77	b.d.	b.d.	b.d.	0.02	0.04	b.d.	95.72	0.57
S-type RD	175_ox7	rim	-	0.04	16.80	2.03	72.52	1.07	2.17	0.01	0.01	0.01	0.00	0.03	b.d.	94.69	0.49
S-type RD	175_ox8	core	-	0.04	19.02	1.90	72.02	1.03	1.72	b.d.	0.00	b.d.	0.00	b.d.	b.d.	95.75	0.56
S-type RD	177B_ox3	core	~10 µm long	0.11	17.31	1.93	71.14	1.04	1.69	0.05	b.d.	0.03	b.d.	b.d.	b.d.	93.31	0.52
S-type RD	177B_ox5	rim	euhedral, attached to another ox and a resorbed px with opx core (px6) & cpx rim (px5)	0.22	16.63	2.10	71.09	1.07	1.80	0.11	b.d.	0.03	b.d.	b.d.	b.d.	93.04	0.51
S-type RD	177B_ox7	rim	subhedral, attached to resorbed	0.09	16.96	2.04	71.72	0.99	1.74	0.04	b.d.	0.03	b.d.	b.d.	b.d.	93.61	0.51
S-type RD	177B_ox8	core	px7-8 (opx)	0.09	17.88	1.95	71.59	0.98	1.74	0.06	b.d.	b.d.	b.d.	0.04	b.d.	94.34	0.54
S-type RD	177B_ox9	rim	subhedral, attached to resorbed	0.05	17.92	1.93	71.45	1.02	1.62	0.06	b.d.	0.01	0.03	0.06	b.d.	94.15	0.54
S-type RD	177B_ox10	core	px7-8 (opx)	0.50	17.68	2.06	70.95	1.00	1.74	0.07	b.d.	0.05	b.d.	0.08	b.d.	94.14	0.54
S-type RD	177B_ox11	rim	same as 177B_ox7-10	0.07	17.81	2.00	71.33	0.98	1.62	0.03	b.d.	0.02	b.d.	0.06	b.d.	93.94	0.54
S-type RD	177B_ox12	rim	subhedral, rounded, ~20 µm sides	1.31	16.16	2.27	70.87	1.01	1.84	0.09	0.16	0.05	b.d.	0.04	b.d.	93.81	0.52
S-type RD	177B_ox13	core		0.08	17.43	1.97	71.56	1.01	1.69	0.07	b.d.	b.d.	b.d.	0.07	b.d.	93.88	0.52
S-type BA	5B_ox1	rim	euhedral, attached to olv1-2, ~60 µm sides	0.11	8.45	5.06	73.84	0.26	3.85	0.05	0.01	b.d.	0.16	0.79	b.d.	92.56	0.26
S-type BA	5B_ox2	core		0.03	8.68	5.31	74.75	0.28	4.08	0.02	0.00	b.d.	0.16	0.88	b.d.	94.19	0.27
S-type BA	5B_ox3	rim	euhedral, attached to olv1-2, ~100 µm long	0.03	8.46	5.41	74.94	0.31	3.93	0.01	b.d.	b.d.	0.19	0.81	b.d.	94.09	0.26
S-type BA	5B_ox4	core		0.09	8.80	5.39	74.39	0.31	3.96	b.d.	b.d.	b.d.	0.14	0.89	b.d.	93.97	0.27
F-type RD	183_ox1	rim	subhedral, rounded, ~50 µm sides	0.05	19.57	2.13	70.77	0.91	1.82	0.02	b.d.	0.02	b.d.	0.07	b.d.	95.36	0.59
F-type RD	183_ox2	core		0.05	20.06	2.12	71.34	0.92	1.82	0.02	b.d.	b.d.	b.d.	0.11	b.d.	96.44	0.60
F-type RD	183_ox3	rim	euhedral, attached to another ox,	0.07	18.96	2.11	69.82	0.93	1.84	0.03	0.02	0.01	b.d.	0.05	0.05	93.88	0.58
F-type RD	183_ox4	core	near px1-2, ~100 µm long	0.06	19.40	2.07	71.59	0.97	1.86	0.04	b.d.	0.02	0.03	0.09	b.d.	96.13	0.57
F-type RD	183_ox6	core	subhedral, rounded, ~100 µm long	b.d.	20.27	2.13	70.99	0.95	1.80	b.d.	b.d.	b.d.	b.d.	0.08	b.d.	96.22	0.60
F-type RD	183_ox7	rim	subhedral, attached to ox9-10,	0.54	16.31	2.16	71.93	0.73	2.44	0.04	0.05	0.04	0.04	0.04	b.d.	94.34	0.49
F-type RD	183_ox8	core	~80 µm long	0.05	19.70	2.13	71.17	0.94	2.10	b.d.	b.d.	b.d.	b.d.	0.07	b.d.	96.15	0.58
F-type RD	183_ox9	rim	subhedral, attached to ox7-8, ~80 µm long	0.06	18.15	2.06	70.82	0.91	2.41	0.02	b.d.	b.d.	b.d.	0.08	b.d.	94.50	0.54
F-type RD	183_ox10	core		0.05	19.90	2.13	70.59	0.91	1.94	b.d.	b.d.	b.d.	b.d.	0.06	b.d.	95.57	0.59
F-type RD	183_ox11	rim	subhedral, rounded, ~100 µm	0.05	19.08	2.03	70.06	0.92	1.77	0.03	b.d.	0.02	b.d.	0.07	b.d.	94.04	0.58
F-type RD	183_ox12	core	long, w/ ap inclusions	0.04	19.71	2.06	70.98	0.93	1.76	0.04	b.d.	b.d.	b.d.	0.08	b.d.	95.60	0.59
F-type RD	193_ox1	rim	subhedral, rounded, attached to/included in opx (px3-5), ~60 µm long	b.d.	19.05	2.13	70.20	0.96	1.84	0.06	b.d.	0.01	b.d.	0.08	b.d.	94.32	0.57
F-type RD	193_ox2	core		b.d.	19.39	2.05	70.53	0.94	1.82	0.02	b.d.	b.d.	b.d.	0.10	b.d.	94.85	0.58
F-type RD	193_ox6	core	same xtl as 177B_ox7-8	b.d.	19.85	2.11	70.76	0.93	1.79	0.02	b.d.	0.01	b.d.	0.06	b.d.	95.53	0.59
F-type RD	193_ox7	rim	subhedral, ~80 µm long	0.13	19.01	2.08	70.13	0.92	1.74	0.07	b.d.	b.d.	b.d.	0.04	b.d.	94.14	0.58
F-type RD	193_ox8	core		0.04	19.58	2.15	70.74	0.93	1.81	0.08	b.d.	b.d.	b.d.	0.09	b.d.	95.43	0.59

Appendix A7. Major element chemistry of olivines. Mg# = $Mg^{2+}/(Mg^{2+} + Fe^{2+})*100$ or MgO/(MgO+FeO)*100 in mol%; Fo = Mg/(Mg+Fe+Mn)*100
Abbreviations: S-type = Shishaldin-type, F-type = Fisher-type, RD = rhyodacite, BA = basaltic andesite, inter. = intermediate, ulv = ulvöspinel, opx = orthopyroxene, ap = apatite, plag = plagioclase, BSE = backscattered electron

Deposit type	Sample	Location	Description	SiO_2	TiO_2	Al_2O_3	FeOt	MnO	MgO	CaO	Na_2O	K_2O	Cr_2O_3	Total	Mg #	Fo
S-type BA	34b_olv1	rim	anhedral, ~300 µm long	37.25	b.d	0.02	25.50	0.48	35.75	0.25	0.02	b.d	b.d	99.28	71.4	71.0
S-type BA	34b_olv2	core		37.36	b.d	b.d	26.04	0.46	35.82	0.19	b.d	b.d	b.d	99.86	71.0	70.7
S-type BA	34b_olv3	rim	anhedral, ~100 µm long,	37.49	0.05	b.d	25.67	0.49	35.72	0.22	0.02	b.d	b.d	99.67	71.3	70.9
S-type BA	34b_olv4	core	next to olv1-2	37.37	b.d	0.02	25.18	0.46	35.74	0.20	b.d	b.d	b.d	98.99	71.7	71.3
S-type BA	34b_olv5	rim	subhedral, ~200 µm long,	37.25	b.d	b.d	25.05	0.46	36.18	0.24	b.d	b.d	b.d	99.17	72.0	71.7
S-type BA	34b_olv6	core	subhedral ulv attached	37.51	b.d	0.03	25.29	0.42	36.28	0.22	b.d	b.d	b.d	99.75	71.9	71.6
S-type BA	5B_olv1	rim	subhedral, ~300 µm long,	36.68	b.d	b.d	24.82	0.44	37.87	0.22	0.03	b.d	b.d	100.06	73.1	72.8
S-type BA	5B_olv2	core	2 ox (ox1-4) attached	37.98	b.d	b.d	25.26	0.39	36.38	0.20	b.d	b.d	b.d	100.20	72.0	71.7
S-type RD	2I_px10	rim	subhedral, zoning (dark BSE core to lighter rim), small Fe-Ti oxides along parts of rim, ~150 µm long	33.47	b.d	b.d	42.72	1.74	19.97	0.23	b.d	b.d	b.d	98.13	45.5	44.5
S-type RD	2I_px11	inter.		36.28	b.d	b.d	28.72	0.95	33.09	0.17	b.d	b.d	b.d	99.20	67.3	66.5
S-type RD	2I_px12	core		37.04	b.d	b.d	27.98	0.79	33.35	0.17	b.d	b.d	b.d	99.33	68.0	67.4